

UNIVERSITY OF CALGARY

Solid-Liquid Mass Transfer and Solid Dynamics in Three-Phase Fluidized Beds

By

Jiasen Song

A THESIS

SUBMITTED TO THE FACULTY OF GRADUATE STUDIES
IN PARTIAL FULFILLMENT OF THE REQUIREMENTS FOR THE
DEGREE OF MASTER OF SCIENCE IN CHEMICAL ENGINEERING

DEPARTMENT OF CHEMICAL AND PETROLEUM ENGINEERING
CALGARY, ALBERTA

APRIL , 2000

© Jiasen Song 2000



National Library
of Canada

Acquisitions and
Bibliographic Services

395 Wellington Street
Ottawa ON K1A 0N4
Canada

Bibliothèque nationale
du Canada

Acquisitions et
services bibliographiques

395, rue Wellington
Ottawa ON K1A 0N4
Canada

Your file Votre référence

Our file Notre référence

The author has granted a non-exclusive licence allowing the National Library of Canada to reproduce, loan, distribute or sell copies of this thesis in microform, paper or electronic formats.

The author retains ownership of the copyright in this thesis. Neither the thesis nor substantial extracts from it may be printed or otherwise reproduced without the author's permission.

L'auteur a accordé une licence non exclusive permettant à la Bibliothèque nationale du Canada de reproduire, prêter, distribuer ou vendre des copies de cette thèse sous la forme de microfiche/film, de reproduction sur papier ou sur format électronique.

L'auteur conserve la propriété du droit d'auteur qui protège cette thèse. Ni la thèse ni des extraits substantiels de celle-ci ne doivent être imprimés ou autrement reproduits sans son autorisation.

0-612-49687-2

Canada

Abstract

Gas-liquid-solid systems have been widely used in physical, chemical, petrochemical and biochemical processes. The successful design of gas-liquid-solid fluidized bed systems depends on the ability to accurately predict the mixing of individual phases and mass transfer between phases. Most previous research has been conducted using small-scale laboratory apparatus with heavy solid particles ($\rho_p \geq 2.0$). The objectives of this work are to study solid-liquid mass transfer and solid dynamics in three-phase fluidized beds with low density particles ($\rho_p < 2.0$). Since one of the more common techniques for measuring solid-liquid mass transfer involves particle tethering, the effect of tethering on solid particle movements as compared to free particles was evaluated.

2-D (x-z) radioactive particle tracking (RPT) results were combined with visual observations to study the solids mixing and flow structure in a three-phase fluidized bed. For 6.35 mm polycarbonate spheres, three flow regions existed in the vortical-spiral flow regime: the descending flow region, the vortical-spiral flow region and the fast bubble flow region. For small and light particles such as polypropylene cylinders (equivalent diameter 4.2 mm), the same three flow regions were also observed. However, ascending flow near the wall at one side of the column and descending flow near the wall at the other side of the column existed periodically.

Solid-liquid mass transfer experiments were performed in two columns (diameters of 12.7 and 30.48 cm) using a tethered benzoic acid particle dissolution technique. With the conditions under study, the solid-liquid mass transfer was found to be independent of liquid velocity but to increase with increasing gas velocity for the 30.48 cm column and for the main-bed region of the 12.7 cm column. The mass transfer coefficient (k_s) decreased with increasing gas superficial velocity in the distributor region of the 12.7 cm column due to gas bypassing. The mass transfer coefficient was found to increase with

column diameter. The scale up factor of $k_s \propto D_c^{0.31}$ was found to be a good approximation for a three-phase fluidized bed containing low density particles.

2-D RPT experiments were also conducted to examine the difference between free and tethered particle movements. RPT results suggested that particle tethering had little effect on x-velocities. In the z-direction, tethered particles exhibited slower movements and this was especially apparent with shorter tether lengths. Statistical analysis of tethered versus free x- and z-velocity distributions suggests that a tether length 3 times the column radius ($3 R_c$) was sufficient to reduce the effects of tethering.

Acknowledgements

I would like to thank my supervisor, Dr. Caroline L. Hyndman, for her guidance and continuous support. Thanks also to Dr. Apostolos Kantzas for his support and advice.

I wish to express my gratitude to the people in TIPM laboratory. Kelly Hamilton was a major contributor in running the particle tracking experiments. Amit Bhargava and Jinwen Chen provided me the FORTRAN program to analyze the image raw data.

I would also like to thank Derek Verhegge for his help in building the column and Noreen Zaman for her help in acquiring pressure fluctuation data. Also thanks to all friends and fellow graduate students who created a very friendly atmosphere in the department.

I acknowledge the financial support of the Natural Science and Engineering Research Council of Canada.

Finally, I express a deep sense of gratitude to my mother, who is illiterate, for her support, encouragement and enduring sacrifices throughout my studies.

**In memory of my father
and to my mother**

TABLE OF CONTENTS

Approval Page	ii
Abstract	iii
Acknowledgements	v
Dedication	vi
Table of Contents	vii
List of Tables	x
List of Figures	xi
Nomenclature	xv
CHAPTER 1 Introduction and Objectives	1
1.1 Introduction	1
1.2 Objectives and Experimental Techniques	2
CHAPTER 2 Literature Review	4
2.1 Flow Regime Identification	4
2.2 Solid-Liquid Mass Transfer	6
2.3 Solid Mixing and Flow Pattern	15
2.3.1 Bubble Motion and Wake Structure	15
2.3.2 Flow Models	18
2.3.3 Solids Mixing and Flow Pattern	22
CHAPTER 3 Theory	28
3.1 Solid-Liquid Mass Transfer	28
3.2 Radioactive Particle Tracking	28
CHAPTER 4 Experimental Methods and Data Treatment	31
4.1 Water System	31

4.2	Air System	31
4.3	The Columns	32
	4.3.1 Smaller Column	32
	4.3.2 Larger Column	34
4.4	Pressure Fluctuation Measurements for Flow Regime Identification	34
4.5	Particle Properties	36
4.6	Mass Transfer Experiments	37
	4.6.1 Preparation of Active Particles	37
	4.6.2 Experimental Procedure	37
4.7	Radioactive Particle Tracking Experiments	38
	4.7.1 The Radioactive Particle	39
	4.7.2 Experimental Procedure	39
	4.7.3 Data Treatment	40
CHAPTER 5 Results and Discussion		41
5.1	Flow Regime Identification	41
5.2	Liquid-Solid Mass Transfer	47
	5.2.1 Effect of Liquid Velocity on Sherwood Number	48
	5.2.1.1 Smaller Column	48
	5.2.1.2 Larger Column	49
	5.2.2 Effect of Gas Velocity on Sherwood Number	50
	5.2.2.1 Smaller Column	50
	5.2.2.2 Larger Column	51
	5.2.3 Scale up Effects	53
5.3	Solid Dynamics	56
	5.3.1 Particle Tracking of Polycarbonate Beads over the Entire Column (Set 1)	57
	5.3.1.1 Free Particle Movements	58

5.3.1.2 Particle Tethering	61
5.3.2 Particle Tracking of Polycarbonate Beads (Set 2)	65
5.3.2.1 Flow Pattern for the Vortical-Spiral Flow Regime	65
5.3.2.2 Free Versus Tethered Particle Movements	70
5.3.3 Particle Tracking of	
Polypropylene Cylindrical Beads (Set 3)	77
5.3.3.1 Flow Patterns	77
5.3.3.2 Free Versus Tethered Particle Movements	83
 CHAPTER 6 Conclusions and Recommendations	 90
6.1 Conclusions	90
6.2 Recommendations	91
 References	 92
 Appendix A Rotameter Calibration	 99
Appendix B Gas-Liquid Distributor	100
Appendix C Minimum L-S Fluidized Velocity	101
Appendix D Mass Transfer Coefficient Experimental Data	102
Appendix E RPT Image Data	107
Appendix F Goodness of Fit Analysis	114
Appendix G Calculation of Average Particle	
Ascending and Descending Velocities	116

List of Tables

Table 2.1	Discrepancies of solid-liquid mass transfer in the literature	8
Table 2.2	Correlations for solid-liquid mass transfer in three-phase fluidized beds	9
Table 4.1	Physical properties of solid particles	36
Table 5.1	Mass transfer experimental operating parameters	48
Table 5.2	Radioactive particle tracking experimental operating parameters	57
Table 5.3	Goodness of fit for tethered to free velocity frequency distributions (PC, $U_g = 1.46$ cm/s)	63
Table 5.4	Goodness of fit for tethered to free velocity frequency distributions (PC, $U_g = 2.16$ cm/s, $U_L = 2.69$ cm/s)	77
Table 5.5	Goodness of fit for tethered to free velocity frequency distributions (PP, $U_L = 2.20$ cm/s)	88
Table D.1	Mass transfer data from the 12.7 cm ID column	103
Table D.2	Mass transfer data from the 30.48 cm ID column	105
Table E.1	Sample of RPT image data after treating (PP, tethered = 9 cm, run 11)	107
Table F.1	Sample calculation of the goodness of fit analysis ($U_g = 1.46$ cm/s, $U_L = 2.08$ cm/s, polycarbonate beads)	114

List of Figures

Figure 2.1	Schematic of a bubble wake structure (from Kitano and Fan, 1988)	17
Figure 2.2	The generalized wake model for the cocurrent up-flow three-phase fluidized bed (from Bhatia and Epstein, 1974)	19
Figure 2.3	Scheme of the modified three-phase counter-current wake model (from Cassanello <i>et al.</i> , 1996)	21
Figure 2.4	Flow structure in the vortical-spiral flow regime in a gas-liquid-solid fluidization system (from Chen <i>et al.</i> , 1994)	24
Figure 3.1	Schematic representation of the gamma camera imaging system	30
Figure 4.1	Experimental apparatus for mass transfer (length in cm)	33
Figure 4.2	30.48 cm diameter column diagram	35
Figure 4.3	Experimental apparatus for RPT	39
Figure 5.1	Pressure fluctuation signals for the dispersed flow regime ($U_L = 2$ cm/s, $U_g = 1$ cm/s, $D_c = 12.7$ cm)	43
Figure 5.2	Pressure fluctuation signals for the vortical-spiral flow regime ($U_L = 2$ cm/s, $U_g = 2$ cm/s, $D_c = 12.7$ cm)	43
Figure 5.3	Pressure fluctuation signals for the turbulent flow regime ($U_L = 2$ cm/s, $U_g = 3$ cm/s, $D_c = 12.7$ cm)	44
Figure 5.4	Power spectral density function for the dispersed flow regime ($U_L = 2$ cm/s, $U_g = 1$ cm/s, $D_c = 12.7$ cm)	44
Figure 5.5	Power spectral density function for the vortical-spiral flow regime ($U_L = 2$ cm/s, $U_g = 2$ cm/s, $D_c = 12.7$ cm)	45
Figure 5.6	Power spectral density function for the turbulent flow regime ($U_L = 2$ cm/s, $U_g = 3$ cm/s, $D_c = 12.7$ cm)	45
Figure 5.7	Power spectral density function for the dispersed flow regime ($U_L = 2$ cm/s, $U_g = 0.98$ cm/s, $D_c = 30.48$ cm)	46

Figure 5.8	Power spectral density function for the vortical-spiral flow regime ($U_L = 2$ cm/s, $U_g = 1.99$ cm/s, $D_c = 30.48$ cm)	46
Figure 5.9	Power spectral density function for the turbulent flow regime ($U_L = 2$ cm/s, $U_g = 2.98$ cm/s, $D_c = 30.48$ cm)	47
Figure 5.10	Effect of liquid velocity on Sherwood number ($U_g = 1$ cm/s, $D_c = 12.7$ cm)	49
Figure 5.11	Effect of liquid velocity on Sherwood number ($U_g = 1$ cm/s, $D_c = 30.48$ cm)	50
Figure 5.12	Effect of gas velocity on Sherwood number ($U_L = 2$ cm/s, $D_c = 12.7$ cm)	52
Figure 5.13	Effect of gas velocity on Sherwood number ($U_L = 2$ cm/s, $D_c = 30.48$ cm)	52
Figure 5.14	Scale up effect on the Sherwood number ($U_g = 1$ cm/s, distributor)	54
Figure 5.15	Scale up effect on Sherwood number ($U_g = 1$ cm/s, main bed)	54
Figure 5.16	Scale up effect on Sherwood number ($U_L = 2$ cm/s, distributor)	55
Figure 5.17	Scale up effect on Sherwood number ($U_L = 2$ cm/s, main bed)	55
Figure 5.18	Comparison of $k_g/D_c^{0.3}$ obtained with two columns	56
Figure 5.19	Schematic of x- and z- position of tagged particle in RPT experiments ($U_g = 1.46$ cm/s, $U_L = 1.68$ cm/s)	59
Figure 5.20	Schematic of x- and z- position of tagged particle in RPT experiments ($U_g = 1.46$ cm/s, $U_L = 2.08$ cm/s)	60
Figure 5.21	(a) Horizontal position profile ($U_g = 1.46$ cm/s)	62
Figure 5.21	(b) Vertical position profile ($U_g = 1.46$ cm/s)	62
Figure 5.22	X- and Z- velocity distributions ($U_g = 1.46$ cm/s)	64
Figure 5.23	Typical movements of the free-particle (PC, $U_g = 2.16$ cm/s): (a) z-position vs. time (b) ascending and descending path in area A and B respectively	68
Figure 5.24	Comparison of typical movements of free and 9 cm tethered particles (PC, $U_g = 2.16$ cm/s)	71

Figure 5.25	Comparison of typical movements of free and tethered particles (PC, $U_g = 2.16$ cm/s)	72
Figure 5.26	Particle velocity fluctuations (PC, $U_g = 2.16$ cm/s)	73
Figure 5.27	(a) Particle Z-position distribution (PC, $U_g = 2.16$ cm/s)	74
Figure 5.27	(b) Particle X-position distribution (PC, $U_g = 2.16$ cm/s)	75
Figure 5.28	(a) Particle Z-velocity distributions (PC, $U_g = 2.16$ cm/s)	76
Figure 5.28	(b) Particle X-velocity distributions (PC, $U_g = 2.16$ cm/s)	76
Figure 5.29	Typical movements of the free-particle (a) $U_g = 2.0$ cm/s (b) $U_g = 0.82$ cm/s	80
Figure 5.30	Particle ascending and descending paths from area A of Figure 5.29 (a) Ascending (b) Descending	82
Figure 5.31	Comparison of typical movements of free and tethered particles (PP, $U_L = 2.20$ cm/s, $U_g = 2.0$ cm/s)	83
Figure 5.32	(a) Particle Z-position distribution ($U_g = 2.0$ cm/s)	84
Figure 5.32	(b) Particle X-position distribution ($U_g = 2.0$ cm/s)	85
Figure 5.33	(a) Particle Z-position distribution ($U_g = 0.82$ cm/s)	85
Figure 5.33	(b) Particle X-position distribution ($U_g = 0.82$ cm/s)	86
Figure 5.34	X- and Z- velocity distributions (PP, $U_L = 2.20$ cm/s)	87
Figure A.1	Rotameter calibration curve	99
Figure B.1	Gas-liquid distributor for 12.7 cm ID column	100
Figure C.1	Dynamic pressure drop for determining the minimum fluidization velocity in a L-S fluidized bed ($D_c = 12.7$ cm)	101
Figure E.1	Particle occurrence in the column (PC, free particle, $U_g = 2.16$ cm/s)	109
Figure E.2	Particle occurrence in the column (PC, tether = 19 cm, $U_g = 2.16$ cm/s)	109
Figure E.3	Particle occurrence in the column (PC, tether = 9 cm, $U_g = 2.16$ cm/s)	110

Figure E.4	Particle occurrence in the column (PP, free particle, $U_g = 2.0$ cm/s)	110
Figure E.5	Particle occurrence in the column (PP, tether = 19 cm, $U_g = 2.0$ cm/s)	111
Figure E.6	Particle occurrence in the column (PP, tether = 9 cm, $U_g = 2.0$ cm/s)	111
Figure E.7	Particle occurrence in the column (PP, free particle, $U_g = 0.82$ cm/s)	112
Figure E.8	Particle occurrence in the column (PP, tether = 19 cm, $U_g = 0.82$ cm/s)	112
Figure E.9	Particle occurrence in the column (PP, tether = 9 cm, $U_g = 0.82$ cm/s)	113
Figure G.1	Particle velocities in area B of Figure 5.25: (a) Ascending (b) Descending (PC, $U_L = 2.69$ cm/s)	116
Figure G.2	Particle velocities in area A of Figure 5.30: (a) Ascending (b) Descending (PP, $U_L = 2.20$ cm/s)	117

NOMENCLATURE

A	cross-sectional area of the bed, m ²
A _p	active particle surface area, m ²
Ar	Archimedes number ($= d_p^3 g (\rho_s - \rho_L) \rho_L / \mu_L^2$)
Bo	Bond number ($= g d_p^2 \rho_L / \sigma_L$)
C ₀	inlet concentration of ions, mol/m ³
C _A	concentration of electroactive species, mol/m ³
C _b	bulk concentration of benzoic acid in the bed, mol/m ³
C _D	drag coefficient
C _p	particle concentration
C _s	outlet concentration of ions, mol/m ³
C _{sat}	the saturated concentration of benzoic acid in water, mol/m ³
d _p	particle diameter, m
D	diffusivity, m ² /s
D _b	effective bubble diameter, m
D _c	column diameter, m
D _e	axial dispersion coefficient, m ² /s
D _p	particle equivalent diameter, m
e _i	expected frequency
f _i	observed frequency
f _v	bubble wake shedding frequency
F	Faraday number
Fr _g	Froude number ($= U_g^2 / d_p g$)
g	gravitational acceleration, m/s ²
G	gas phase
G ₁	defined by equation 2.1
G ₂	defined by equation 2.2

Ga	Galileo number ($= d_p^3 g \rho_L^2 / \mu_L^2$)
H	fluidized bed height, m
H _p	injection port location, m
I	diffusion limited current, A
I'	intensity of transmitted light
I ₀	intensity of transmitted light in the absence of particles
J _d	Colburn factor ($= (k_s / U_L) / (\mu_L / \rho_L D)^{2/3}$)
k	dimensionless bubble wake size parameter, defined by equation (2.17)
k _s	solid-liquid mass transfer coefficient, m/s
K	constant in equation (2.15)
K _{EW}	effective volumetric mass transfer coefficient between the wake and the emulsion phase
L	column length, m
L(E)	liquid phase in the emulsion
L(W)	liquid phase in the wake region
m	number of terms in the goodness of fit summation
M	weight loss of the active particle, kg
Mv	density number ($= (\rho_s - \rho_L) / \rho_L$)
n _e	number of electrons involved in the electrochemical reaction
Pe	Peclet number ($= uL/D_e$)
R	radial position in the column, m
R _c	inside column radius, m
Re _g	gas Reynolds number ($= U_g \rho_g d_p / \mu_g$)
Re _L	liquid Reynolds number ($= U_L \rho_L d_p / \mu_L$)
S	particle (spherical cathode) surface area, m ²
S(E)	solid phase in the emulsion
S(W)	solid phase in the wake region
Sc	Schmidt number ($= \mu_L / \rho_L D$)

Sh	Sherwood number ($= k_s d_p / D$)
Sr	Strouhal number (defined by equation 2.19)
t	time, s
t_n, t_{n-1}	time at the n^{th} and $(n-1)^{\text{th}}$ data point in the RPT data, s
T	temperature, °C
u	fluid velocity, m/s
U'	turbulence intensity, m/s
U_b	bubble rise velocity, m/s
U_E	emulsion velocity, m/s
U_g	gas superficial velocity, m/s
U_L	liquid superficial velocity, m/s
U_{Lmf}	minimum fluidization liquid velocity for two-phase system, m/s
U_s	particle velocity in a turbulent field, m/s
U_t	particle terminal velocity, m/s
V_s	volume of the solid phase in the bed, m^3
w_s	mass of solid particles in the column, kg
x	ratio of solids holdup in the wake region to the liquid-solid fluidized region, defined by equation (2.16)
x_n, x_{n-1}	x-position at the n^{th} and $(n-1)^{\text{th}}$ data point in the RPT data, m
z	axial distance, m
z_n, z_{n-1}	z-position at the n^{th} and $(n-1)^{\text{th}}$ data point in the RPT data, m

Greek letters

α	level of significance of goodness of fit test
ϵ_g	gas holdup in the bed
$\bar{\epsilon}_g$	cross-sectionally averaged value of gas holdup
ϵ_L	liquid holdup in the bed
ϵ_{lf}	liquid holdup in the liquid-solid fluidized region

ε_{lw}	liquid holdup in the wake region
ε_s	solid holdup in the bed
ε_{sf}	solids holdup in the surrounding liquid-solid fluidized region
ε_{sw}	average solids holdup in the wake region
ε_w	wake volume fraction
μ_g	gas viscosity, kg/(m s)
μ_L	liquid viscosity, kg/(m s)
ρ_c	density ($= \rho_s \varepsilon_s + \rho_L \varepsilon_L$), kg/m ³
ρ_g	gas density, kg/m ³
ρ_L	liquid density, kg/m ³
ρ_p	particle specific gravity
ρ_s	particle density, kg/m ³
σ_L	liquid surface tension, N/m
ϕ	particle sphericity
χ^2	goodness of fit
$\chi^2_{\alpha, m-2}$	critical region for the goodness of fit test

Abbreviations

ACDW	ascending in the central region and descending near the wall
AWDC	ascending near the wall and descending in the central region
CSTR	continuously-stirred tank reactor
HWU	height of a wake-shedding unit defined by equation (2.18)
PC	polycarbonate beads
PP	polypropylene beads
PSDF	power spectral density function
RPT	radioactive particle tracking
RTD	residence-time distribution

TLD

trajectory length distribution

CHAPTER 1

Introduction and Objectives

1.1 Introduction

Gas-liquid-solid systems have been widely used in physical, chemical, petrochemical and biochemical processes successfully. Configuration alternatives include the choice of continuous phase, relative flow directions, and continuous flow or batch. For example, both the liquid and solids can be either in continuous flow or batch while the gas is always in continuous flow; the flow of gas and liquid can be co-current upward, co-current downward, counter-current, or cross-current; the gas may either be a continuous phase or discrete bubbles; the liquid may be a continuous phase, a film, or droplets; and the solids are a discrete phase in either a packed or suspended state (Epstein, 1981; Fan, 1989).

Gas-liquid-solid fluidization is defined as an operation in which a bed of solid particles is suspended in gas and liquid media due to the net drag force of the gas and/or liquid flowing opposite to the net gravitational force or buoyancy force on the particle (Muroyama and Fan, 1985). Three flow regimes can be identified based on the bubble flow behavior in three-phase fluidized beds: the dispersed bubble, the coalesced bubble, and the slugging regime. The dispersed bubble regime predominates at high liquid velocities and at low to intermediate gas velocities. It is characterized by uniform, small sized bubbles. In the coalesced bubble regime, bubbles tend to coalesce and both the bubble size and velocity become large and show a wide distribution. Coalesced bubbles rise near the column center with high velocity and stir the bed violently. The coalesced bubble regime predominates at low liquid and high gas velocities. Most of the industrial columns operate in this regime. If the column diameter is small, the gas bubbles can easily grow to the size of the column diameter at high gas flow rates creating "slug" bubbles which occupy nearly the whole cross section of the column, and the operation is in the slugging regime. The slugging regime is only encountered in small diameter columns.

The major advantages of fluidized systems over fixed bed systems are high macromixing, high reactant conversions for reaction kinetics favoring completely mixed flow patterns, the ability to achieve significant temperature uniformity without the aid of external means, and ease of catalyst replacement. The three-phase fluidized bed reactor was first used commercially in 1968 for hydrotreating petroleum residuals. The process, known as the H-Oil process, was developed in the United States following research and development beginning in the late 1950's (Fan, 1989). Classical applications of three-phase fluidized bed reactors are: H-Oil or LC-Fining processes for hydrogenation and hydrodesulfurization of residual oil, H-Coal process for coal liquefaction; turbulent contacting absorption for flue gas desulfurization; fermentation in the food, chemical and pharmaceutical industries; and aerobic biological wastewater treatment.

Gas-liquid-solid fluidization became a subject for fundamental research only a few decades ago. Considerable progress has been made with respect to an understanding of the phenomena of gas-liquid-solid fluidization since then. The successful design of a gas-liquid-solid fluidized bed system depends on the ability to accurately predict the fundamental properties of the system, specifically the hydrodynamics, the mixing of individual phases and the mass transfer properties. Unfortunately, most of the properties in literature are derived from small-scale laboratory apparatus with heavy solid particles ($\rho_p \geq 2.0$, such as sand, glass beads, steel shot, etc.). Light or low density particles ($\rho_p < 2.0$) have also been widely used in industries such as the aforementioned fermentation and wastewater treatment processes. Therefore, extension of the results to a large diameter column with low-density particles for scale up is essential.

1.2 Objectives and Experimental Techniques

The main objectives of this work are:

- 1) To measure solid-liquid mass transfer coefficients in different regions of a three-phase fluidized bed of light particles.

- 2) To study the scale up effects on mass transfer in a three-phase fluidization system of light particles.
- 3) To verify the applicability of tethered particles as a method of mass transfer study.
- 4) To study the solids mixing and flow structure in a three-phase fluidized bed.

Three experimental techniques are used in the study, namely pressure fluctuation measurements for flow regime identification, radioactive particle tracking for solid mixing and flow structure study, and a dissolution technique for measurement of solid-liquid mass transfer.

CHAPTER 2

Literature Review

2.1 Flow Regime Identification

The performance of a three-phase fluidized bed is substantially influenced by the flow regime. The flow regime of a three-phase fluidized bed is usually determined by visual observation. Although visual observation provides some information on the flow patterns, it is often difficult to positively identify the flow regime transition without quantitative measurements. This is true even in a transparent column, due to the relatively opaque nature of multiphase flow. While for industrial columns that are not transparent, visual identification is impossible.

Fan *et al.* (1986) investigated the pressure fluctuation behavior and flow regime transition in a three-phase fluidized bed. They attempted to characterize the flow regimes in a three-phase fluidized bed by the statistical properties of the wall pressure fluctuations, especially the power spectral density function (PSDF) and the root mean square of the pressure fluctuations. The pressure fluctuation signals appear very similar for dispersed bubble, coalesced bubble, and slug flow regimes. However, when the statistical properties of the signals are calculated, differences in the pressure signals become apparent. For each regime, there is a distinct peak between 0 and 2 Hz and a broad peak between 16 and 25 Hz, although the relative magnitude of these peaks differs for each regime. The PSDF is negligibly small at frequencies above 30 Hz for all three flow regimes. In the dispersed bubble regime, the magnitude of the PSDF between 2 and 16 Hz is small; while it is fairly large in the coalesced bubble regime and is quite large in the slug flow regime. These behaviors suggest a potential objective method for determining the transition from the dispersed bubble regime to the coalesced bubble regime and from the dispersed bubble regime to the slug flow regime.

Jakher (1998) applied the same technique to identify the flow regime and the transition between the regimes. Pressure signals from three locations in the bed were measured and analyzed. PSDF was evaluated and the total power between 2 to 16 Hz was calculated. From the change of the total power versus frequency curve slope, a transition point from the dispersed bubble to the coalesced bubble could be identified. He found that signals from different locations revealed a similar trend for transition from one regime to another, but the transition point was different: the transition occurred last in the region nearest the distributor.

Zhang *et al.* (1997) used a two-element conductivity probe to obtain bubble frequency, sauter mean bubble chord length and the time taken by a bubble to pass a given point. They linked the flow regimes and their transitions directly to the properties of bubbles that characterized these regimes. It was found that in the dispersed bubble regime, bubble frequency increased linearly with gas velocity. The frequency deviated from this linear relationship when the transition to coalesced bubble flow took place. Hence, the dispersed/coalesced bubble flow transition can be obtained from a plot of bubble frequency versus superficial gas velocity, corresponding to the point where the bubble frequency deviates significantly from a linear relationship. As the gas velocity is increased further, bubbles become larger and some bubbles sizes approach the diameter of the column, indicating that the flow pattern has changed to slug flow. The transition between coalesced bubble flow and slug flow is set as the point at which the sauter mean bubble chord length, measured at the center of the column, reaches the column diameter.

Zheng *et al.* (1988) studied the wall pressure fluctuation to identify the flow regimes in a three-phase fluidized bed. They pointed out that different flow regimes could exist in the system simultaneously. The flow regimes significantly affected the holdups of the three-phase fluidized bed reactor and thus its performance. The PSDF was found to be distinctly different for different regimes. The transitions between flow regimes could be obtained by solving the following equations:

$G_1 > 1$	dispersed bubble regime
$G_1 = 1$	dispersed /transition regime transition point
$G_1 < 1$ and $G_2 > 1$	transition regime
$G_2 = 1$	transition/coalesced regime transition point
$G_2 < 1$	coalesced bubble regime

Where:

$$G_1 = 130 Fr_g^{-0.0136} Ar^{-0.395} Bo^{0.621} (1 + U_L / U_g)^{-0.002} (1 - \varepsilon_s)^{0.216} \quad (2.1)$$

$$G_2 = 1.16 Fr_g^{-0.0266} Ar^{-0.0171} Bo^{0.004} (1 + U_L / U_g)^{-0.008} (1 - \varepsilon_s)^{1.45} \quad (2.2)$$

2.2 Solid-Liquid Mass Transfer

In a three-phase fluidized bed reactor, the solid-liquid mass transfer can play an important role in the performance, especially when the process is under mass transfer control. A fundamental understanding of the mechanisms and parameters important to predict the rate of mass transfer is thus vital to achieving the optimum operation and condition necessary for a given goal and system. The mass transfer rate across the solid-liquid interface can be described by the product of three terms: the overall solid-liquid mass transfer coefficient, the solid-liquid interfacial area, and the concentration gradient. The external surface of the solid is generally undeformable and the solid-liquid interfacial area remains constant so long as the external particle surface remains completely wetted. The mass transfer coefficient is thus dependent only on the system hydrodynamics and, consequently is a strong function of the operating variables and physical properties of the individual phases.

Several models describing mass transfer have been suggested in literature and are being employed for the calculation of mass transfer coefficients in a fluidization system. Alvarez-Cuenca *et al.* (1984) utilized the water-oxygen-glass beads system in their studies and reported the existence of two well-differentiated mass transfer zones in a three-phase fluidized bed. The first zone is near the distributor and is termed the "grid

zone". In this zone plug flow conditions prevail. The second zone is termed the "bulk zone", in which axial dispersion is more predominant. Later, Asfour and Nhaesi (1990) developed the two-zone model mentioned above and tested it using experimental data. They claimed that this model was validated for a wide range of operating conditions and proved to perform better than previous models. Asif *et al.* (1992) used residence-time distribution (RTD) experiments to study the hydrodynamics of a liquid-solid fluidized bed and proposed a two-region model. This model used a continuous-stirred tank reactor (CSTR) to account for the distributor region behavior while the rest of the bed was modeled with the conventional dispersion model. They found that in the fluidized beds containing low-density particles, distributor effects on hydrodynamics were significant; while for fluidized bed containing high-density particles, distributor effects were negligible. Kim and Kim (1983), Kato *et al.* (1985), Kim *et al.* (1992) and Gervais *et al.* (1995) studied the axial liquid mixing using a dispersion model in a three-phase fluidization system. Kim and Kim (1983) used a tracer response measurement technique to study the effects of different parameters on the liquid phase axial dispersion coefficient. Their correlation showed that the axial dispersion coefficient increased with increasing gas and liquid velocities and column diameter, but decreased with increasing particle size. They also found that liquid surface tension and viscosity had only little effect on axial dispersion coefficient.

In recent years a number of studies have appeared in the literature regarding solid-liquid mass transfer in three-phase fluidized bed (Hasanien *et al.*, 1984; Arters and Fan, 1986; Prakash *et al.*, 1987; Nikov and Delmas, 1987; Arters and Fan, 1990; Kim *et al.*, 1991). Experimental techniques such as ion-exchange, electrochemical reduction, and dissolution of solids have been used to study solid-liquid mass transfer. However, considerable discrepancies exist between the experimental data in the literature (Table 2.1). This may be due to the different experimental techniques and operating parameters employed by the various researchers. Correlations for solid-liquid mass transfer are shown in Table 2.2.

Table 2.1 Discrepancies of solid-liquid mass transfer in the literature

Authors	Nikov and Delmas (1987)	Prakash <i>et al.</i> (1987)	Arters and Fan (1990)	Kim <i>et al.</i> (1991)	Dutta and Pangarkar (1993)
Experimental Technique	Electrochemical (tethered)	Dissolution (free & tethered)	Dissolution (free & tethered)	Ion-exchange (free)	Dissolution (tethered)
Column dimensions (cm)	$D_c = 5 \text{ \& } 9.4$	$D_c = 17$ $L = 176$	$D_c = 7.6, 10.2, 15.2$ $L = 180, 140, 120$	$D_c = 9.4$ $L = 143$	$D_c = 15 \text{ \& } 30$ $L = 200$
Active particle size (mm) & specific gravity	$d_p = 3.0 \text{ \& } 10$ $\rho_p = 8.15$	Not available	$d_p = 4.2 - 4.5$ $\rho_p = 1.29$	$d_p = 1.0$ $\rho_p = 1.181$	Cylinder: 2×3 $\rho_p = 1.39$
Inert particle size (mm) & specific gravity	$d_p = 3.0 \text{ and } 10$ $\rho_p = 1.34 - 8.15$	$d_p = 5.2$ $\rho_p = 2.52$	$d_p = 2.5 - 3.7$ $\rho_p = 1.15 - 1.47$	$d_p = 1.0$ $\rho_p = 1.181$	$d_p = 0.8$ $\rho_p = 2.59$
Effect of U_L on k_s	Negative	Independent	Independent	Positive	Independent
Effect of U_g on k_s	Positive	Positive (Negative at $U_g = 5 - 15$ cm/s for direct gas jets distributor)	Positive	Positive	Positive
Effect of D_c on k_s	Independent	Not studied	Independent	Not studied	Positive
Effect of tethering on k_s	Not studied	No	Yes	Not studied	Not studied

Table 2.2 Correlations for solid-liquid mass transfer in three-phase fluidized beds

Reference	Experimental Method	U_L (cm/s)	U_g (cm/s)	Correlation	Equation
Hassanien <i>et al.</i> (1984)	Electrochemical	5 - 20	0 - 16	$Sh = 0.264 Fr_g^{0.056} Ga^{0.41} Re_L^{-0.1} Sc^{0.34}$	2.3
Arters (1984)	Dissolution	1.85 - 7.14	0 - 26	$Sh = 0.228(1 + 0.347 Re_g^{0.623}) \phi^{1.35} Ga^{0.323} Mv^{0.3} Sc^{0.4}$ $17.4 < Re_L < 253$ $0.0 < Re_g < 9.80$ $22.3 < Ga < 562$ $1960 < Sc < 3550$	2.4
Arters and Fan (1986)	Dissolution	1.85 - 7.14	0 - 26	$Sh = 0.228(1 + 0.826 Re_g^{0.623}) \phi^{1.35} Ga^{0.323} Mv^{0.3} Sc^{0.4}$	2.5
Nikov and Delmas (1987)	Electrochemical	5 - 25	0 - 43	$Sh = 0.33(GaMvSc)^{1/3} [1 + 0.22 Mv^{-0.57} (U_g / U_L)^{0.77}]$ $0.11 \times 10^6 < Ga < 15.7 \times 10^6$ $860 < Sc < 19,900$ $0.27 < Mv < 7.07$ $0 < U_g / U_L < 3.9$ $0 < U_g^2 / gd_p < 6.28$	2.6

Table 2.2 continued

Reference	Experimental Method	U_L (cm/s)	U_g (cm/s)	Correlation	Equation
Prakash <i>et al.</i> (1987)	Dissolution	3 - 7	0 - 30	$\varepsilon_L J_d = 0.35 \text{Re}_L^{-1/3}$ with $J_d = (k_L / U_L) / (\mu_L / \rho_L D)^{2/3}$	2.7
Kim <i>et al.</i> (1991)	Ion-exchange	0.3 - 1.5	0 - 0.3	$\frac{C_s}{C_0} = \frac{4\Omega \exp(\frac{Pe}{2})}{(1 + \Omega)^2 \exp(\frac{\Omega Pe}{2}) - (1 - \Omega)^2 \exp(-\frac{\Omega Pe}{2})}$ With: $\Omega = 1 + \frac{4}{Pe} \frac{6 * k_L * V_s}{U_L * A * d_p}$	2.8
Jadhav and Pangarkar (1991)	Dissolution (sparged reactor)	none	9 - 35	$Sh = 2 + 0.0915(d_p U' \rho_L / \mu_L)^{0.617} Sc^{0.45}$ ($d_p \leq 1.1$ mm) $Sh = 2 + 0.102(d_p U' \rho_L / \mu_L)^{0.75} Sc^{0.452}$ ($1.54 \leq d_p \leq 3.68$ mm) $U' = 0.43 \{gD_c [U_g - \varepsilon_g U_b - \varepsilon_s U_s (\rho_s - \rho_c) / \rho_L]\}^{1/3}$	2.9 2.10
Dutta and Pangarkar (1993)	Dissolution	1 - 7	1.5 - 20	$Sh = 2 + 0.144(d_p U' \rho_L / \mu_L)^{0.6} Sc^{0.45}$ $U' = 0.43 gD_c \{U_g + U_L - \varepsilon_g U_b - \varepsilon_s U_s (\rho_s - \rho_c) / \rho_c - \rho_L U_L / \rho_c\}^{1/3}$	2.11
Gogoi and Dutta (1996)	Dissolution (sparged reactor)	none	10 - 35	$Sh = 2 + 0.21(d_p U' \rho_L / \mu_L)^{0.1094} Sc^{0.45}$ $U' = 0.49 \{gD_c [U_g - \varepsilon_g U_b - \varepsilon_s U_s (\rho_s - \rho_L) / \rho_L]\}^{1/3}$	2.12

For the ion-exchange method, the bed is packed with fresh resins prior to the start of the operation. An ionic solution is passed through the column and an exchange of ions takes place. The mass transfer coefficient can then be calculated from the known outlet concentration and an appropriate liquid flow model. Kim *et al.* (1991) used Cu^{++} ions in the liquid and H^+ ions from Duolite C20D resin in a three-phase fluidized bed to study the solid-liquid mass transfer. They reported a positive effect of gas and liquid velocities on the solid-liquid mass transfer in a three-phase fluidized bed (see Tables 2.1 and 2.2).

Kikuchi *et al.* (1995) used two systems: (1) K^+ - Na^+ ion-exchange in cation-exchange resin bead beds; (2) zinc dissolution by HCl in zinc-plated glass bead beds to study solid-liquid mass transfer in a three-phase fluidized bed. They found that the solid-liquid mass transfer coefficient for ion-exchange resin beads (light particles) increased with increasing gas velocity. While for glass beads (heavy particles), it remained almost constant for gas velocities below 2 cm/s. At low liquid velocity and for the smaller sized glass beads, the solid-liquid mass transfer coefficient was smaller than those from two-phase fluidized bed. The solid-liquid mass transfer coefficient also decreased with increasing particle diameter.

Nikov and Delmas (1987) used an electrochemical technique to study the mass transfer in two three-phase fluidized beds ($D_c = 5 \text{ cm}$ & 9.4 cm). This method involved a fixed spherical electrode immersed in a fluidized bed of inert particles of the same diameter as the fixed sphere. Mass transfer was measured by an electrochemical method, using the diffusion controlled cathode reduction of ferricyanide ion at the electrode. The mass transfer coefficient k_s is related to the limiting current intensity I by:

$$k_s = \frac{I}{n_e F S C_A} \quad (2.13)$$

They concluded that the solid-liquid mass transfer coefficient was not affected by the column diameter and particle diameter but increased with the gas flow rate; as the density of the particles or liquid flow rate increased, the gas effect decreased.

The most common technique for measuring solid-liquid mass transfer is the dissolution technique. In this technique, a sparingly soluble solid dissolves into the liquid phase. For measurements in the fluidized beds, the bed can be packed either fully or partially with the dissolvable or so-called “active” particles. The particles can be made up entirely of the dissolvable matter or can be coated with dissolvable material. Most studies have used benzoic acid since it is easy to pelletize and has low solubility in water. The mass transfer coefficient can be calculated from the known outlet concentration and an appropriate model for the liquid flow. The dissolution technique may also be used with a tethered particle. In that case, the particle is attached to the end of a thread. The particle is injected into the bed for a certain time and the weight loss of the particle is measured. The main advantage of this method is that it requires no prior knowledge of the hydrodynamic characteristics of the fluidized bed.

Arters (1984) studied solid-liquid mass transfer in a three-phase fluidized bed with a full bed of benzoic acid particles. The benzoic acid concentration was determined at the outlet of the bed and along the length of the bed using in-bed liquid samples. A spectrophotometer was used to analyze the samples at 228 nm. The entire range of his experimental data was described accurately by Equation 2.4 in Table 2.2. His correlation reduces to the modified equation of Ballesteros *et al.* (1982) for two-phase fluidized base case at zero gas Reynolds number ($Re_g = 0$). Arters (1984) concluded the following: solid-liquid mass transfer coefficient was independent of superficial liquid velocity but strongly depended on gas velocity; it also increased with increasing particle size at high gas rates (>6 cm/s) but is independent of particle size at low gas rates (<6 cm/s).

Prakash *et al.* (1987) used free floating and tethered particles to study the solid-liquid mass transfer in a three-phase fluidized bed. Both techniques measured the weight loss of a few particles coated with benzoic acid in a bed of inert glass beads. Mass transfer coefficient k_s was computed using the following equation:

$$-\frac{dM}{dt} = k_s A_p (C_{sat} - C_b) \quad (2.14)$$

A new correlation giving a better fit over the entire range of the mass transfer data of their study was also developed (Equation 2.7 in Table 2.2). The following results were obtained from their experiments: 1) for free floating and tethered particles, the mass transfer coefficients were in close agreement as long the density of coated particles were close enough to the density of inert beads; 2) the mass transfer coefficient increased with gas velocity and reached an asymptotic value at gas velocity above a certain value; 3) the liquid velocity had no significant effect on the solid-liquid mass transfer coefficient within the range of their experiments; 4) mass transfer coefficient decreased with liquid viscosity; 5) surface active agents significantly increased the gas holdup, and thus, increased the mass transfer coefficient. They used a tether length of 176 cm, which is equivalent to $10 R_c$.

Arters and Fan (1990) studied solid-liquid mass transfer experimental methods in a three-phase fluidized bed. Free floating, mobile tethered (fixed with a 5 cm long, thin wire), semimobile tethered (thicker wire), and fixed particles were used. They pointed out that many of the discrepancies in the fluidization literature might be traced directly to experimental procedures and conditions; measurement of mass transfer from single free floating active particles in beds of inerts yielded results comparable to those of entire beds of active particles as long as complete mixing of the particles occurred; particle tethering of any type affected the measurement of the mass transfer; the mass transfer was found to be a function of superficial gas velocity and gas phase holdup and independent of liquid velocity; the mass transfer in the wall region of gas-liquid-solid fluidized beds was significantly less than in more radially centered regions due to the lack of turbulence-inducing bubbles rising along the wall.

Werther (1992) proposed a two phase model to investigate the different factors influencing the scale up of a gas-solid fluidized bed reactor. He pointed out that the scale up of fluidized-bed process involves not only the enlargement of the reactor size, but also a number of characteristic changes of design detail. Two reactors with diameter of 0.2m

(operated at a gas velocity of 0.3m/s) and 3m (operated at a gas velocity of 0.45m/s) respectively were used to study the scale up effect. The gas-solid mass transfer in small reactor was significantly higher than that of the large reactor. Different distributors resulted in different initial bubble sizes, thus affecting the reactant conversion. The particle size distribution also influenced the fluid mechanics. Using the same type of distributor, finer particles led to an equilibrium bubble diameter which was lower than the initial bubble size. While for the larger particles, bubbles grew significantly from their initial bubble size to the equilibrium diameter. The increase of the interfacial area caused by the smaller bubbles resulted in a dramatic improvement of reactor performance. Baffle plates and screens may be used to maintain smaller bubble size and to increase the interfacial mass transfer area.

Jadhav and Pangarkar (1991) studied three-phase sparged reactor and pointed out that mass transfer in a turbulent fluid was a complex process which was governed by the convective transport mode. Their correlations (Equations 2.9 and 2.10 , Table 2.2) thus included a term for turbulence intensity U' . The flow around a particle contributing to convective transport was a combination of: 1) streaming flow due to particle motion relative to the fluid caused by density difference between the particle and surrounding fluid, and 2) flow due to velocity gradient in the surrounding fluid. In a turbulent fluid the particle and fluid velocities were also a random function of time and space. Using two columns (20 cm diameter x 200 cm and 40 cm diameter x 220 cm) in their experiments, they concluded that: 1) k_s increased with the increase of column diameter ($k_s \propto D_c^{0.29}$), 2) k_s decreased with increase in d_p up to 1.1 mm after which it increased with increase d_p up to 1.5mm (further increase in d_p had no effect on k_s), and 3) there was no effect of scale up on the $k_s - d_p$ relationship.

Dutta and Pangarkar (1993) studied the scale up effects on mass transfer in a three phase fluidized bed. The experiments were conducted in acrylic columns of 0.15 and 0.30 m diameters and 2 m height. Air, water, and natural sand were used in this study. A few

benzoic acid particles were tied with very fine nylon thread of around 0.5 m length to a rod. Tether length were therefore $6.67 R_c$ for the 0.15 m diameter column and $3.33 R_c$ for the 0.3 m diameter column. They found that the mass transfer coefficient increased with increasing gas velocity and was independent of liquid velocity over the range of study. The mass transfer coefficient was significantly affected by column diameter and a scale up factor of $k_s \propto D_c^{0.26}$ was proposed. However, one can deduce a scale up factor of $k_s \propto D_c^{0.6}$ from their correlation (Equations 2.11, Table 2.2) instead of $k_s \propto D_c^{0.26}$. The reason could be a mistake in their turbulence intensity equation.

In a later paper, Gogoi and Dutta (1996) used free benzoic acid particles (0.5 wt%) and three cylindrical acrylic columns of diameter 10 cm, 20 cm, and 30 cm and length 250 cm to study the scale up effects on mass transfer in a three-phase sparged reactor. The mass transfer coefficient was found to be dependent on the reactor diameter, and the relationship was $k_s \propto D_c^{0.302}$. Note that according to their correlation (Equations 2.12, Table 2.2), a scale up factor of $k_s \propto D_c^{0.0302}$ is expected. Again, the reason could be a mistake in Equation 2.12; if the exponent on the Reynold's number were close to one (0.906), then the scale up factor reported is obtained.

The literature is divided with respect to the effect on particle tethering (Prakash *et al.*, 1987 vs. Arters and Fan, 1990). A study on tethered versus free particle motion is therefore of interest. Furthermore, relatively few studies on scale-up have been conducted and none yet on light particles in three-phase fluidized beds.

2.3 Solids Mixing and Flow Pattern

2.3.1 Bubble Motion and Wake Structure

In gas-liquid-solid fluidized beds, the flow patterns and solid mixing are very important for determining the heat and mass transfer rates as well as the overall reaction rates.

Solid mixing and flow pattern in a three-phase fluidized bed are closely related to bubble and bubble wake flow characteristics. Consequently, a fundamental understanding of bubble and bubble wake behavior can provide the basis for a mechanistic approach to analysis of the various hydrodynamic phenomena (Fan, 1989).

The interaction between a rising gas bubble and the surrounding liquid or liquid-solid medium results in the observed bubble shape and determines the extent of the disturbance in the surrounding flow field. Bubbles in motion are generally classified by shape as spherical, oblate ellipsoidal, and spherical-cap with the actual shape depending on the dominating forces acting on a bubble. For small bubbles (diameter of volume-equivalent sphere (D_b) less than 1mm in water), the bubble shape is approximately a sphere, the surface tension force dominates, and the bubble rises steadily in a rectilinear path. For intermediate size bubbles, effects of both surface tension and inertia of liquid flowing around the bubble are important and liquid viscosity and the presence of surface-active contaminants influence the bubble dynamics. The motion of intermediate size bubbles is extremely complex; ellipsoidal bubbles exhibit secondary motion characteristics, such as zig-zag or spiral trajectories and shape dilations or oscillations, as they rise. Large bubbles ($D_b > 18$ mm) have an approximately spherical-cap shape and a relatively flat base. The bubbles follow a rectilinear path with some rocking and/or base oscillations. (Fan, 1989)

The differences in the motion of these bubbles inherently depend on the differences in the flow fields immediately behind the bubble, or the so-called bubble wake. The bubble wake has been recognized as a key factor in explaining various phenomena occurring in three-phase fluidized beds such as solids mixing (Larachi *et al.*, 1995, 1996), particle entrainment into the freeboard, and bed contraction upon the initial introduction of gas bubbles into liquid-solid fluidized beds (Rigby and Capes, 1970). Kitano and Fan (1988) used an optical fiber probe system (which was based on a transmission principle) to investigate the wake structure in a two-dimensional liquid-solid fluidized bed. In their

study, an incandescent light passing through the fluidized bed was received by the optical fiber and transmitted to a photomultiplier. The photomultiplier was interfaced with a microcomputer for data analysis and recording. The Lambert-Beer law, which related the particle concentration to the light intensity, was adapted to analyze the data:

$$I' = I_0 e^{-KC_p} \quad (2.15)$$

They subdivided the wake into four regions, namely, a stable liquid wake region (I) immediately beneath the bubble, followed by a stable solids wake region (II), a vortex sheet region (III) and a fluctuating solids wake region (IV) as shown in Figure 2.1. The stable liquid wake region had a very low solids concentration, and its existence was strongly related to the particle terminal velocity. In their study, the primary-wake area was defined as the sum of the stable liquid (I) and stable solids (II) wake regions. They also pointed out that these regions were particularly strongly attached to the rising bubble.

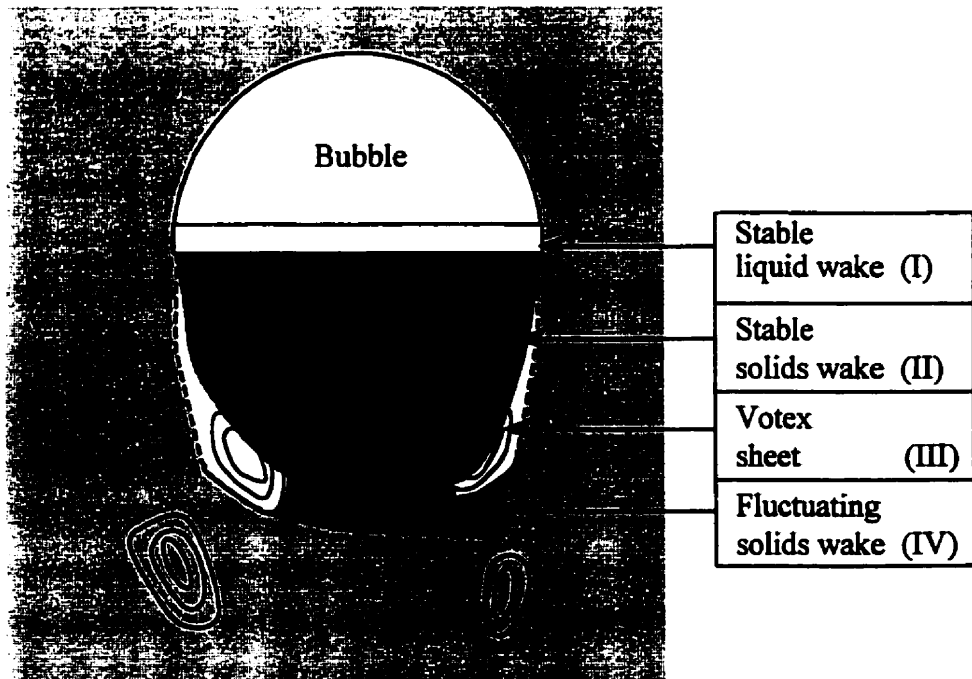


Figure 2.1 Schematic of a bubble wake structure (from Kitano and Fan, 1988)

The variation in solids concentrations between the wake and the surrounding medium and within the wake region itself results from the inability of the particles to follow exactly the flow paths of the liquid elements. The relative value of average solids holdups in the wake region (ϵ_{sw}) to that in the surrounding liquid-solid fluidized region (ϵ_{sf}) is expressed as:

$$x = \epsilon_{sw}/\epsilon_{sf} \quad (2.16)$$

Ostergaard (1965) assumed that the wake porosity was identical to that in the liquid-solid fluidized region, i.e. $x = 1$. Efremov and Vakhrushev (1970), Darton and Harrison (1975) and Baker *et al.* (1977) assumed that the wake was solid-free, i.e. $x = 0$. El-Temtamy and Epstein (1978) assumed x could vary between 0 and 1. Kitano and Fan (1988) found that at small ϵ_{sf} , x could be significantly greater than unity; x was not appreciably influenced by the bubble size but was strongly affected by the solids holdup in the liquid-solid fluidized region.

2.3.2 Flow Models

The development of flow models is essential to the quantitative description of the transport properties in three-phase fluidized beds. The wake concept has provided a fundamental framework for a global treatment of the bed behavior, such as bed contraction, overall phase holdup, axial solids holdup distribution in the freeboard, liquid velocity profiles and particle terminal velocity.

Bhatia and Epstein (1974) proposed the generalized wake model. A dimensionless bubble wake size parameter, k , which was defined as the ratio of the wake volume fraction to the bubble volume fraction in this model, i.e.,

$$k = \epsilon_w/\epsilon_g \quad (2.17)$$

k and x (as previously defined in Equation 2.16) were two key parameters in this model. They divided the bed into a gas bubble region, a wake region, and a liquid-solid

(fluidized) region, as illustrated in Figure 2.2. Several basic assumptions were made in the model development: first, the solids content in the wake could be an arbitrary value different from that in the liquid-solid fluidized region; second, the wake rose at the same velocity as that of the bubble; and third, the Richardson-Zaki correlation between solids holdup and liquid velocity was applied in the liquid-solid fluidized region. As a result, the liquid, solid and gas holdups were obtained in terms of x and k . The two key parameters defined within the model were evaluated empirically or, in some cases, through theoretical development.

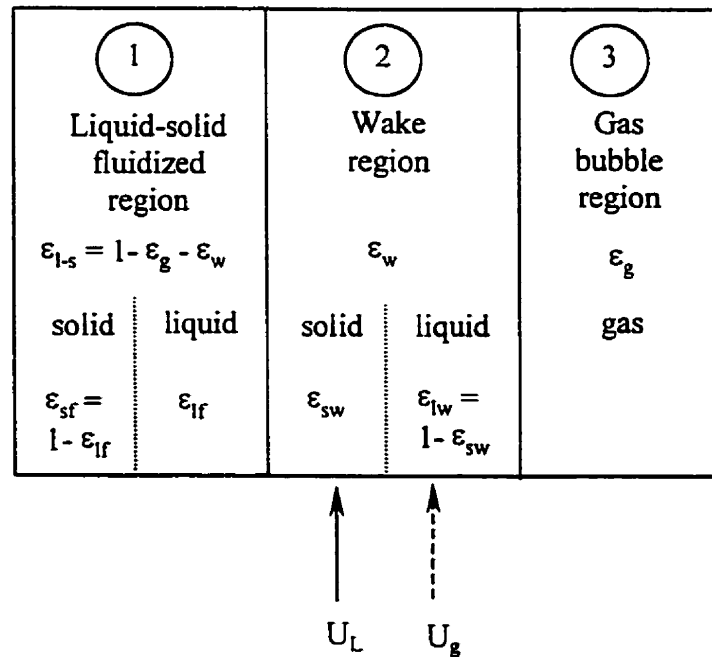


Figure 2.2 The generalized wake model for the cocurrent up-flow three-phase fluidized bed (from Bhatia and Epstein, 1974)

Consideration of the bubble wake structure led to a mechanistic approach to the determination of the axial solids holdup in the freeboard. Page and Harrison (1974) suggested that wake formation and shedding were the main mechanisms for particle entrainment and de-entrainment in the transitional region of the freeboard, and the wake

shedding frequency played a prominent role in the axial variation of solids holdup. El-Temtamy and Epstein (1980) developed a stagewise partition process model for solids entrainment in the freeboard region. They postulated that in each stage the solid particles were carried upward in the bubble wake, transferred to the surrounding liquid-solid region, and settled in the liquid-solid region. The height of a stage (or wake-shedding unit) in the model, defined as the distance traveled by a bubble during the time interval between the shedding of two successive wake fragments, was given by:

$$HWU = \left(\frac{U_g / \varepsilon_g}{U_g / \varepsilon_g - U_L / \varepsilon_L} \right) \left(\frac{D_b}{Sr} \right) \quad (2.18)$$

Where D_b was the effective bubble diameter, and Sr was the Strouhal number defined as:

$$Sr = \left(\frac{D_b f_v}{U_g / \varepsilon_g - U_L / \varepsilon_L} \right) \quad (2.19)$$

They recommended using Sr of 0.27 for air bubbles in water for bubble Reynolds numbers between 2200 and 6000.

Morooka *et al.* (1982) found that the liquid phase flow pattern in a three-phase fluidized bed was similar to that in a bubble column where the liquid flowed upward in the central region and downward in the peripheral region. They proposed a circulating flow model to simulate the lateral distributions of gas holdup and interstitial liquid velocity. The lateral distribution of gas holdup could be approximated by:

$$\varepsilon_g (r/R_c) = 2 \bar{\varepsilon}_g [1 - (r/R_c)^2] \quad (2.20)$$

The liquid velocity was a maximum at the axis and a minimum near the wall. However, it was not necessarily for the liquid velocity to be negative at the wall in a three-phase fluidized bed in contrast to the case of a bubble column operating under liquid-batch conditions.

Other wake models include the structural wake model, the particle terminal velocity model, the drift flux model (Fan, 1989), etc. However, none of the aforementioned models has been used to predict solids mixing behavior in gas-liquid-solid fluidized beds

as a direct result of the wake phenomena. In an attempt to model the longitudinal mixing characteristics of the solids in three-phase fluidized beds, Cassanello *et al.* (1996) developed a one-dimensional, two-zone model which postulated that axial mixing was determined by the action of primary wakes and a wake-emulsion mass transfer. The former was responsible for the upward motion of the solids, and the latter allowed the compensating downward motion to take place in the emulsion phase. This model contained only one fitted parameter K_{EW} : the effective volumetric mass transfer coefficient between the wake and the emulsion phase. Note that the emulsion phase in this model was similar to the liquid-solid fluidized region defined by Bhatia and Epstein (1974). Figure 2.3 illustrated the basic idea of this model:

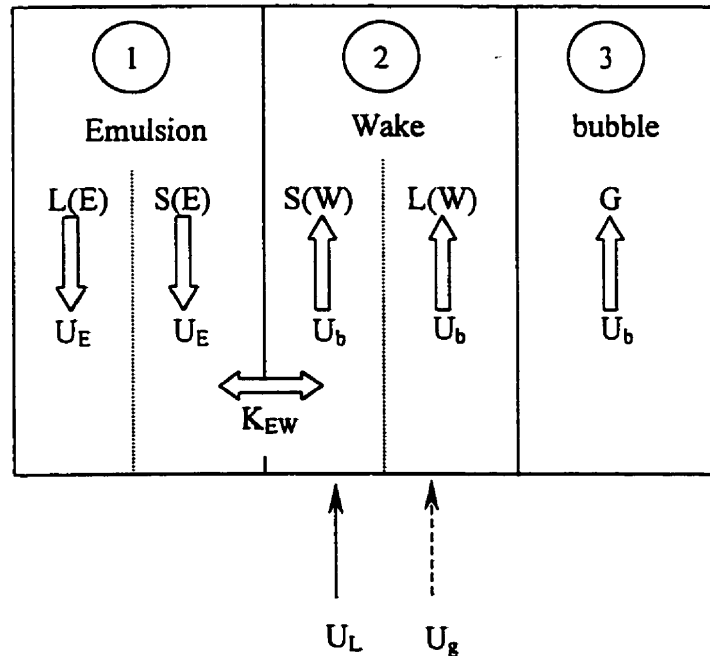


Figure 2.3 Scheme of the modified three-phase counter-current wake model
(from Cassanello *et al.*, 1996)

2.3.3 Solids Mixing and Flow Pattern

The complex behavior of three-phase fluidization is a direct result of the flow structure, and extensive efforts have been made to unveil the flow phenomena. However, most of the previous research are restricted to obtain the time-average results, and very often those studies are qualitative due to the limitation of the measurement techniques employed.

Recent progress in this field is the implementation of non-invasive techniques such as particle image velocimetry (Chen and Fan, 1992; Tzeng *et al.*, 1993; Chen *et al.*, 1994) and radioactive particle tracking (Larachi *et al.*, 1996; Cassanello *et al.*, 1996; Kiared *et al.*, 1997). The major advantage of non-invasive over probe techniques is that it provides a full picture of the flow field for the phase studied rather than local information in the vicinity of the probe. Moreover, intrusive probe techniques introduce an undesirable physical disturbance to the flow and can result in either inaccuracies in the measurements or even permanent impairment of the probes.

The residence time distribution (RTD) obtained from input/output measurements using inert tracers is a common technique that can be used to study the hydrodynamics in a flow reactor. However, it is impossible in practice to determine the flow pattern within the reactor from the RTD. Castellana *et al.* (1980) demonstrated a novel experimental procedure in which radioisotopes and a gamma camera were used to provide detailed quantitative information on the mixing processes within a vessel. The gamma-ray detection system they used was the Searle Pho/Gamma Low Energy Mobile Scintillation Camera. The radioisotope tracer used was Technetium-99m (^{99m}Tc) pertechnetate, a 140-keV γ -emitting radioisotope with a half-life of 6.5 hours. The vessel was placed on the collimator above the camera face. The tracer dissolved in saline was introduced rapidly through the injection tube. As the tracer travelled through the vessel, the camera detected the emission and located its x-y position on the crystal face. The activity (i.e. total counts

per frame time) vs. time curve from selected region-of-interest was thus generated. The activity vs. time data was directly proportional to average tracer concentration within those regions and could be used to characterize mixing mechanisms.

Chen and Fan (1992) used particle image velocimetry (PIV) technique to measure flow properties of a three-phase fluidized bed. PIV consists of laser sheeting, image recording and processing. The laser used in their study was a Lixel 3500, 4 watt Argon Ion laser system and operated in continuous mode. The thickness of the laser sheet was about 2 mm. Image recording was done by a video camera with maximum frame grab speed of 1/30 second. A PIV interrogation software was developed to identify “particle images”, discriminated particle image between different phases, determined holdups of each phase, calculated bubble size, computed displacement between image pairs (from which the instantaneous velocities and accelerations were determined). For liquid and gas velocities of 10.8 cm/s and 0.58 cm/s respectively, they observed that in the free-board region, the combination of bubble wake and liquid drift effects resulted in a highly turbulent liquid flow structure without a dominant flow direction. While for the solid, three circulation cells could be found: one located at about the center region circulated clockwise; another located at the left of the center cell circulated counter-clockwise; and the other relatively small counterclockwise circulating cell located immediately above the center cell.

Chen *et al.* (1994) studied the macroscopic flow structure in 3-D bubble column and gas-liquid-solid fluidization systems using PIV technique. With the increase of the gas velocities, three flow regimes were observed in their study, namely the dispersed bubble regime, the vortical-spiral regime, and turbulent flow regime. The vortical-spiral regime was further classified into four regions (Figure 2.4), from the column center to the wall: central plume region, fast bubble region, vortical-spiral flow region, and descending flow region. The descending flow region was characterized by downward liquid and/or solids movements. The vortical-spiral flow region was characterized by the existence of spiral-downward liquid and/or solids vortices. Adjacent to the vortical-spiral flow region was

the fast bubble flow region, where clusters of bubbles or coalesced bubbles moved upward in a spiral manner with high velocity. The central plume region was surrounded by the fast bubble flow region, and was characterized by a relatively uniform bubble size distribution and less bubble-bubble interaction.

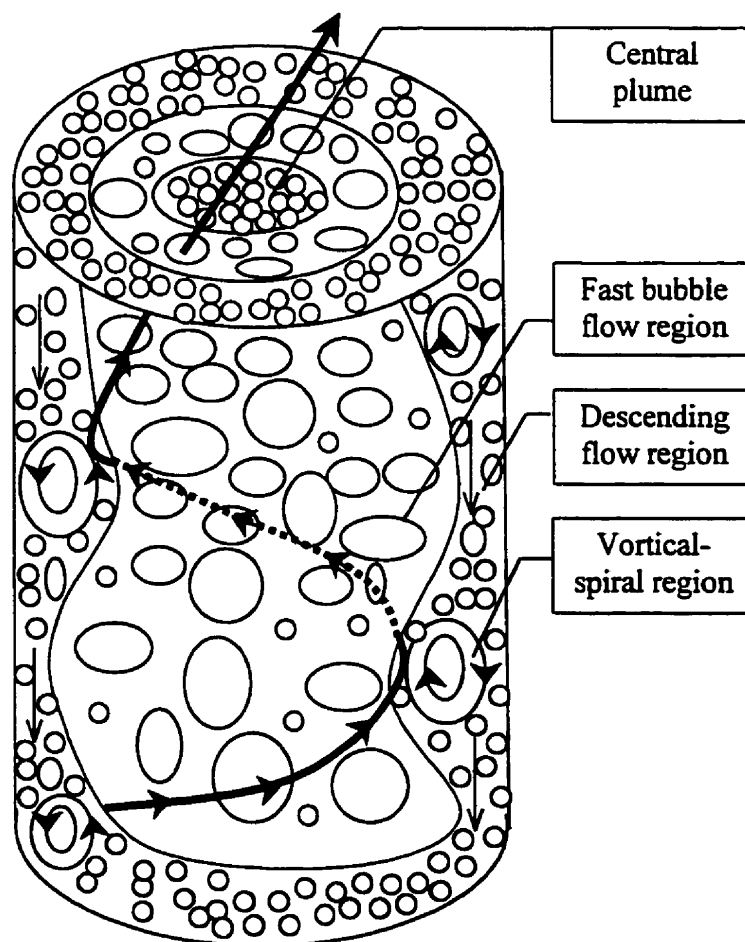


Figure 2.4 Flow structure in the vortical-spiral flow regime in a gas-liquid-solid fluidization system (from Chen *et al.*, 1994)

Lin *et al.* (1985) were the first to use the radioactive particle tracking (RPT) technique to monitor solids motion in fluidized bed system. The tracer particle they used was made of scandium-46 (with a half-life of 84 days) and was closely matched to the size and density of the solid beads in the bed. Twelve photo multiplier tubes incorporating Bicorn 2 in x 2 in (5.08 cm x 5.08 cm) sodium iodide (NaI) crystals were used to continuously monitor the gamma ray emission from the tracer. These twelve scintillation detectors were arranged in a staggered configuration at three different heights with four in each level. Instantaneous solids velocities were obtained by differentiating two successive locations at known data sampling rates. Mean velocity distributions were then summarized in vector diagrams. They found that with a uniform distributor plate and at low air velocities, the solids motion was characterized by a single toroidal vortex with particles ascending near the wall and descending in the central region of a cylindrical bed (AWDC). Increasing the air velocity, a second toroidal vortex in the opposite direction (ascending in center, descending near wall--ACDW) appeared in the upper region of the bed. At sufficiently high velocities, the AWDC vortex disappeared.

Kantzas *et al.* (1999) used a gamma camera to study the hydrodynamic properties of a gas-solid fluidized bed. Their camera was a Siemens Orbiter that had 75 photo-multiplier tubes and a NaI crystal with a diameter of 41 cm. The particle, radio-labeled by ^{99m}Tc (with a half-life of 6.02 hours), had the same physical characteristics as the solid phase, and yielded approximately 1000-1500 counts per second at the camera face. Data was acquired with matrix size of 128 x 128 or 160 x 160. Each image was then processed and the number of counts per pixel was determined. The center of the radioactive particle was calculated through a center of mass calculation to determine the particle position in the 2-D coordinates. The particle trajectory, velocity profile, and probability density functions (PDF) were then obtained. Their results suggested that there were several regions in the bed that correspond to different flow domains within the column. Better mixing (characterized by a wide distribution range of both x- and z-position) could be achieved by a wide particle size distribution.

Zarabi (1998) used the same apparatus to describe particle behavior in a gas-solid fluidized bed. In his study, particle displacement was classified into bounded movement (movement in one direction was the direct result of movement in the other direction) and stream movement (gradual changes in axial direction, which could be a major reason for solid circulation in a fluidized bed). Three different flow zones, namely the entrance zone, circulation zone, and free board were also quantified. He found that the length of the circulation field increased with increasing gas flow rate; while the circulation period decreased with increasing gas flow rate. He also observed that the frequency of particle occurrence decreased toward the bottom and the wall; the horizontal and vertical velocities of the particle were found to be of the same order of magnitude.

Song *et al.* (1999) applied the same technique to three-phase fluidization system. The fluids they used were water and air, the solids were spherical polycarbonate particles—6.35 mm in diameter with a density of 1160 kg/m³. RPT experiments were performed for both free and tethered particles in the same conditions. For a given air velocity, higher water velocity resulted in better solid mixing. Under operating conditions close to minimum liquid fluidization velocity (U_{Lmf}), we found that free and tethered particles had similar movements in the main bed region.

Larachi *et al.* (1995) used radioactive particle tracking (RPT) technique to investigate the solid flow structure in a three-phase fluidized bed. Their system consisted of eight 76 mm x 76 mm uncollimated and unshielded NaI scintillation detectors mounted around the reactor. The particle, made of ⁴⁶Sc radionuclide, was tracked by the detectors, which continuously and simultaneously measured count rates for several hours. The gamma-ray counts were interpreted by a triangulation technique to yield the instantaneous particle position. A calibration was repeated for each experiment when at least one operating condition was changed to evaluate the attenuation of gamma-rays in the bed. They observed that bed-scale large amplitude uninterrupted rising and descending paths were clearly distinguishable. These uninterrupted rising paths were closely related to the

primary bubble wakes. The particle rising velocity distribution was found to be log-normal and independent of the particle size. In addition, three types of solid motions were observed, namely a bubble-like or wake motion (ascending), a convective compensatory or offset motion (descending), and a dispersion or random motion. The two former types of motion were characterized by long amplitude displacements and were responsible for solids gulf streaming. The latter occurred predominantly in the liquid-solid emulsion phase and was due to short range interactions between solids and small bubbles or neighboring liquid and particles.

Later, Larachi *et al.* (1996) extended the observations on the flow structure made on dilute and transparent three-phase systems by Chen *et al.* (1994) to opaque and/or dense three-phase fluidized beds. They identified the following three regions in the vortical-spiral flow regime instead of Chen's four regions: fast-bubble flow region (located at $0 \leq r/R_c \leq 0.63$), annular descending flow region (located at $0.63 \leq r/R_c \leq 1$), and annular vortical flow region which was adjacent to the fast-bubble flow region and often merged with the descending flow region. They also observe that the vertical movements (ascending and descending) were carried out at almost constant axial velocities. Based on the RPT experiments, they pointed out that using axial dispersion model to describe solids movements in a three-phase fluidized bed was not adequate.

Kiared *et al.* (1997) investigated the solids trajectory length and solid residence-time distributions (TLD and RTD) in a three-phase fluidized bed. In their study, RTD was modeled using a two-zone one-dimensional cross-flow multistage stirred reactor model; A macromixing index was also derived from the experimental TLDs for describing solids mixing in the fully developed zone of a three-phase fluidized bed. Their results showed that solids axial mixing was similar having an ascending central region and descending at the wall region, and that solids exchange occurred between these two regions; the RTD predicted by their model closely agreed with their measurements.

CHAPTER 3

Theory

3.1 Solid-Liquid Mass Transfer

The driving force for mass transfer between the solid particle and the surrounding liquid, according to the film theory, is the solute concentration difference between the particle surface (which is equal to the saturation concentration) and the bulk liquid stream. A mass balance over the dissolving solid particle can be expressed as:

$$-\frac{dM}{dt} = k_s A_p (C_{sat} - C_b) \quad (3.1)$$

where dM is the particle weight loss during the experimental time interval dt , k_s is the solid-liquid mass transfer coefficient, A_p is the solid-liquid interfacial surface area, and C_b and C_{sat} are the bulk liquid and saturation concentration at the benzoic acid particle surface respectively. For the case of few tethered benzoic acid particles, C_b is equal to zero.

3.2 Radioactive Particle Tracking

The radioactive particle tracking (RPT) was performed by means of a gamma camera, which is designed to detect gamma radiation. The major components of a gamma camera are a collimator, a sodium iodide detector, and the photomultiplier tubes (Figure 3.1). The gamma radiation from the labeled radioactive particle strikes the face of the collimator mounted to the detector head. The collimator has parallel holes. Only those gamma rays traveling perpendicular to its face are allowed to pass through the collimator. The other gamma rays are stopped by the collimator septa. The gamma rays which pass through the collimator then strike the scintillation crystal (NaI), which changes the energy of the gamma rays into light energy proportion to the amount of energy dissipated within the crystal. The photons are directed to the array of photomultiplier tubes. Each tube detects the flashes of light or scintillations.

The position of the scintillation in the crystal are translated by the photomultiplier tube array and the electronic position logic circuits to a corresponding position on a display screen. Because only the perpendicular gamma rays are allowed to pass the collimator, the scintillation light produced in the crystal shows the same relative positions corresponding to the origin radioactive particle in the column.

The output signal from the gamma camera is analog and must therefore be converted to a digital form by an analog to digital converter. After the position signals are digitized, their position values are used to generate images. The signals are two-dimensional, which presented the x (horizontal) and z (vertical) position in the image. One frame of image data corresponds to all the scintillation events measured during the frame time. As soon as the acquisition of the first image frame is complete, the camera begins to collect a second image on the next frame until the desired number of frames is reached. The time interval between frames is very short (usually in tens of milliseconds), thus the particle trajectory can be reconstructed by interpreting the relative position in successive frames. Instantaneous particle velocity can also be obtained from the particle distance between two successive frames and the time it takes to travel.

The 3-dimensional images can be obtained by using two similar cameras positioned at 90° with respect to each other and programmed to acquire data simultaneously. The data analysis is exactly the same as mentioned above.

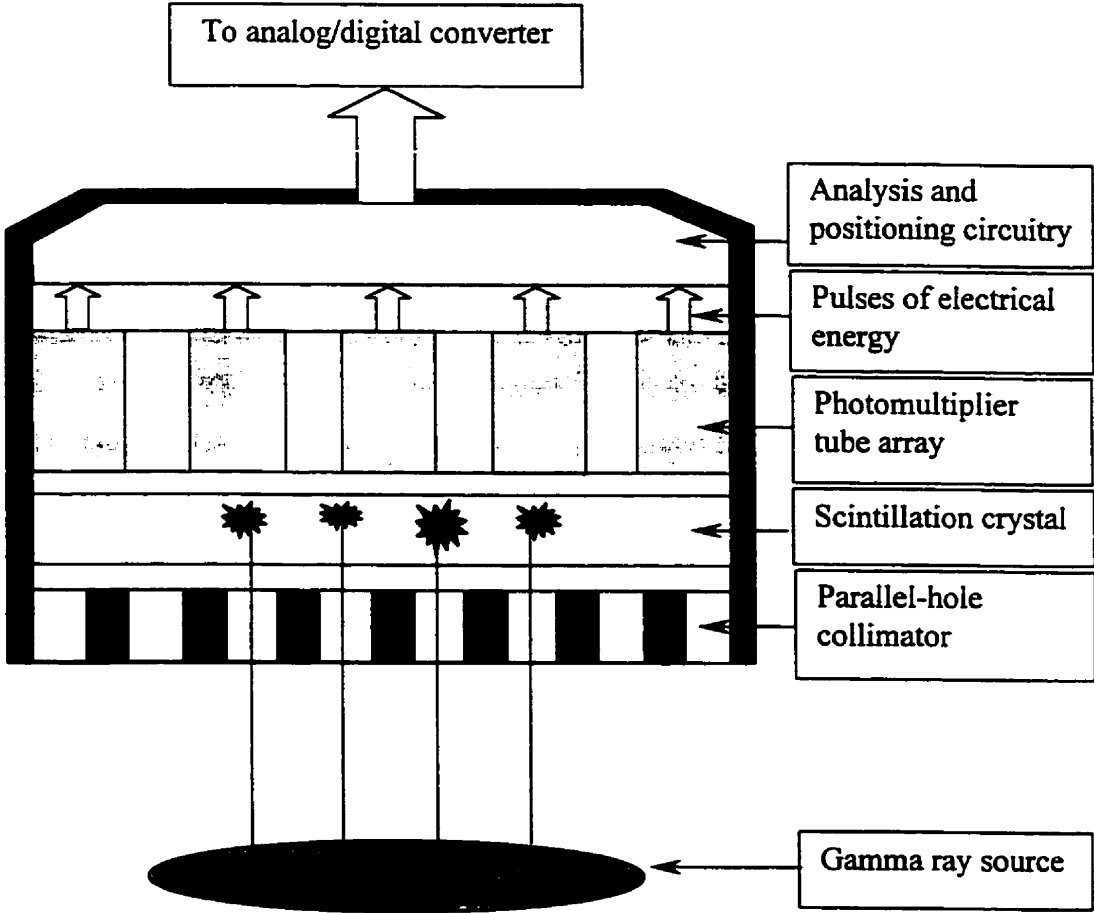


Figure 3.1 Schematic representation of the gamma camera imaging system

CHAPTER 4

Experimental Methods and Data Treatment

Polypropylene (PP) cylindrical particles (for mass transfer and RPT experiments), polycarbonate (PC) spherical particles (for RPT experiments), water, and air were chosen as the experimental system. One 12.7 cm ID Plexiglas column and one 30.48 cm ID PVC column were used in this study. Air was simply vented to the atmosphere. Water was directed to drain for the mass transfer measurements or recycled to the tank for RPT experiments. For both columns, a piece of screen was put on the top of each column outlet to prevent the overflow of solid particles. Pressure fluctuation and mass transfer measurements were performed in the multiphase laboratory with both columns. RPT experiments were performed in Tomographic Imaging and Porous Media (TIPM) laboratory using the smaller diameter column.

4.1 Water System

Water supplied to the lab was filtered and stored in a tank. A centrifugal pump with a recycle loop provided flow to the column. Water flow rate to the larger column was monitored from a pre-calibrated magnetic flow meter, while it was measured with a rotameter calibrated using the pre-calibrated magnetic flow meter for the smaller column (shown in Figure A.1). In TIPM lab, it was read from the flow meter directly.

4.2 Air System

In the multiphase lab, air was obtained from the building supply. The air was filtered to remove oil and small particles. A pressure gauge was placed near the inlet of air distributor. The air flow rate was measured using a linear mass flow meter (KURZ Instruments Inc., Model #: 565-8-04). The flow meter compensated for pressure and

temperature changes to generate a voltage signal proportional to a linear increase in the air flow at standard conditions. The voltage signals were read through a data acquisition board supplied by National Instruments. LabView (Version 4.1) was used to read and display the values in the desired units.

In TIPM lab, air was provided by an air compressor. Before entering the air distributor, it passed through a filter and three pressure regulators to ensure a desired pressure and steady air flow. The flow rate was obtained from rotameter calibrated previously.

4.3 The Columns

The columns consisted of four parts: the liquid calming section, the gas-liquid distributor, the column itself, and the gas-liquid disengaging section.

4.3.1 Smaller Column

Figure 4.1 shows the details of the smaller column (12.7 cm ID). For the polypropylene particles, a settled bed height of 50 cm was maintained for all the experiments. While for the polycarbonate particles, a settled bed height of 54.5 cm was used.

The liquid calming section consisted of a conical section, 14 cm in height at the bottom, and a straight section of 10 cm in height. The water entered the conical section through several holes in the radial direction, then went straight up the distributor. After going through the calming section, the water flow was evenly distributed throughout the diameter of the distributor entrance.

The gas-liquid distributor (shown in Figure B.1), used to ensure a uniform distribution of gas and liquid, had a height of 12.5 cm. Liquid flowed through 109, 2 mm ID tubes extending from the calming section through the distributor to the column-side face of the

distributor. Air entered the distributor from four side ports and exited through 121, 0.6 mm ID orifices.

The column was 12.7 cm ID and 160 cm long. 10 pressure taps (7 for manometers and 3 for pressure transducers) and 3 injection ports (for mass transfer and RPT experiments) were located along the column as indicated by Figure 4.1.

The disengaging section was simply for the gas and liquid separation. It was a piece of plexiglas pipe (30.48 cm ID and 25 cm in height) at the top of the column with a 5.08 cm OD PVC pipe as liquid outlet. A piece of Nylon screen was placed at the column outlet to prevent the overflow of solid particles.

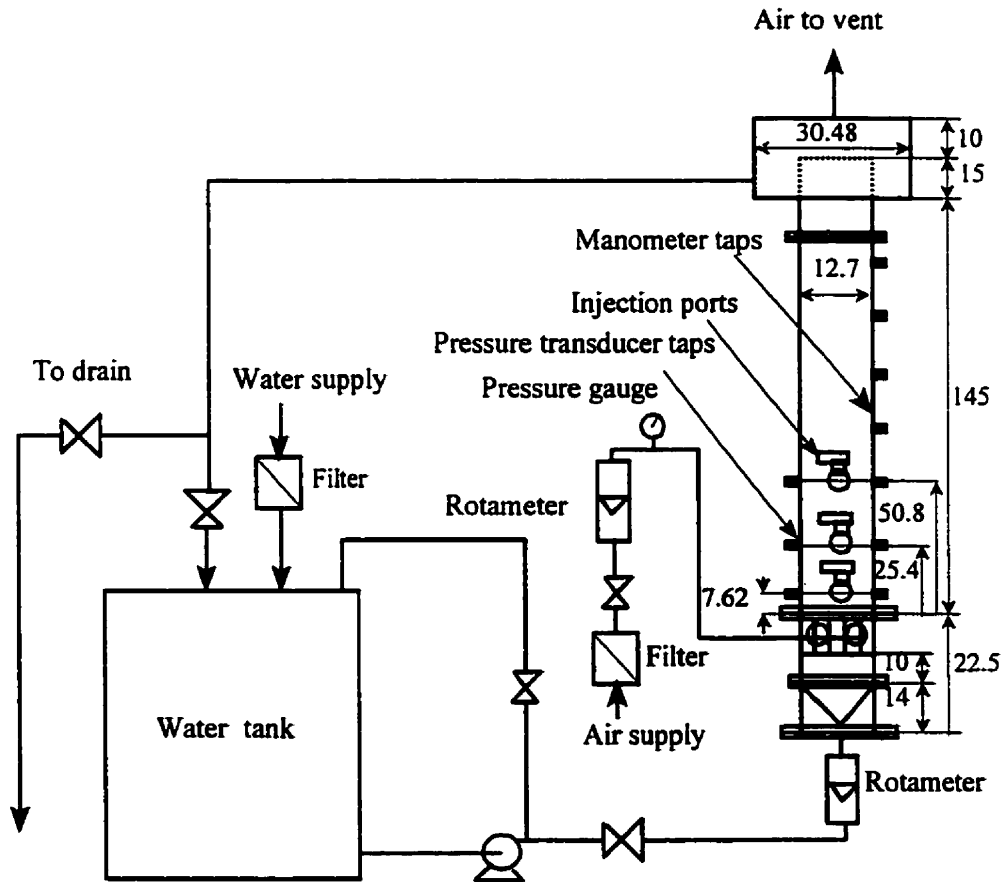


Figure 4.1 Experimental apparatus for mass transfer (dimensions in cm)

4.3.2 Larger Column

Figure 4.2 shows the details of the larger column (30.48 cm ID). A settled bed height of 150 cm was maintained for the polypropylene particles.

The liquid calming section consisted of a cylindrical section made of Plexiglas, 43 cm in height and 30.48 cm ID. The water entered the section through 3 plastic pipes, each with several holes in the radial direction, then went straight up to the distributor. After going through the calming section, the water flow was evenly distributed throughout the diameter of the distributor entrance.

The gas-liquid distributor, used to ensure a uniform distribution of gas and liquid, had a height of 21 cm. Liquid flowed through 109, 6.35 mm ID stainless steel tubes extending from the calming section through the distributor to the column-side face of the distributor. Air enters the distributor from four side ports and exited through 121, 0.6 mm ID orifices. The distributor is essentially a scaled version of the smaller column (see Figure B.1 for details).

The column was 30.48 cm ID and 410 cm long. Pressure measurement ports, pressure fluctuation measurement ports, and injection ports were located along the column as indicated by Figure 4.2. The disengaging section was a piece of PVC pipe (57 cm ID and 60 cm in height). There was a 12 cm OD PVC pipe as liquid outlet at the top of the column. A piece of stainless steel screen was placed at the column outlet to prevent the overflow of solid particles.

4.4 Pressure Fluctuation Measurements for Flow Regime Identification

Pressure fluctuation signals were measured using differential pressure transducers (OMEGA Engineering Inc., Model: 26-005DV) at different locations (7.62 cm and

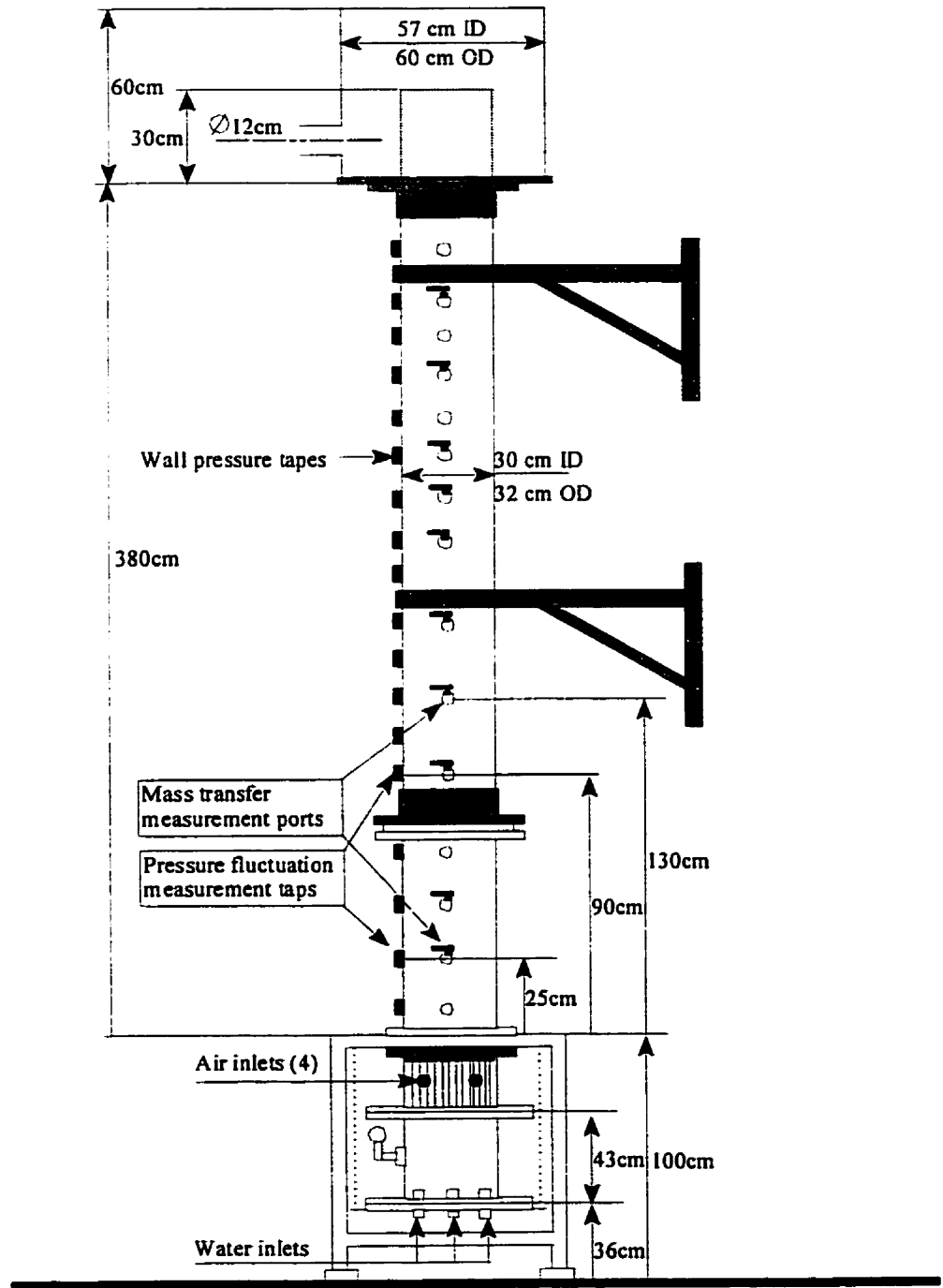


Figure 4.2 30.48 cm diameter column diagram

25.4 cm above the distributor for the smaller column and 25 cm and 90 cm above the distributor for the larger column) in the column. One end of the pressure transducer was connected to a T-fitting to allow purging of air bubbles as well as connection to the pressure tap, and the other end was exposed to air. The transducer produces a voltage signal proportional to the measured pressure. The voltage signals were read through a data acquisition board supplied by National Instruments (Enhanced multifunction I/O Board, Model: AT-MIO-64E-3). The signals were digitized by means of an analog-digital converter. The digitized data was then passed to the LabView program to calculate the power spectral density function (PSDF) on a decibel scale. The program consisted of a Scaled Time Domain Window.vi (implemented with a Hanning Window as the signal filter), an Auto Power Spectrum.vi and a Spectrum Unit Conversion.vi. The decibel scale was later converted to linear scale. Based on the work of Fan *et al.* (1986) and Jakher (1998), the differences in the PSDF shape were used to identify the flow regimes and their transition. Flow regimes identified by this method were also confirmed by visual observation.

4.5 Particle Properties

The following particle properties were measured (Table 4.1). Minimum liquid fluidization velocity (U_{Lmf}) for the PP cylinders and PC spheres was measured as shown in Appendix C. For PP cylinders, U_{Lmf} was 1.2 cm/s and for PC spheres, U_{Lmf} was 1.68 cm/s.

Table 4.1 Physical properties of solid particles

particle	shape	diameter (mm)	length (mm)	sphericity (ϕ)	equivalent diameter (mm)	density (g/cm ³)
PP	cylindrical	3.438	4.243	0.870	4.221	1.22
benzoic acid active particle	cylindrical	3.647	4.542	0.869	4.492	1.16
PC	spherical	6.35	6.35	1.000	6.35	1.16

4.6 Mass Transfer Experiments

4.6.1 Preparation of Active Particles

Benzoic acid dissolution in water is a common choice in mass-transfer studies due to the low solubility of benzoic acid in water, the well-known physical properties, the relative ease to pelletize, and the chemical stability of the acid. The benzoic acid used was analytical reagent grade made by British Drug Houses Ltd. One end of the Nylon strings (approximately 80 cm in length for smaller column and 100 cm in length for larger column) were put in the cylindrical mold made of an aluminum plate. The mold has a slightly larger diameter than polypropylene (PP) particles. Benzoic acid powder was melted and poured into the mold. After cooling down, the benzoic acid pellets were removed from the mold and shaped manually into the same size as polypropylene particles. The pellets were labeled afterwards. Their weight, size (including diameter and height), and string length were then recorded for the calculation of mass transfer coefficient. Typical properties of the active benzoic acid pellet and polypropylene particles are shown in Table 4.1.

4.6.2 Experimental Procedure

Both distributor and main bed regions were under investigation in this study. Two injection ports, located at 7.62 cm and 50.8 cm above distributor for smaller column and 25 cm and 130 cm above distributor for larger column, were used. A $3/8''$ (9.52 mm) hollow steel tube was used to insert the active particles through the injection ports to the bed. A rubber stopper near the tip was used to prevent water leakage and allowed on-line insertion. The tethered active particle was first put in the tube right after the stopper. When the tube was inserted into the center of the column, the rubber stopper was pushed forward and the particle started to move in the bed within the limits of the tether. A stopwatch started to record the time simultaneously. Approximately 10 minutes was

maintained for all the runs. At the end of 10 minutes, the string was retracted and the stopwatch stopped. The tube was quickly removed from the bed (particle insertion and removal required approximately 5 to 10 seconds and was considered negligible to the total time). Particles were left to dry overnight and then weighed and measured the next day. Note that for all the runs, the string between benzoic acid particle and the stopper was kept at a length of $\sqrt{2} R_c$, which is 9 cm for smaller column and 21 cm for the larger column.

During the process, a thermocouple was placed in the top of the column to monitor the temperature. Again, a LabView program was used to monitor the temperature.

4.7 Radioactive Particle Tracking Experiments

Radioactive particle tracking experiments were performed in the TIPM laboratory. The gamma camera has 75 photo-multiplier tubes arranged in hexagonal array, and a NaI crystal with a diameter of 41 cm (shown in Figure 4.3). Technetium (^{99m}Tc) with a half-life of 6.02 hours was used to tag the particle. ^{99m}Tc was chosen because of its availability, cost effectiveness, energy of emission and short physical half life which made the waste disposal safer and easier.

The Nuclear MAC gamma camera computer was used to acquire, display and process the images. The software follows the standard Macintosh user interface guidelines. It operates through the familiar menus, windows, mouse controls, and dialog boxes. The Nuclear MAC supports the standard image formats of the Macintosh, so images can be displayed using other standard programs (Kantzas *et al.*, 1999).

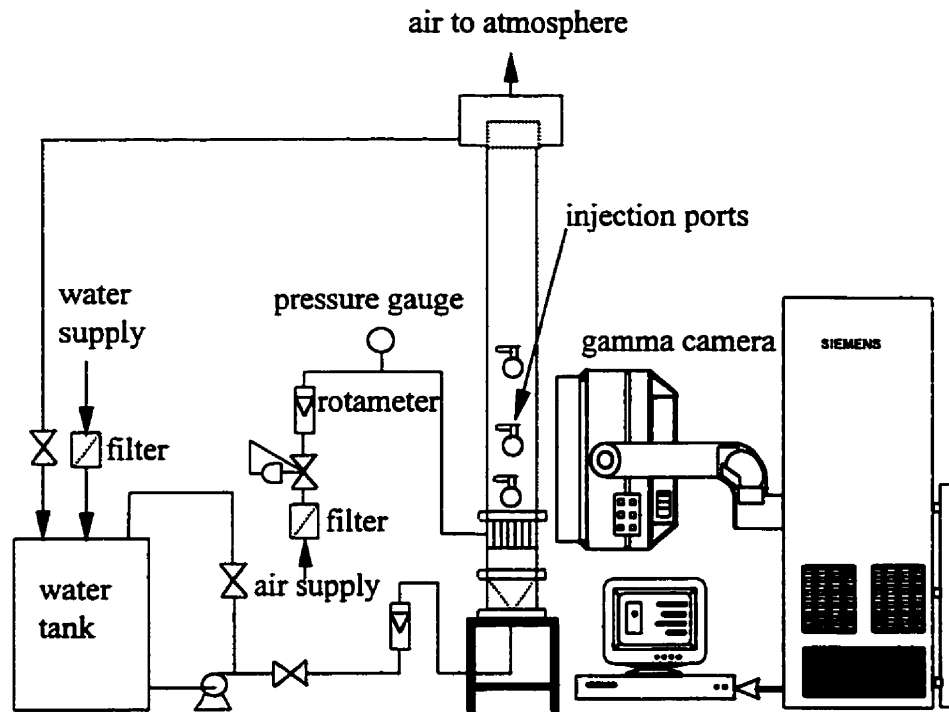


Figure 4.3 Experimental apparatus for RPT

4.7.1 The Radioactive Particle

A small hole was drilled into the particle, which had the same physical properties as the solid phase in the bed. ^{99m}Tc was injected into the hole and then sealed using “Hot Stuff” instant glue. The radiolabeled particle was put directly into the column for free particle tracking. A nylon thread was also glued to the hole for tethered particle tracking. The same injection technique used in the mass transfer study (Section 4.6.2) was used to inject the tethered particle.

4.7.2 Experimental Procedure

1. Place the column next to the camera.
2. Adjust the head of the camera to the desired position of the column.

3. Mark the wall and distributor plate or a specific z-position in the column with a radioactive marker.
4. Set the liquid and gas flow rates to the desired level and allow the flow to stabilize.
5. Inject the radioactive particle into the bed.

When the labeled particle appeared in the monitoring screen, data acquisition was started. 128 x 128 matrix was used in this study. Each pixel was 3.43 mm x 3.43 mm in size. Each set of data consisted of 1000 frames.

4.7.3 Data Treatment

The data collected in the experiment was transferred to a workstation. A FORTRAN program written by Amit Bhargava and Jinwen Chen was used to process the raw image data. Details on the data treatment are given in Appendix E.

CHAPTER 5

Results and Discussion

In a three-phase fluidized bed, solid-liquid mass transfer and flow patterns are strongly related to the operating flow regimes. Three flow regimes can be identified based on the bubble flow behavior in a three-phase fluidized bed: the dispersed bubble, the coalesced bubble, and the slugging regime. According to the work of Chen *et al.* (1994), the coalesced bubble regime can be further divided into two sub-regimes: vortical-spiral regime at intermediate gas velocity and turbulent flow regime at high gas velocity. In this study, flow regime identification was first examined to determine the hydrodynamic environment under which the solid-liquid mass transfer, solids dynamics and flow patterns were studied.

5.1 Flow Regime Identification

Polypropylene cylinders were used in flow regime identification experiments shown below. Pressure fluctuation signals from main bed region were taken and the power spectral density function (PSDF) were calculated using LabView programming. Based on the work of Fan *et al.* (1986) and Jakher (1998), the differences in the PSDF were used to identify the flow regimes and their transition.

For the smaller column ($D_c = 12.7$ cm) operating under $U_L = 2.0$ cm/s, at $U_g = 0.5$ cm/s, the bubble size was observed to be relatively small and uniform, indicating the column was operating under dispersed flow regime. At $U_g = 1.5$ cm/s, in the column center, some bubbles coalesced to form larger ones (2 - 3 cm in diameter) and formed a bubble cluster rising spirally, indicating it was operating in vortical-spiral flow regime. At $U_g = 3.0$ cm/s, clusters of bubbles moved upward in a spiral manner with high velocity in the column center were observed, indicating the column was operating under turbulent flow regime.

Figure 5.1, 5.2 and 5.3 show the typical pressure fluctuation signals from the smaller column (main bed region) operating under different flow regimes. The signals appear similar in character except with respect to their magnitudes: they all fluctuate around a mean value within a narrow range. The PSDF's of these signals shown in Figures 5.4, 5.5 and 5.6 permit us to distinguish between the different flow regimes. At $U_g = 1.0$ cm/s (Figure 5.4), the PSDF is fairly small and only few insignificant peaks exist for the whole range of frequency. At $U_g = 2.0$ cm/s (Figure 5.5), the PSDF has a narrow peak near 7 Hz. While at $U_g = 3.0$ cm/s (Figure 5.6), the PSDF is much larger and there exists a distinct broad peak between 0 to 10 Hz. From this general trend of the appearance of a peak located near 7 Hz indicates the onset of the transition or vortical-spiral flow regime. With increased PSDF intensity as well as a broadening of the peak, the onset of the turbulent flow regime can be distinguished. Currently there is not any quantitative standard to classify the flow regimes based on the magnitude of the peak.

The pressure fluctuation and PSDF of larger column (main bed region) display the similar trend (Figures 5.7 to 5.9) except that the peak of PSDF is located around 2 Hz. In this work, we combined visual observations with the PSDF's to determine the operating flow regimes for the mass transfer and flow pattern studies.

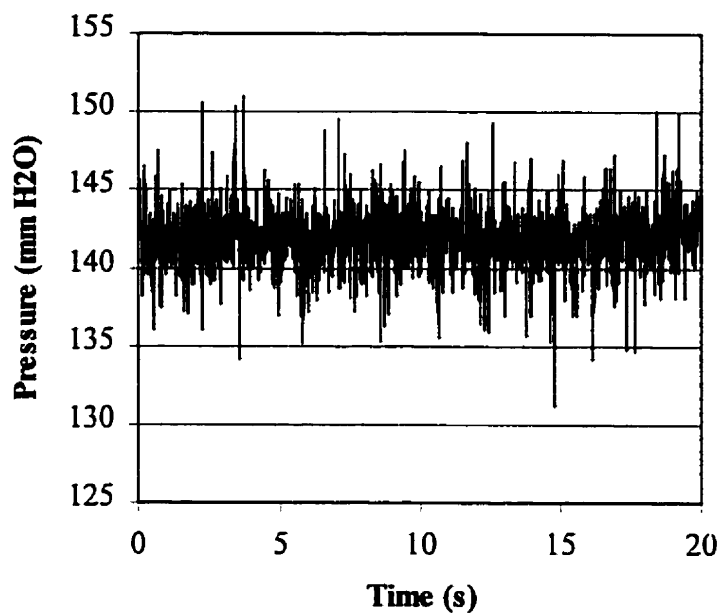


Figure 5.1 Pressure fluctuation signals for the dispersed flow regime
($U_L = 2$ cm/s, $U_g = 1$ cm/s, $D_c = 12.7$ cm)

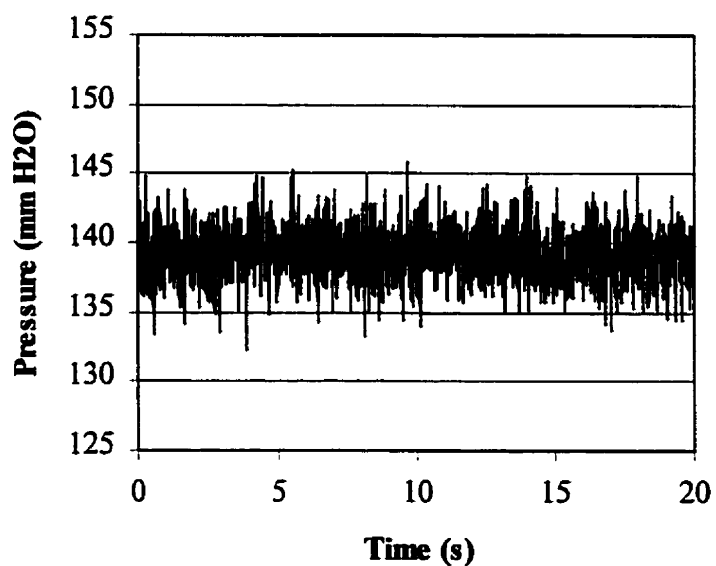


Figure 5.2 Pressure fluctuation signals for the vortical-spiral flow regime
($U_L = 2$ cm/s, $U_g = 2$ cm/s, $D_c = 12.7$ cm)

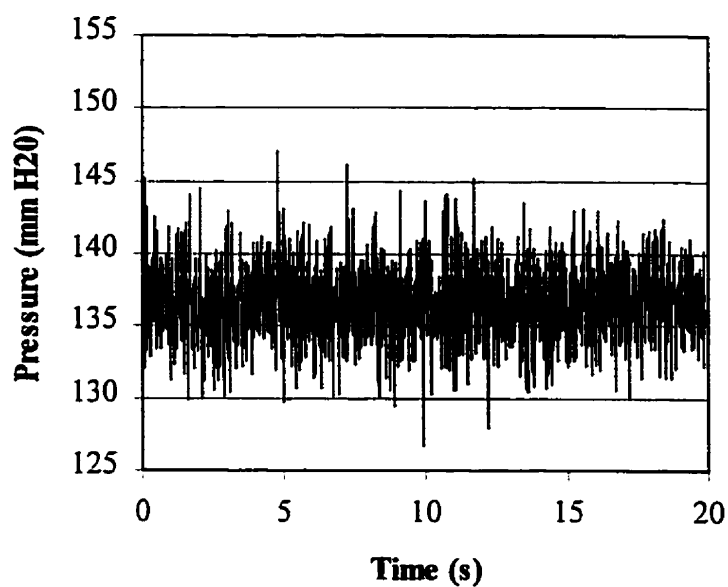


Figure 5.3 Pressure fluctuation signals for the turbulent flow regime
($U_L = 2$ cm/s, $U_g = 3$ cm/s, $D_c = 12.7$ cm)

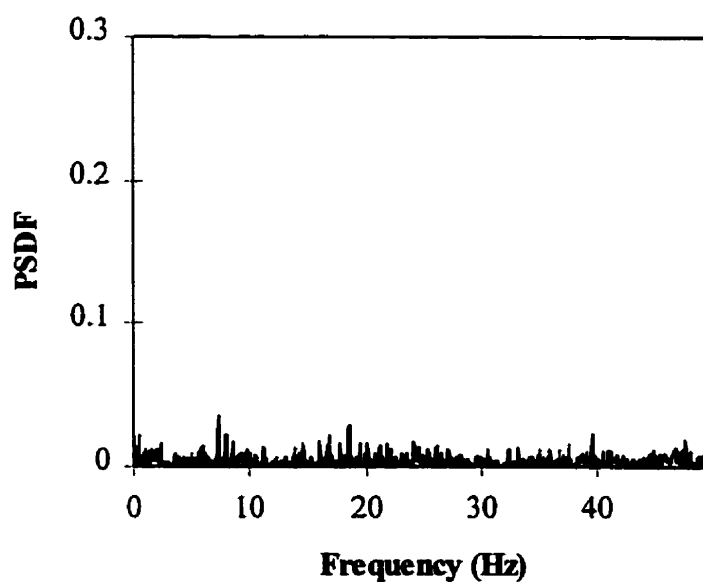


Figure 5.4 Power spectral density function for the dispersed flow regime
($U_L = 2$ cm/s, $U_g = 1$ cm/s, $D_c = 12.7$ cm)

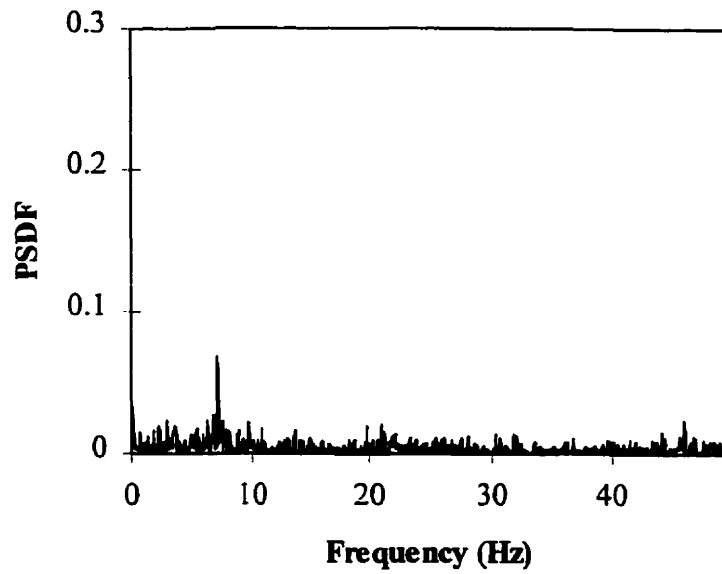


Figure 5.5 Power spectral density function for the vortical-spiral flow regime
 ($U_L = 2$ cm/s, $U_g = 2$ cm/s, $D_c = 12.7$ cm)

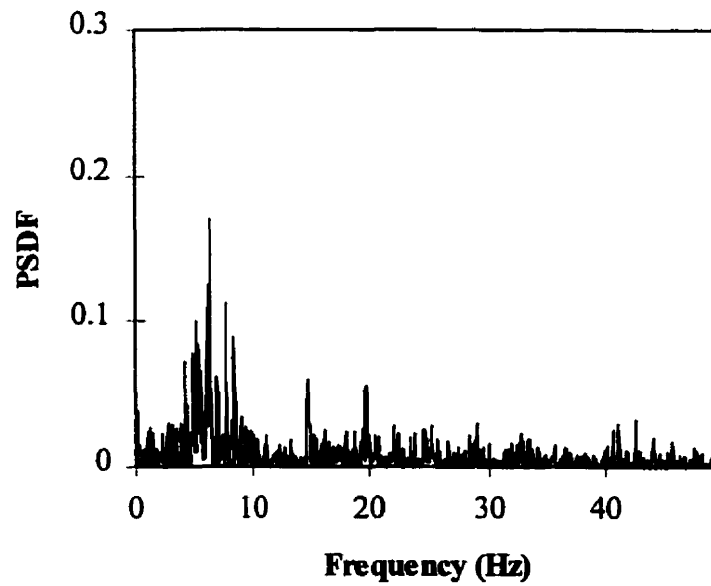


Figure 5.6 Power spectral density function for the turbulent flow regime
 ($U_L = 2$ cm/s, $U_g = 3$ cm/s, $D_c = 12.7$ cm)

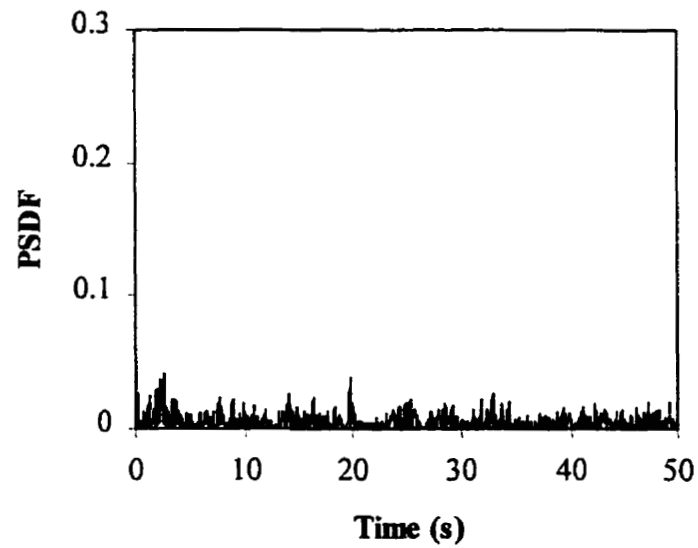


Figure 5.7 Power spectral density function for the dispersed flow regime
($U_L = 2$ cm/s, $U_g = 0.98$ cm/s, $D_c = 30.48$ cm)

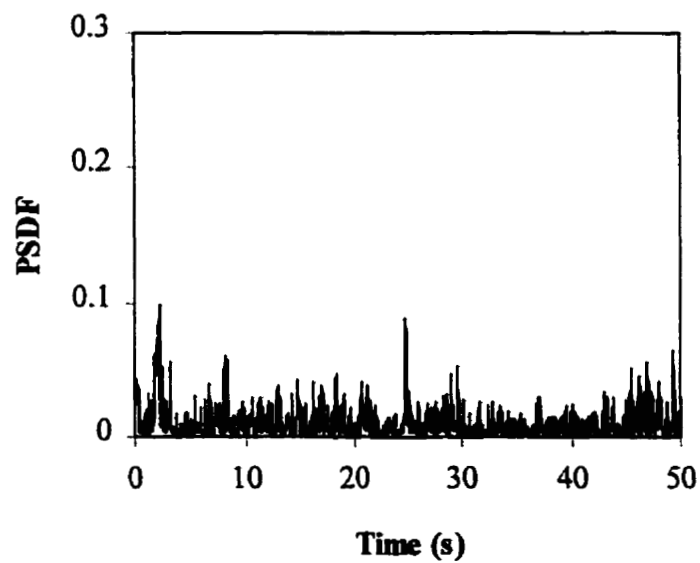


Figure 5.8 Power spectral density function for the vortical-spiral flow regime
($U_L = 2$ cm/s, $U_g = 1.99$ cm/s, $D_c = 30.48$ cm)

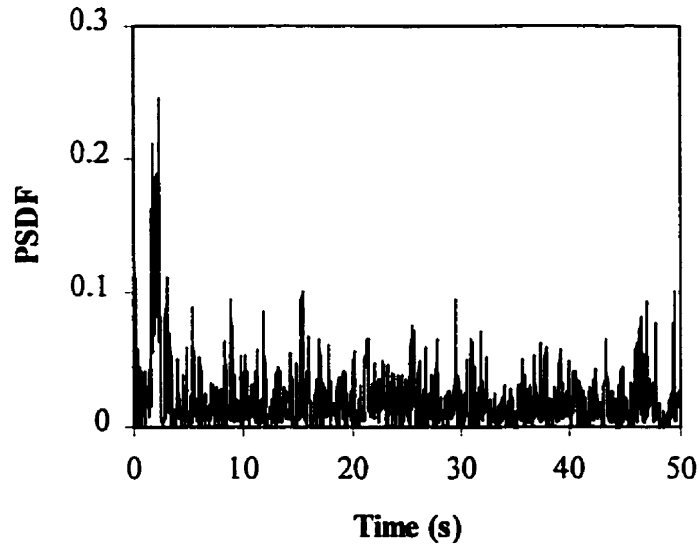


Figure 5.9 Power spectral density function for the turbulent flow regime
 ($U_L = 2 \text{ cm/s}$, $U_g = 2.98 \text{ cm/s}$, $D_c = 30.48 \text{ cm}$)

5.2 Liquid-Solid Mass Transfer

Liquid-solid mass transfer experiments were carried out in two columns (12.7 cm ID and 30.48 cm ID) to study the scale up effects. A dissolution technique with tethered benzoic acid pellets was used (inert particles were polypropylene cylinders). For both columns, a tether length of $\sqrt{2} R_c$ (9 cm for smaller column and 21 cm for the larger column) was maintained for all the runs. As shown in Table 5.1, the experiments were conducted at two locations, one in the distributor region and the other in the main bed region. Three liquid velocities and three gas velocities were used in this study. According to flow regime identification, for a constant gas velocity of 1 cm/s, the columns were operated in dispersed flow regime for the three liquid velocities. While for a constant liquid velocity of 2 cm/s, with the increase of air velocity from 1 cm/s to 2 cm/s and to 3 cm/s, the columns were operated in dispersed, vortical-spiral (or transition), and turbulent flow regimes respectively. The operating parameters with their flow regimes are shown in Table 5.1.

Table 5.1 Mass transfer experimental operating parameters

Column diameter (D_c), cm	Particle injection location		Superficial liquid velocity (U_L), cm/s	Superficial gas velocity (U_g), cm/s	Operating flow regime
	Above the distributor (H_p)	H_p / D_c			
12.7	7.62 cm	0.6	2.0, 3.0, 4.0	1	Dispersed
			2.0	2	Vortical-spiral
			2.0	3	Turbulent
12.7	50.8 cm	4	2.0, 3.0, 4.0	1	Dispersed
			2.0	2	Vortical-spiral
			2.0	3	Turbulent
30.48	25 cm	0.8	2.0, 3.0, 4.0	1	Dispersed
			2.0	2	Vortical-spiral
			2.0	3	Turbulent
30.48	130 cm	4.3	2.0, 3.0, 4.0	1	Dispersed
			2.0	2	Vortical-spiral
			2.0	3	Turbulent

The mass transfer coefficient was determined using Equation 3.1 with $C_b = 0$. The detailed results are shown in Appendix D. Note that in this study, three repetitions were performed for each set of operating parameters. For comparison purposes, the Sherwood number correlation proposed by Nikov and Delmas (1987, Equation 2.6) was also calculated. Correlation was computed for the average experimental conditions for six repetitions (three repetitions from the distributor region and three repetitions from the main bed region).

5.2.1 Effect of Liquid Velocity on Sherwood Number

5.2.1.1 Smaller Column

As Figure 5.10 indicates, for a gas velocity of 1 cm/s, the liquid-solid mass transfer coefficients are independent of liquid velocities for both distributor and main bed region. This is in agreement with previous work of Arters (1984), Arters and Fan (1986, 1990),

Prakash *et al.* (1987), and Dutta and Pangarkar (1993). There is also no significant difference between the distributor and main bed region. This may correspond to the uniform bubble sizes and their rising velocities since all experiments shown in Figure 5.10 were in the dispersed regime. The magnitude of Sherwood numbers from this work is close to that of Nikov and Delmas. Note that Nikov and Delmas used a tethered particle electrochemical technique. The columns they used were 5 and 9.4 cm in diameter (see Table 2.1).

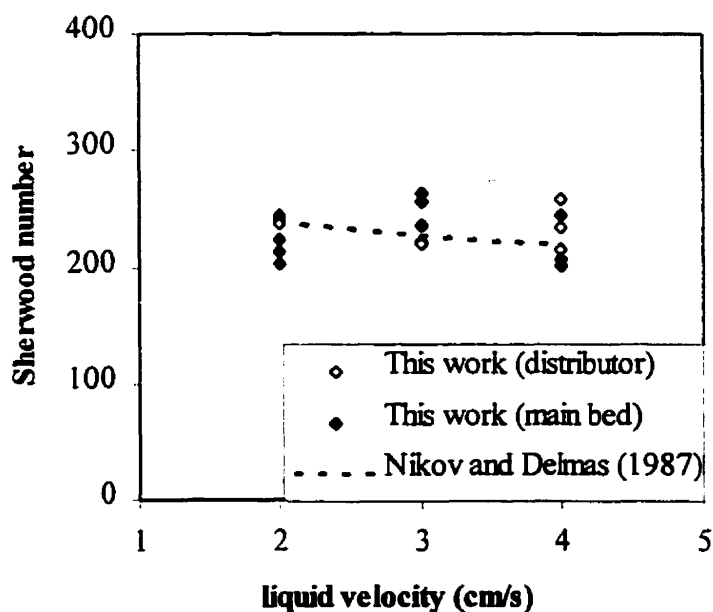


Figure 5.10 Effect of liquid velocity on Sherwood number
($U_g = 1 \text{ cm/s}$, $D_c = 12.7 \text{ cm}$)

5.2.1.2 Larger Column

As Figure 5.11 indicates, for a gas velocity of 1 cm/s, the liquid-solid mass transfer coefficients are independent of liquid velocities for both distributor and main bed region. In the main bed region, the mass transfer coefficient is always higher than that of

distributor region for all the runs, indicating a more turbulent environment. The magnitude of Sherwood numbers from this work at distributor region is close to that of Nikov and Delmas (1987). While at the main bed region, it is much higher than that of Nikov and Delmas, indicating there is a scale up effect.

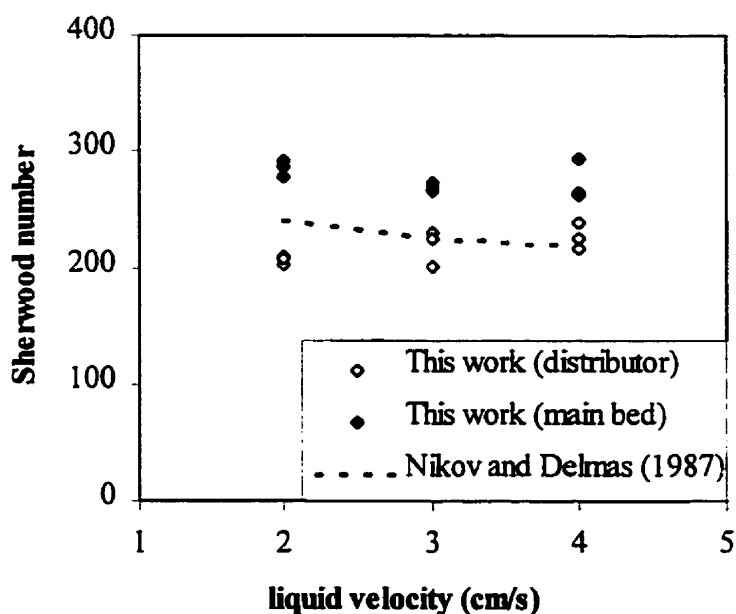


Figure 5.11 Effect of liquid velocity on Sherwood number
($U_g = 1$ cm/s, $D_c = 30.48$ cm)

5.2.2 Effect of Gas Velocity on Sherwood Number

5.2.2.1 Smaller Column

Figure 5.12 shows the effect of gas velocity on Sherwood number. In the main bed region, the Sherwood number increases with the increase of gas velocity, which is consistent with previous observations in the literature. Note that when the flow regime changes from dispersed to vortical-spiral, the increase of Sherwood number is higher than

when it changes from vortical-spiral to turbulent. This is probably because, even in vortical-spiral regime, the bed is highly turbulent compared to dispersed regime. While in the distributor region, the Sherwood number decreases slowly when the gas velocity is increased. This coincides with the results of Nishikawa *et al.* (1976) and Prakash *et al.* (1987), who observed that over certain range of gas velocity, the mass transfer coefficient decreased with increasing gas velocities. This decrease in Sherwood number is presumed to be caused by the formation of large gas jets which bypassed most of the distributor region. Catros *et al.* (1985) proposed that this region be divided into a gas jet sub-region where there were few particles and another sub-region where there were few gas bubbles. The energy provided by the gas was therefore not fully utilized near the distributor. In the main bed region, the magnitude of Sherwood numbers from this work are close to that of Nikov and Delmas (1987).

5.2.2.2 Larger Column

Figure 5.13 shows the effect of gas velocity on Sherwood number for larger column. As with the liquid velocity, the Sherwood numbers in the main bed region are higher than those in the distributor region. Sherwood number also increases with the increase of gas velocity in main bed region. In contrast to the results of smaller column (Figure 5.12), Sherwood numbers in larger column increase with the increase of gas velocity in the distributor region. With the increase of column diameter, the effect of distributor on hydrodynamics in a three-phase fluidized bed containing low-density particles is overcome, and the gas bypassing problem can be eliminated. It should be noted here that the distributors used in the smaller and larger columns are essentially identical in design. The magnitude of Sherwood numbers from this work is much higher than that of Nikov and Delmas (1987) in the main bed region.

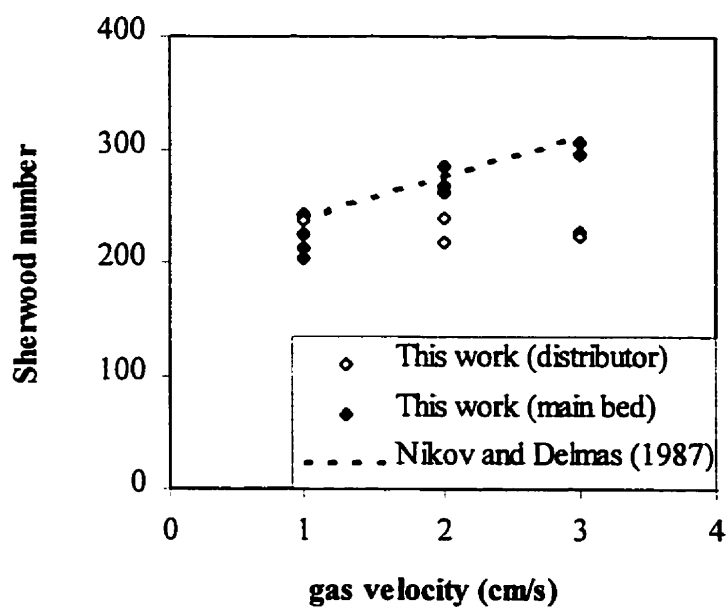


Figure 5.12 Effect of gas velocity on Sherwood number
($U_L = 2$ cm/s, $D_c = 12.7$ cm)

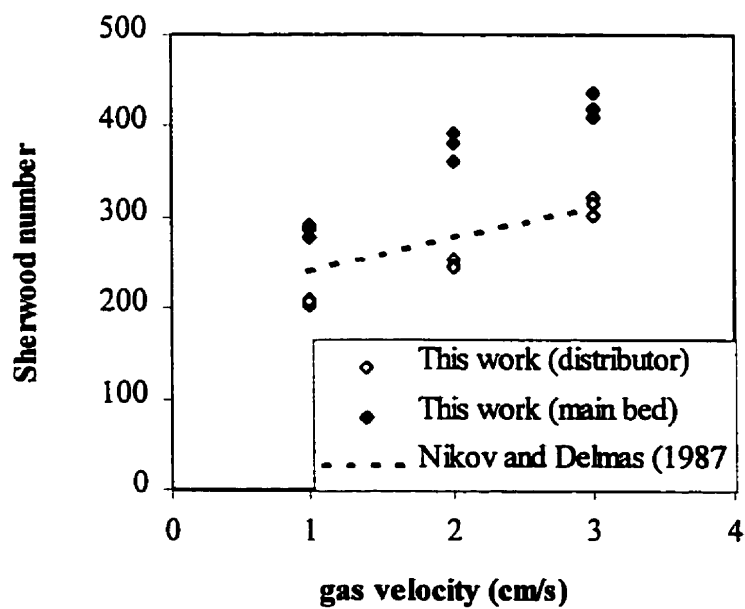


Figure 5.13 Effect of gas velocity on Sherwood number
($U_L = 2$ cm/s, $D_c = 30.48$ cm)

5.2.3 Scale up Effects

Figure 5.14 to 5.17 show the effect of scale up on Sherwood number. There are not significant effects on Sherwood number of scale up for a given gas velocity (1 cm/s) and increasing liquid velocity in the distributor region (Figure 5.14). In the main bed region, a scale up effect is observed, and the larger column has a higher Sherwood number (Figure 5.15). For a given liquid velocity of 2 cm/s, with increasing gas velocity, in the distributor region, the magnitude of Sherwood number at lower gas velocities (1 & 2 cm/s) is similar in the two columns, but at higher gas velocity (3 cm/s) the effect of scale is quite significant (Figure 5.16). The trends observed in Figure 5.16 for the large and small columns are quite different. Sherwood number decreases with increasing gas velocity in the small column while a sharp increase with gas velocity is observed in the large column. In the main bed region, the larger column has a much higher Sherwood number (Figure 5.17). Liquid phase turbulence has a pronounced effect on local Sherwood number, as pointed out by Gogoi and Dutta (1996), Dutta and Pangarkar (1993) and Jadhav and Pangarkar (1991). Increases column diameter will increase the turbulence intensity (see Equation 2.12).

Figure 5.18 shows the ratio of mass transfer coefficient over $D_c^{0.31}$ obtained with the two columns for various superficial gas and liquid velocities in the main bed region. It can be seen that the values distribute between approximately 0.8 and 1.1. The factor of $D_c^{0.31}$ was obtained by comparing the $(k_s/D_c^n)_{D_c=30.48}/(k_s/D_c^n)_{D_c=12.7}$ to one using a sum of squared errors for all mass transfer data points, where n is the scale up factor. Values of n from 0.26 to 0.37 were investigated with 0.31 giving the minimum error. It should be noted that for $k_s \propto D_c^{0.26}$ proposed by Dutta and Pankargar (1993) the value for the ratio $(k_s/D_c^{0.26})_{D_c=30.48}/(k_s/D_c^{0.26})_{D_c=12.7}$ ranged from 1.0 to 1.5. The scale up factor of $D_c^{0.31}$ should, however, be verified with longer tether lengths.

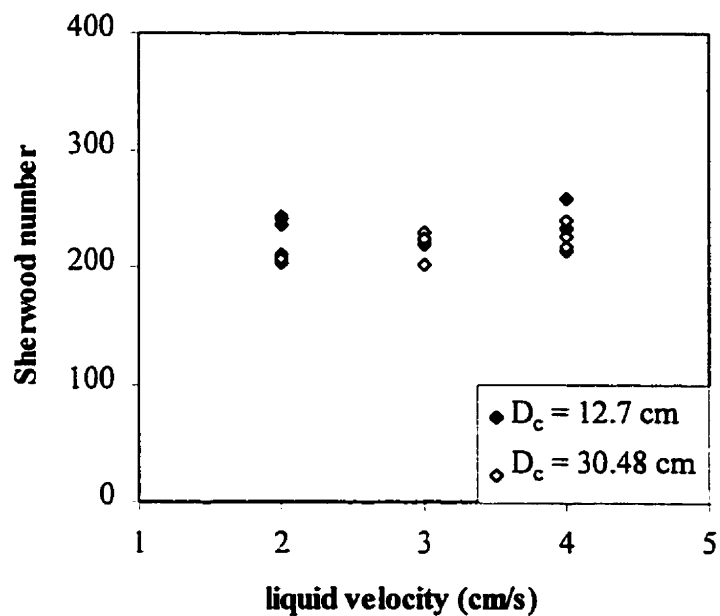


Figure 5.14 Scale up effect on the Sherwood number ($U_g = 1$ cm/s, distributor)

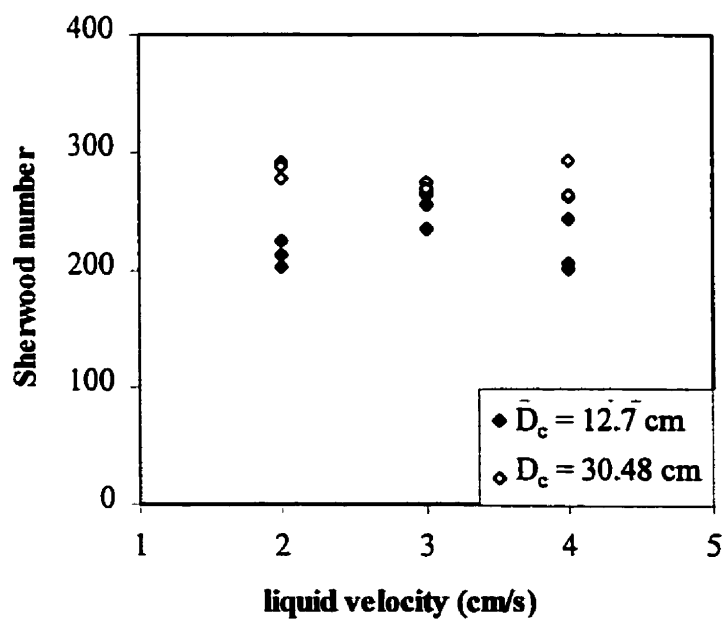


Figure 5.15 Scale up effect on Sherwood number ($U_g = 1$ cm/s, main bed)

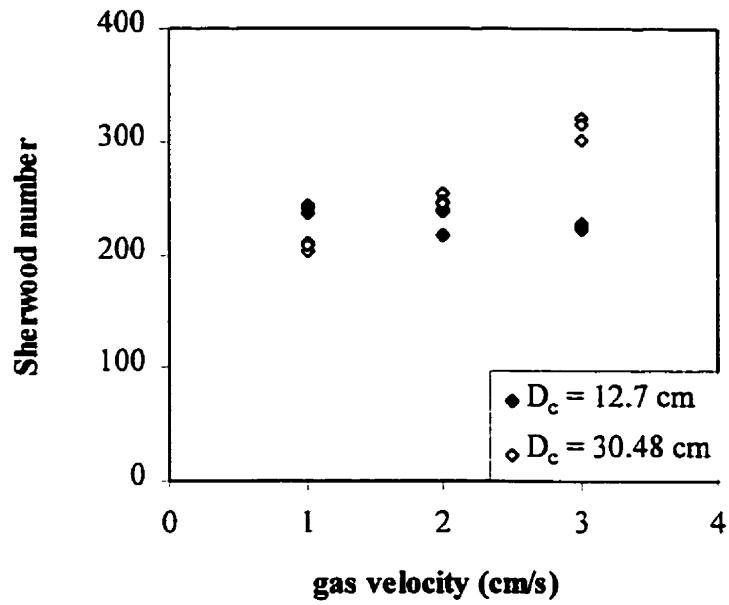


Figure 5.16 Scale up effect on Sherwood number ($U_L = 2$ cm/s, distributor)

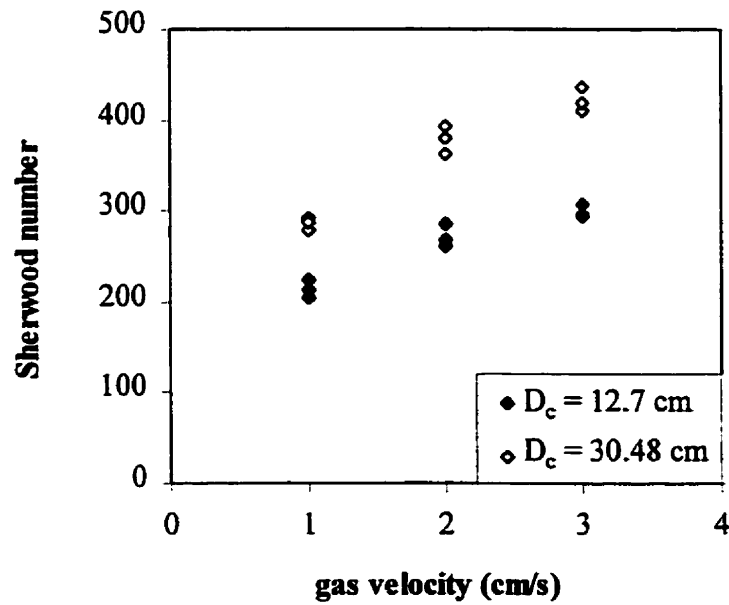


Figure 5.17 Scale up effect on Sherwood number ($U_L = 2$ cm/s, main bed)

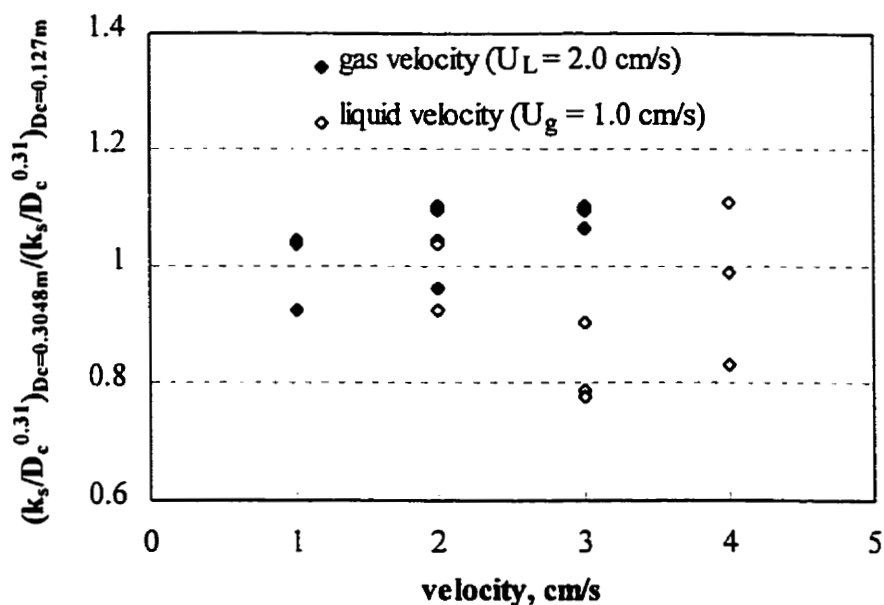


Figure 5.18 Comparison of $k_s/D_c^{0.31}$ obtained with two columns

5.3 Solid Dynamics

Solid dynamics were studied using the radioactive particle tracking technique as outlined in Section 4.6. The operating parameters for experiments are shown in Table 5.2 and all experiments were conducted in the 12.7 cm diameter column. The main purpose of Set 1 was to study the free and tethered particle movements in the whole column, which included the distributor region and free-board region. Set 2 focused on the flow pattern and the difference between free and tethered particles in the main bed region. Set 3 examined the effect of flow pattern and the difference between free and tethered particle movements in the dispersed and vortical-spiral flow regimes in the main bed section. Particle properties were outlined in Table 4.1.

Table 5.2 Radioactive particle tracking experimental operating parameters

Experiment	Set 1	Set 2	Set 3	
Inert particle	PC sphere	PC sphere	PP cylinder	
Radioactive particle state	Free and 6.35 cm tether	Free, 9 cm & 19cm tether	Free, 9 cm & 19cm tether	
Superficial liquid velocity (cm/s)	1.68 & 2.08	2.69	2.20	
Superficial gas velocity (cm/s)	1.46	2.16	0.82	2.0
Scanning area (cm above distributor plate)	0-32 & 24-65	29-70	29-70	
Injection port (cm above distributor plate)	7.62 & 25.4	50.8	50.8	50.8
Operating flow regime	Vortical-spiral	Vortical-spiral	Dispersed	Vortical-spiral

5.3.1 Particle Tracking of Polycarbonate Beads over the Entire Column (Set 1)

The camera was first placed in front of the distributor-main bed region and then moved up to main bed-free board region. For both free and tethered (tether = 6.35 cm) particles, 12 sets of data (each consisting of 1000 frames) with a frequency of 50 Hz were collected for each flow rate and camera position. The data acquisition continued for several hours.

5.3.1.1 Free Particle Movements

Figure 5.19 and 5.20 show the x-z positions of free particles from RPT experiments. Although the trajectory analysis is shown in two dimensions (x- and z-), some interesting observations can still be made. The particle trajectory of Figure 5.19 indicates that very often the particle is caught oscillating in a very narrow part of the column. Most of these events occur at the lower part of the column. The only place that such oscillations are not evident is at the very top of the column scanning area (free-board region under these operating conditions). The particles in the free-board region drifted widely in the x-direction before they settled down as confirmed by visual observations. At the lower liquid velocity (Fig. 5.19), the particle seldom reached the distributor plate nor the wall of the column. This suggests a poor solids mixing. At the higher liquid velocity (Figure 5.20), the particle made larger movements between images. Also the horizontal particle oscillations appeared wider. The particle covered a wider part of the column and appeared on several occasions to travel close to the wall and the distributor plate, indicating better mixing was achieved. There are some similarities between the two trajectory profiles, such as the oscillating movements and some stagnant zones (areas A and B as shown). At higher liquid velocity (Figure 5.20), the particle started a new ascending path whenever it approached the distributor thus completed a circulation journey (area C). However, this was not seen at lower liquid velocity (Figure 5.19).

In one of the runs in Fig. 5.19 (marked as D), the particle was first expelled outwards to the wall by the spouting gas and then rose. The rising trajectory is located at about $x = 4.79$ cm. Note that this is in the x-direction. If the x-coordinate is converted into a radial distance r , then we must have $r/R_c \geq 0.75$. Larachi *et al.* (1996) observed an annular descending flow region for $r/R_c \geq 0.63$. The current results and visual observations during the present experiments confirmed that in the distributor region, particles near the wall were picked up by the gas jets and traveled upward for a certain distance. This is possibly

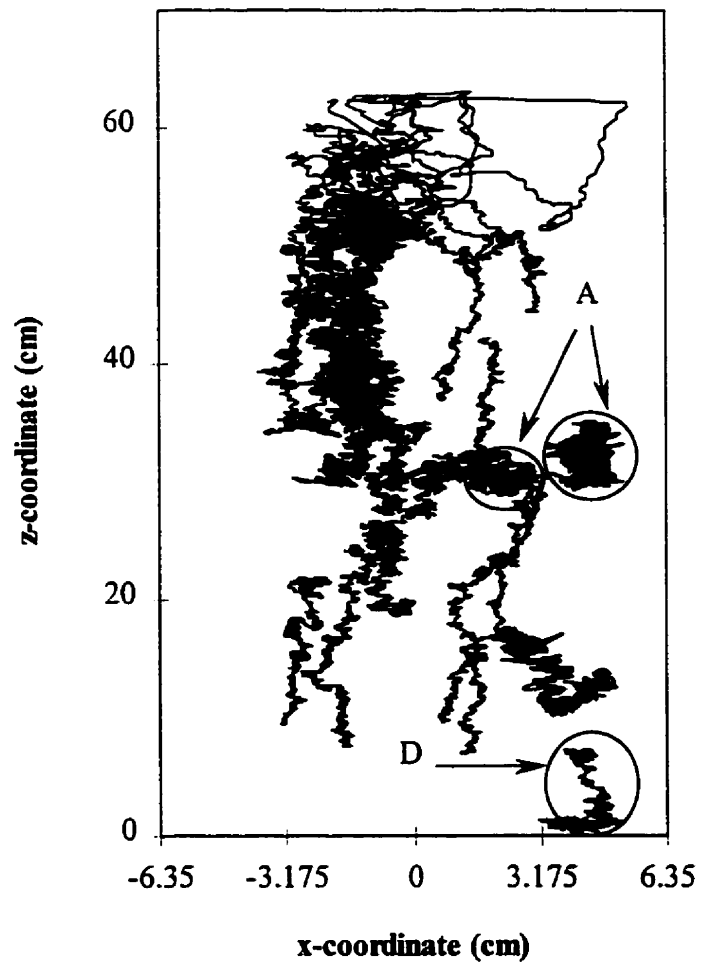


Figure 5.19 Schematic of x- and z- position of tagged particle in RPT experiments
($U_g = 1.46$ cm/s, $U_L = 1.68$ cm/s)

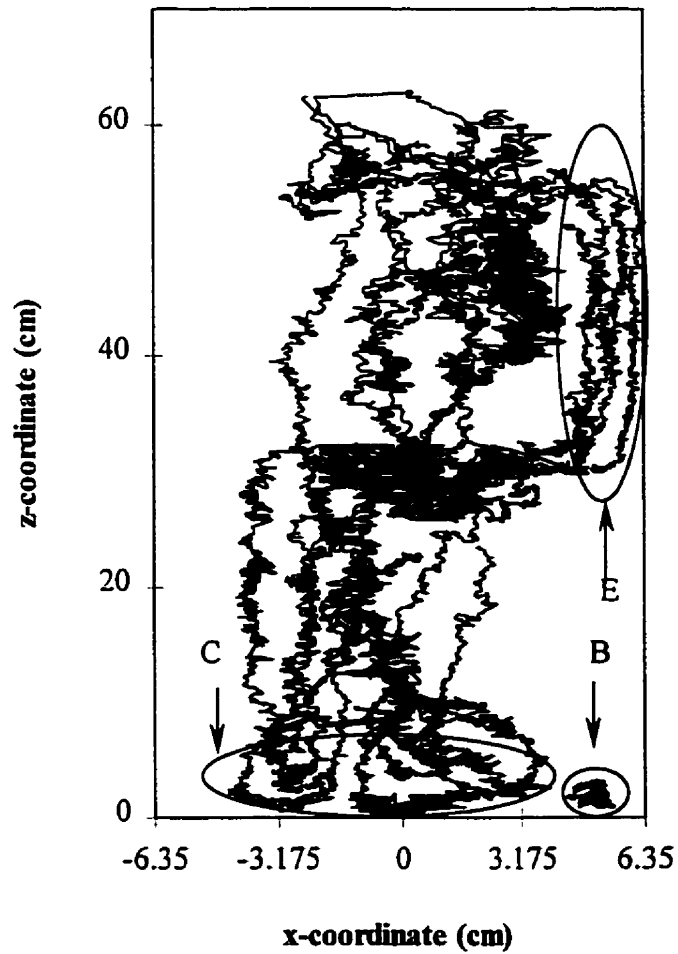


Figure 5.20 Schematic of x- and z- position of tagged particle in RPT experiments
($U_g = 1.46$ cm/s, $U_L = 2.08$ cm/s)

due to the effects of the distributor on the hydrodynamics of the fluidized bed containing low-density particles, as pointed out by Asif *et al.* (1991). Downward moving trajectories marked as E in Figure 5.20 are located at $r/R_c \geq 0.63$. The particles were ejected towards the wall by the bubbles in the free board region and descended for all the runs. Trajectories in area E are in good agreement with Larachi *et al.* (1996) and with visual observations during the current experiments.

The increasing mixing intensity is also evident from the x- and z-position frequency distributions shown in Figure 5.21. As we can see from Figure 5.21 (a), the particles appeared more often on right side of the column than the left side, indicating a strong effect of distributor on the flow pattern. With an increase in liquid velocity, the frequency distribution of particle occurrence flattened somewhat. In Figure 5.21 (b), there is a peak in z-position frequency distribution near the distributor for $U_L = 2.08$ cm/s because of the good particle circulating movements mentioned previously (area C of Figure 5.20). There is also a peak near 30 cm above the distributor for each liquid flow rate. Since the camera acquired images in two overlapping locations of the column, one might easily deduce that the higher occurrence was caused by the overlap. However, closer inspection of the trajectory profiles indicated that this is not the case. The reason was stagnant zones trapped the particles in them (area A of Figure 5.19).

5.3.1.2 Particle Tethering

Figure 5.22 shows the velocity distributions of free and tethered particles. Under current operating conditions, the x- and z-velocity distributions of both tethered and free particles appear similar. A goodness of fit analysis was used to determine whether the tethered particle velocities could be considered a sample population of the free particle velocities. The level of significance α was 0.05. Critical region $\chi_{\alpha, m-2}^2$ was obtained from Biometrika Tables for Statisticians (1966). The value of goodness of fit χ^2 , was calculated from the following equation (Freund and Walpole, 1980):

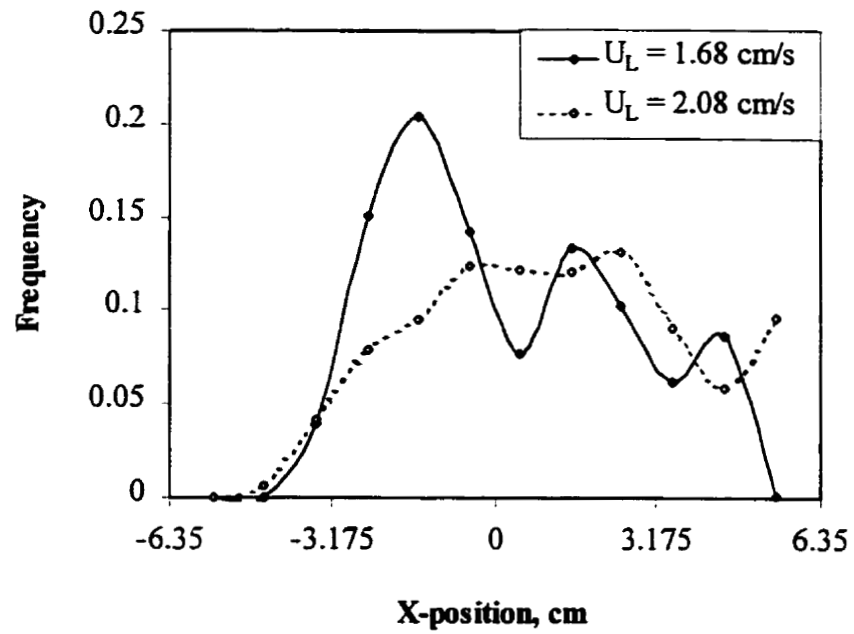


Figure 5.21 (a) Horizontal position profile ($U_g = 1.46$ cm/s)

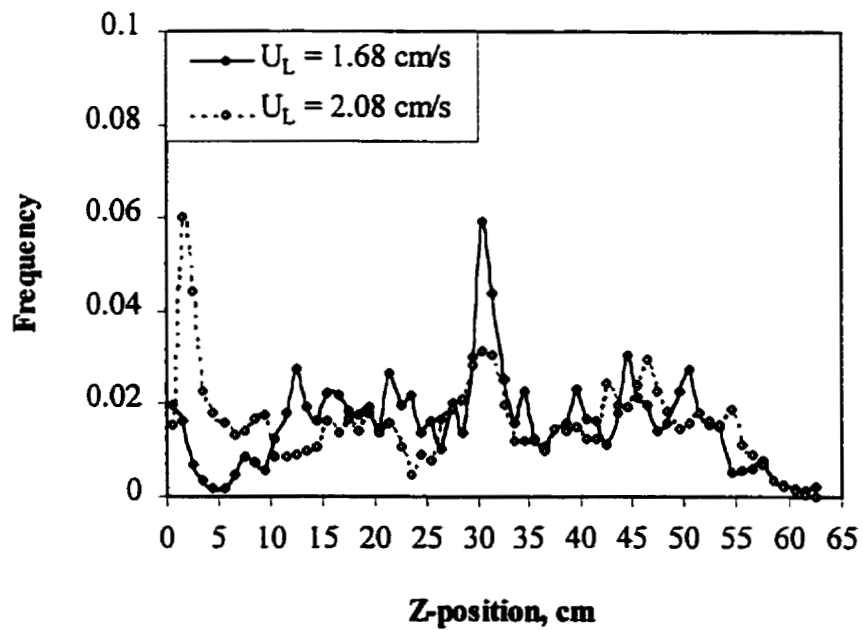


Figure 5.21 (b) Vertical position profile ($U_g = 1.46$ cm/s)

$$\chi^2 = \sum_{i=1}^m \frac{(f_i - e_i)^2}{e_i} \quad (5.1)$$

A sample calculation of χ^2 is illustrated in Table F.1. The results of the goodness of fit (Table 5.3, Song *et al.* 1999) confirm that tethered particles have a similar velocity distribution to free particles in the main bed region for both liquid velocities. While in the distributor region at $U_L = 1.68$ cm/s, the velocity distribution deviates significantly from that of free particle. Note that 1.68 cm/s is the minimum fluidization velocity for the corresponding liquid-solid system (U_{Lmf}), and 2.08 cm/s was the highest liquid velocity allowed with the existing pump system. For both liquid velocities and a gas velocity of 1.46 cm/s, the bed was not well mixed. Therefore, the discussions here are valid only under operating conditions close to U_{Lmf} .

Table 5.3 Goodness of fit for tethered to free velocity frequency distributions (PC, $U_g = 1.46$ cm/s)

Liquid Velocity, cm/s	Particle velocity	Critical region ($\chi_{0.05, m-2}^2$)	Goodness of fit (χ^2)	Result
1.68	x-main	36.415	5.03	Accept
	z-main	41.337	4.83	Accept
	x-distributor	27.587	172.05	Reject
	z-distributor	26.296	147.43	Reject
2.08	x-main	40.113	5.66	Accept
	z-main	38.885	3.69	Accept
	x-distributor	41.337	32.42	Accept
	z-distributor	37.652	35.85	Accept

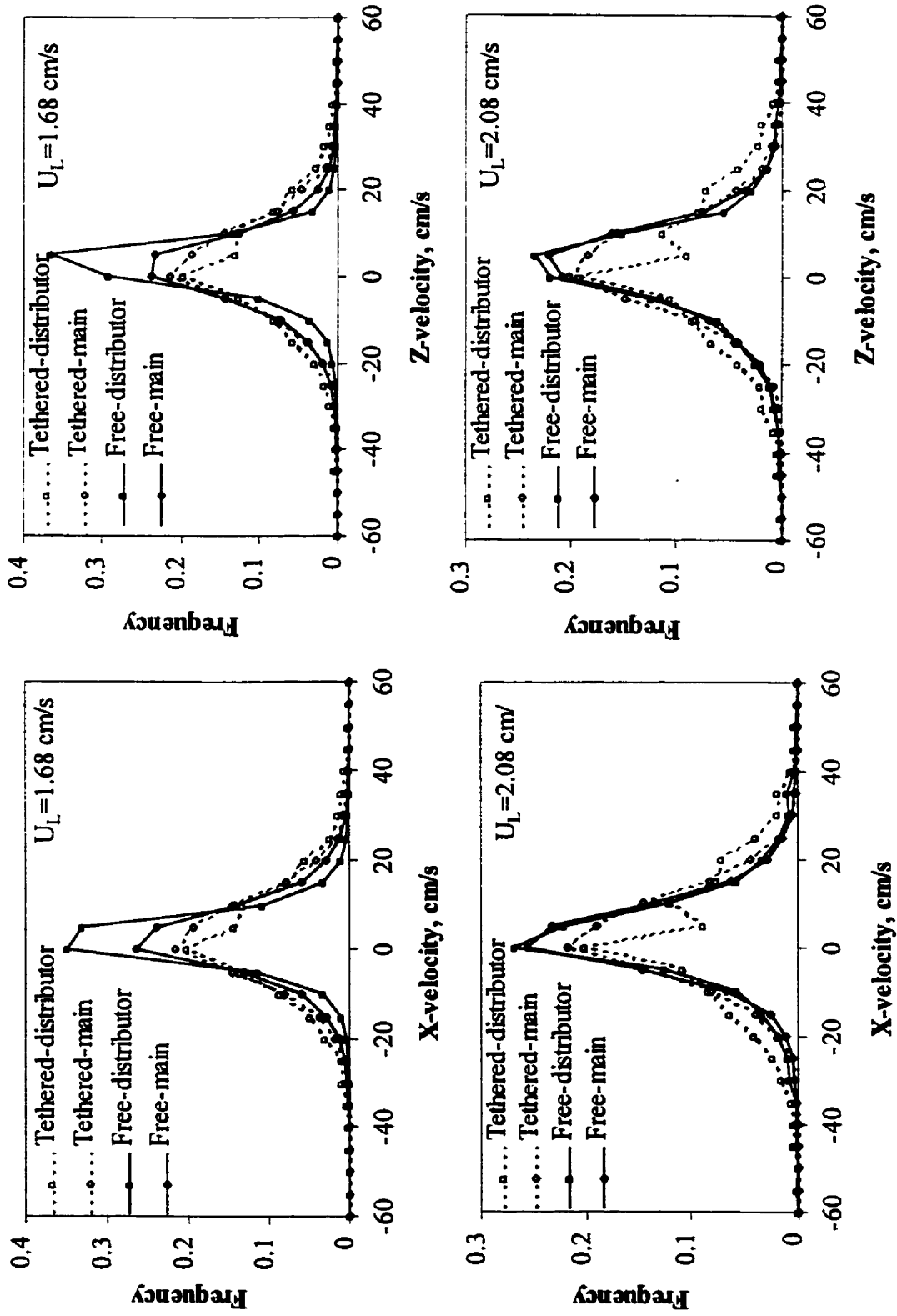


Figure 5.22 X- and Z- velocity distributions ($U_e = 1.46$ cm/s)

5.3.2 Particle Tracking of Polycarbonate Beads (Set 2)

The gamma camera face was centered at the third injection port ($z \cong 50.8$ cm). The superficial water velocity was increased to 2.69 cm/s to ensure excellent particle mixing. The superficial air velocity was 2.16 cm/s. To compare with free particle movements, two tether lengths were used: $\sqrt{2} R_c$ (9.0 cm) and $3 R_c$ (19 cm). The tethered particle was injected from the third port which is the same port as used for the injection of activated benzoic acid particles for mass transfer experiments. 40 sets of RPT data, each consisting of 1000 frames with a frequency of 20 Hz, were collected for free particle tracking. For tethered particle tracking, 20 sets of data were collected for each tether length with the same frequency as that of free particle. More sets of data were required for the free particle as it left the scanning area quite often.

5.3.2.1 Flow Pattern for the Vortical-Spiral Flow Regime

In the main bed section, the particles and liquid moving downward in straight and/or spiral manner near the column wall were observed. However, particles near the wall were also picked up by the gas jets to a certain distance in the distributor section. Those particles within the gas jets went up and down with the liquid stream as the gas channels occurred or disappeared periodically. Under the operating conditions of Set 2, few tiny bubbles existed in this region. This region was identical to the descending flow region as described by Chen *et al.* (1994, Figure 2.4) and Larachi *et al.* (1996).

The dynamic nature of the descending flow region was related closely to the formation and movement of vortices nearby. Adjacent to the descending flow region, spiral-downward and upward vortices which swung laterally back and forth to the wall could be seen. The ascending and descending vortices deformed after traveling a short distance and often yielded new vortices in the nearby downward stream. From emerging to disappearing, these vortices lasted only few seconds. The vortices trapped and discharged

gas bubbles as well as solid particles. This region, characterized by the spiral-downward and upward vortices, coincided with the vortical-spiral flow region observed by Chen *et al.* (1994) and Larachi *et al.* (1996).

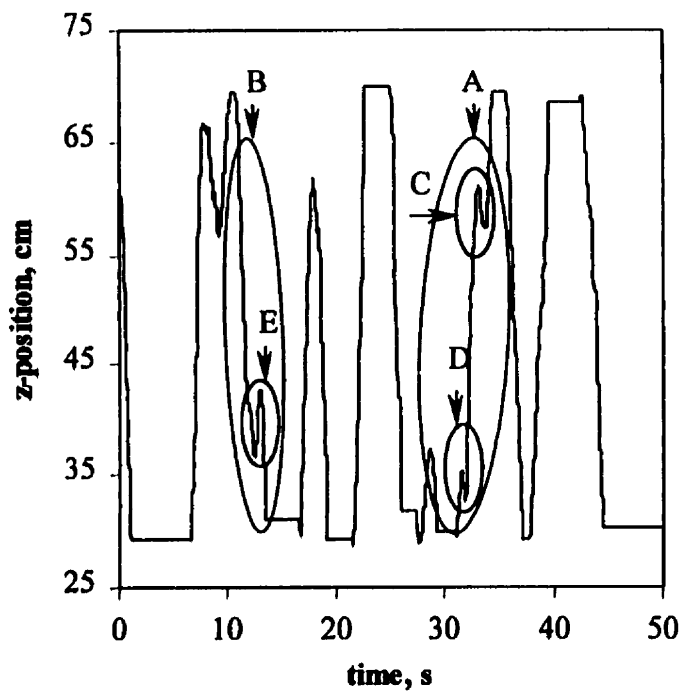
From the free-board section, clusters of bubbles were observed to move upward in a spiral manner with high velocity in the column center. There could be more than one spiral bubble stream existing simultaneously and the spiral direction changed dynamically. These spiral bubble streams swung laterally back and forth over almost the entire diameter. This region was referred to as the fast bubble flow region (Chen *et al.*, 1994; and Larachi *et al.*, 1996). Generally speaking, bubbles in this region were large (several centimeters), and they carried liquid and solid particles in their wake. The upward movements of gas bubbles, liquid and solid particles in the fast bubble flow region, and the compensating downward movements of liquid and solid particles in the descending flow region, resulted in a good macromixing in the axial direction. The vortices in the vortical-spiral flow region served as an "exchanger" for bubbles, liquid and solid between fast bubble flow region and descending flow region in the radial direction. The central plume region (shown in Figure 2.4), characterized by a relatively uniform bubble size distribution and surrounded by the fast bubble flow region, was not observed in this study. These observations concerning the vortical-spiral flow regime are in agreement with Chen *et al.* (1994), except with respect to the central plume, who used a 10.2 cm ID column and Larachi *et al.* (1996) who used a 10 cm ID column.

Figures 5.23 (a) and (b) show some typical movements of the free particle. As mentioned previously, the range of column being monitored was between 29 to 70 cm above the distributor. The horizontal flat lines in Figure 5.23 (a) simply represent the radioactive particle leaving the camera window.

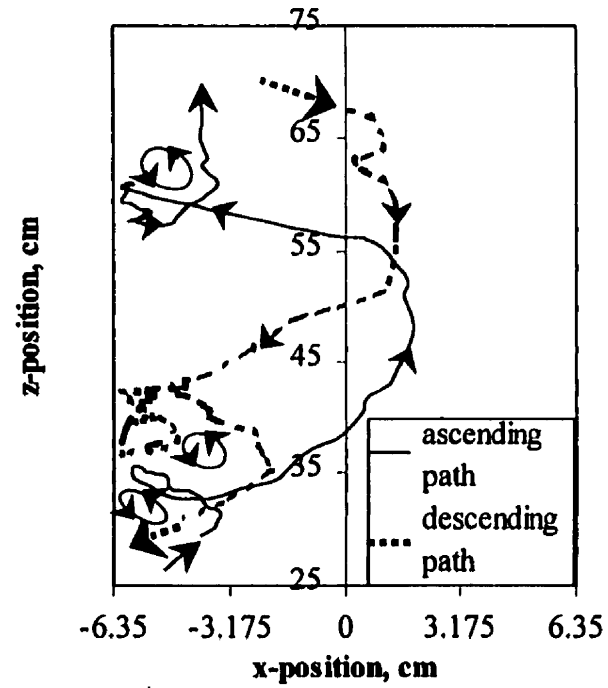
The free particle moved all the way up along the axial direction very often (Figure 5.23 (a)). The only possible explanation of this phenomenon was that the particle was carried up by a bubble wake. It is generally known that the pressure within the near wake is lower than that in the surrounding medium, thus the particles are trapped in the wake. This phenomenon indirectly confirmed the existence of a stable solids region in the near-wake region driven by the ascending bubble, as previously identified by Kitano and Fan (1988, Figure 2.1). Larachi *et al.* (1995, 1996) also observed that the bubble wake could pick up large and heavy particles such as 3 mm glass beads ($\rho_p = 2.5 - 2.6$). Dhanuka and Stepanek (1978) indicated that the solid holdup in the wake was virtually zero for glass particles larger than 2 mm in a water system; while non-zero values could be obtained for particles smaller than 1 mm with a specific gravity of less than 3 with water as the liquid phase. Kitano and Fan (1988) showed that bubble wakes could carry up solids of less than 1 mm in size. This is the first time a bubble wake has been observed to carry a particle size as large as 6.35 mm ($\rho_p = 1.16$). The bubble velocity can also be indirectly obtained from the particle rising velocity, since the bubble wake moves at the same velocity as the bubble (Larachi *et al.*, 1995).

Besides the large-amplitude ascending movement, the free particle also exhibited an ascending-descending-ascending random path (area A in Figure 5.23 (a)). This type of movement is explained as follows: the particle first ascended with the bubble wake, was shed from the wake and drifted with the liquid-solid emulsion, then it was picked up by another bubble wake and a new ascent was initiated. This indicated that particle exchange occurred with the liquid-solid emulsion phase due to wake shedding. The bubble wakes thus contribute to the solid mixing in the column.

Figure 5.23 (b) shows the x-z trajectory of the free radioactive particle in areas A and B of Figure 5.23 (a). A spiral pattern for both the ascending and descending paths can be



(a)



(b)

Figure 5.23 Typical movements of the free-particle (PC, $U_g = 2.16$ cm/s): (a) z-position vs. time (b) ascending and descending path in area A and B respectively (dotted circles indicate a vortex)

observed. The ascending spiral path swung laterally back and forth over almost the entire column diameter, indicating that the particle was in the fast-bubble flow region (see Figure 2.4). Examining Figure 5.23 (b) closely, one can see that whenever the particle approached the wall, it became trapped in a counter-clockwise vortex on the left side (dotted circles). This directly confirmed the existence of a vortical-spiral flow region between the fast-bubble flow region and the wall. It was within these vortices that the particle was shed from the large bubble wake and exhibited the random longitudinal fluctuation movement shown in sub-areas C, D and E of Figure 5.23 (a).

A particle large-amplitude downward movement was also exhibited for descending paths in Figure 5.23 (a). The downward solid motion, located near the wall, arose as a response to counterbalance the solid upflow induced by rising bubbles in the fast-bubble region. Note that the particle descending trajectories were not necessarily straight. Indeed, visual observations indicated that most of them descended spirally. The existence of such a region, characterized by the downward liquid and solid movements and referred to as the descending flow region, was thus shown.

Three types of particle movements have been discussed so far: the bubble-like or wake movement in a spiral manner in the fast bubble flow region (located in the column center), the compensatory descending movement in either straight or spiral manner in the descending flow region (located near the wall), and the random longitudinal fluctuating movement with the vortex in the vortical-spiral flow region (located between the wall and the fast bubble flow region). The two former types of movement were characterized by large amplitude axial displacements of solid particles and the latter was characterized by local short-distance radial interactions between solid, liquid and small bubbles. Together all movements resulted in a high level of bed-scale mixing of the solid particles.

5.3.2.2 Free Versus Tethered Particle Movements

Figure 5.24 compares typical movements of free and 9 cm tethered particles. For a tether length of 9 cm, the particle trajectory was confined within 50.8 ± 9 cm in z-direction (marked by horizontal dash line). Compared to the movements of a free particle, it spent more time fluctuating at the upper and lower boundaries, such as areas A and B in Figure 5.24. In the z-direction, the amplitude of the fluctuating movements was very small, but the frequency was quite high. The tethered particle was first trapped in the bubble wake and ascended (end of area A) with the bubble in the fast-bubble flow region. Because of the restriction of the tethering, the particle could not go above 59.8 cm (beginning of area B) in the z-direction. Thus it was shed from the wake, drifted with the liquid-solid emulsion (area B). Due to the nature of the fast-bubble flow region, i.e. swinging laterally back and forth over the diameter, eventually the particle encountered the descending flow region and started to descend with liquid-solid emulsion near the wall (end of area B). Again, because of the restriction of the tethering, the particle could not go below 41.8 cm in the z-direction. The particle drifted with the liquid-solid emulsion in the descending flow region until it encountered the fast-bubble flow region, was entrained in a bubble wake and started another ascending trajectory. Thus, a circulation process is observed in Figure 5.24. Note that during its ascending or descending paths, the particle might encounter a vortex generated in the vortical-spiral flow region and change its direction as shown in areas C and D.

Figure 5.25 shows the comparison of typical movements of free, 9 cm and 19cm tethered particles. For 19 cm tethering, the particle was seen going all the way up (also went out of the camera window sometimes but it came back very soon) and down quite often similar to the free particle. Its movements appeared closer to that of free particle than 9 cm tethering even though it still occasionally fluctuated near the boundaries (areas C and D of Figure 5.25). The average particle ascending and descending velocities in area B can be determined by using the best linear fits of z-position versus time curves (Larachi *et al.*,

1996) shown in Appendix G.1. For the free particle, ascending and descending velocities were 46 and 28 cm/s respectively; for 19 cm tethering, they were 30 and 19 cm/s; while for 9 cm tethering, they were 18 and 9 cm/s. Ascending velocities are always higher than that of descending ones. This concurs with the ascending particle being located in the fast-bubble flow region where higher velocities are observed. Furthermore, tethering lowered the particle velocity for either ascending or descending movements. With the increased tether length, the effect on particle ascending and descending velocities was reduced.

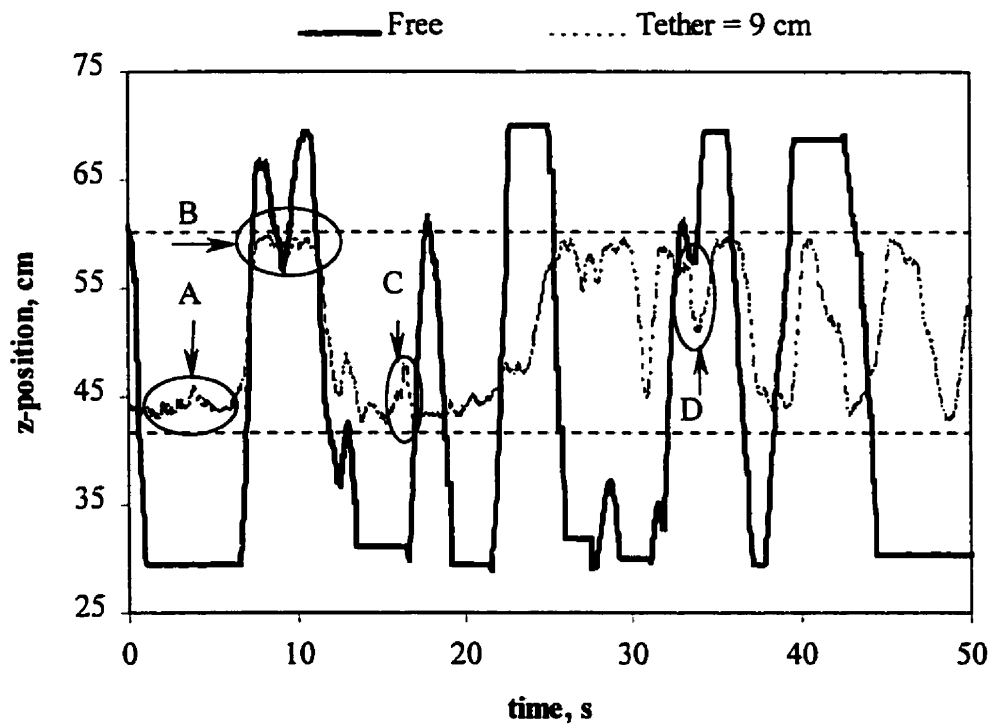
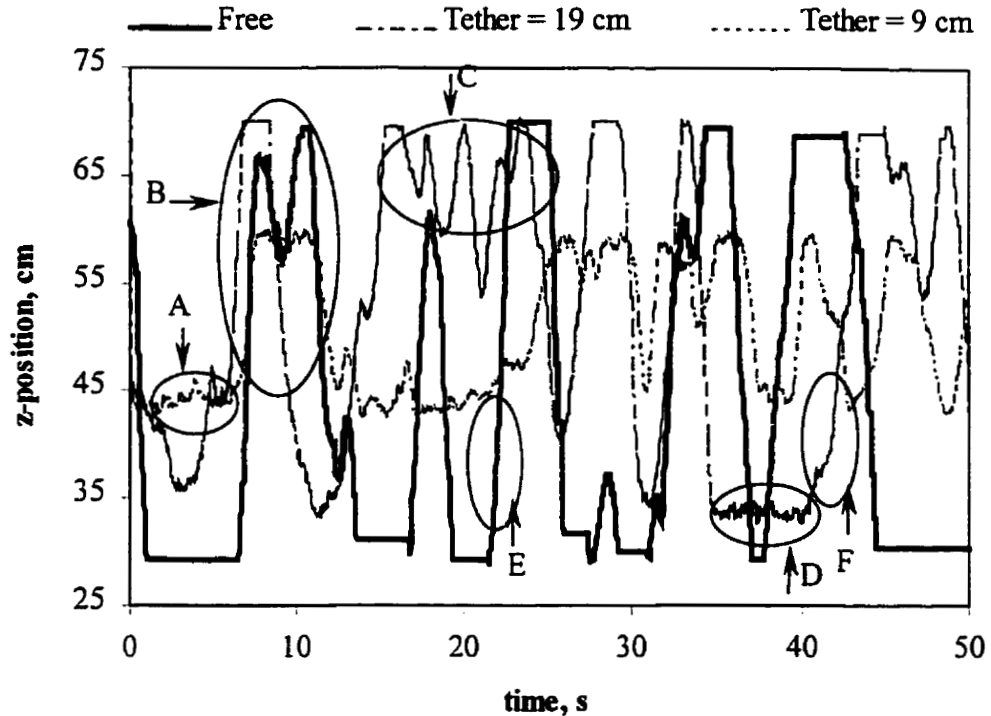


Figure 5.24 Comparison of typical movements of free and 9 cm tethered particles
(PC, $U_g = 2.16$ cm/s)



**Figure 5.25 Comparison of typical movements of free and tethered particles
(PC, $U_g = 2.16$ cm/s)**

The z-velocity of the tethered particle was even lower while it was fluctuating. As can be seen from Figure 5.26, the magnitude of fluctuating velocities corresponding to area A and D in Figure 5.25 was within approximately ± 20 cm/s. On the other hand, z-velocity ranged from -20 to +60 cm/s for the free particle. The 19 cm tethered particle had velocities comparable in magnitude to the free particle movements (areas E and F, Figures 5.25 and 5.26).

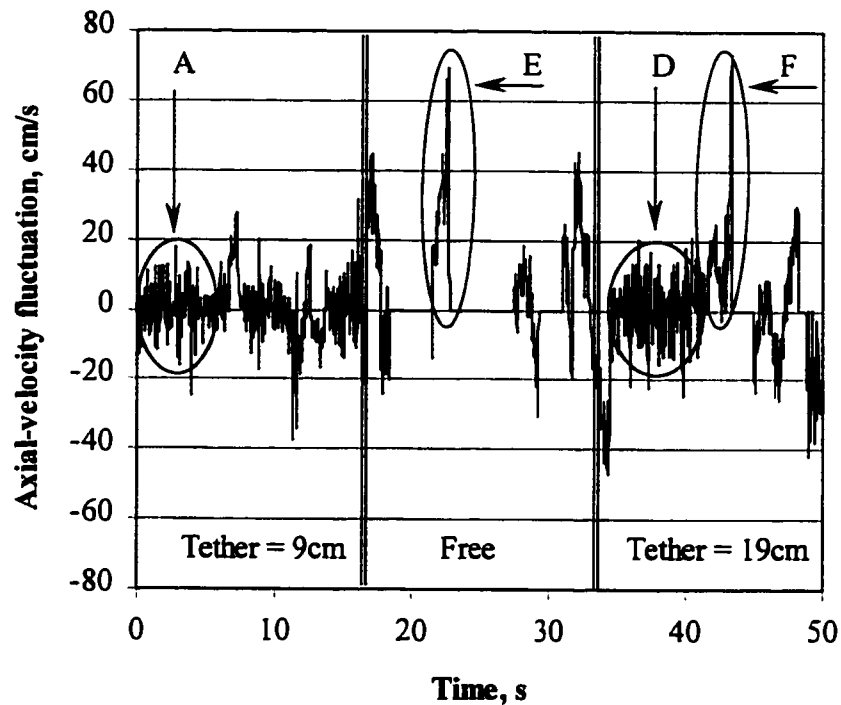


Figure 5.26 Particle velocity fluctuations (PC, $U_g = 2.16$ cm/s)

Figures 5.27 (a) and (b) show particle occurrence frequency in the column for different cases (see also Appendix E, Figures E.1, E.2 and E.3). The position frequency distributions for the free particle are quite even in both x- and z-direction. The particle visited everywhere within the window (from 29 to 70 cm in z-direction and from -6.35 to 6.35 cm in x-direction), indicating that good mixing was achieved. For a tethered length of 9 cm ($\sqrt{2} R_c$), the particle movement was confined within 50.8 ± 9 cm (41.8 to 59.8 cm) in z-direction. Compared to free particle, the differences of z-position frequency distribution are substantial. There is a peak near 44 cm. Since the particle downward movement occurred near the column wall, this location was its lower boundary where

particle would fluctuate for some time before it turned around. Near 59 cm, there is a very high peak which marks the upper boundary of particle movements. In x-direction, there exists a broad peak value of position frequency distribution between -2.5 to 3.5 cm for the 9 cm tethered particle (Figure 5.27 (b)). In x-direction, 19 cm (3R) tethering also has a peak value between -1.5 to 3.5 cm, indicating tethered particles tend to spend more time in the central region. The z-position frequency distribution for 19 cm tethering is similar to that of free particle. However, at the lower portion, the particle seems to have higher occurrence near 35, 38, 42 and 51 cm. 35 cm would be the lower boundary for 19 cm tethering. Our visual observation confirmed that the other higher occurrences were caused by the tether being wound to the injection tube. The general trend here is: with increasing tethered length, the particle position distribution along the axial and radial directions becomes similar to free particle movements.

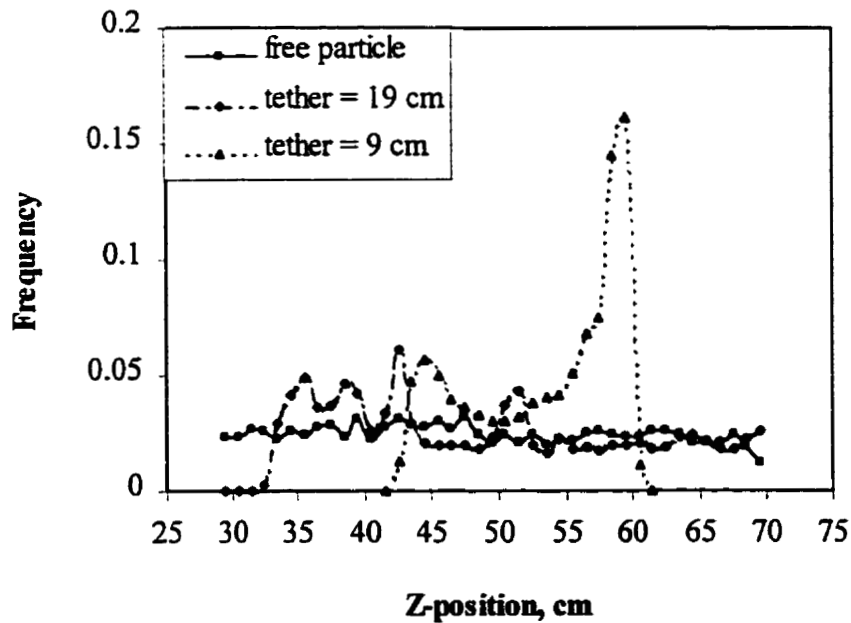


Figure 5.27 (a) Particle Z-position distribution (PC, $U_g = 2.16$ cm/s)

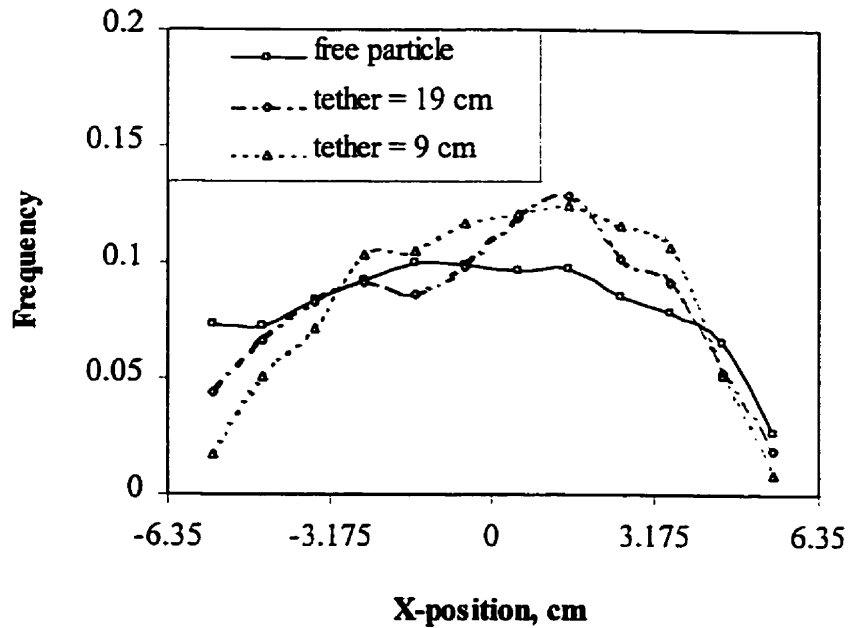


Figure 5.27 (b) Particle X-position distribution (PC, $U_g = 2.16$ cm/s)

Figures 5.28 (a) and (b) show the z and x-velocity distributions for the free particle, 19 cm tethering and 9 cm tethering. The z-velocity distributions are wider than x-velocity distribution. The z-velocity distribution of the free particle is also wider than those of tethered ones; 19 cm tethering is wider than that of 9 cm tethering. The observations coincide with previously discussion: tethering lowers the particle velocity and the shorter the tethering, the more significant the effect. The x-velocity distributions are very similar for the three cases. A goodness of fit analysis was again used to determine whether the tethered particle velocities could be considered a sample population of the free particle velocity. The goodness of fit analysis (Table 5.4) shows that z-velocity of 9 cm tethering deviates from that of free particle; while z-velocity of 19 cm tethering and x-velocities of both lengths of tethering have similar distributions to those of free particle.

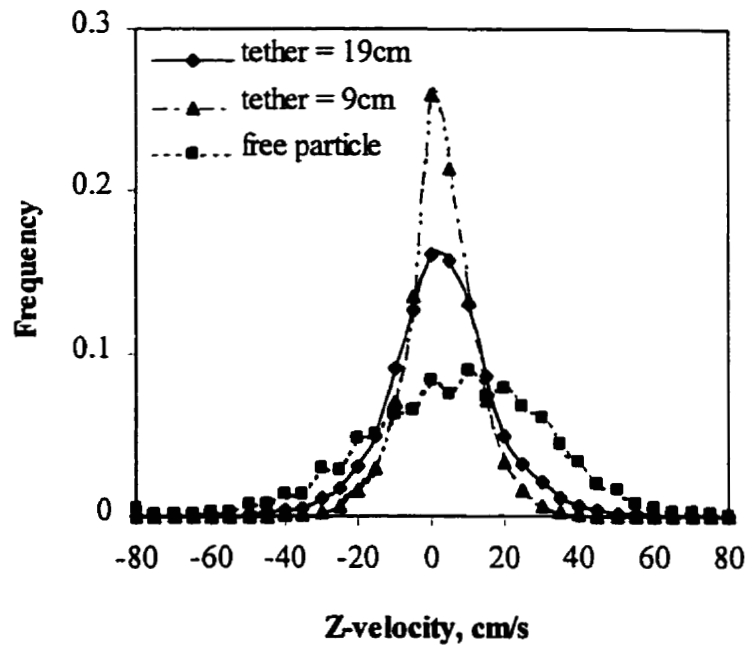


Figure 5.28(a) Particle Z-velocity distributions (PC, $U_g = 2.16$ cm/s)

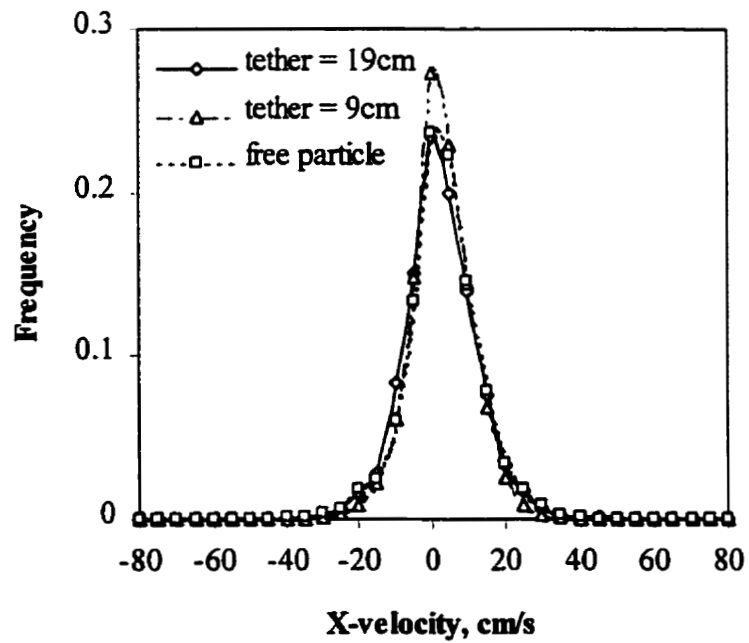


Figure 5.28(b) Particle X-velocity distributions (PC, $U_g = 2.16$ cm/s)

**Table 5.4 Goodness of fit for tethered to free velocity frequency distributions
(PC, $U_g = 2.16$ cm/s, $U_L = 2.69$ cm/s)**

Tether length (cm)	Velocity	Critical region ($\chi_{0.05, m-2}^2$)	Goodness of fit (χ^2)	Result
9 ($\sqrt{2} R_c$)	z-velocity	43.773	84.428	Reject
	x-velocity	30.144	2.177	Accept
19 (3 R_c)	z-velocity	43.773	29.122	Accept
	x-velocity	30.144	5.953	Accept

5.3.3 Particle Tracking of Polypropylene Cylindrical Beads (Set 3)

The gamma camera face was centered at the third injection port ($z \cong 50.8$ cm), where mass transfer experiments were performed. As indicated in Table 5.2, one superficial water velocity, and two superficial air velocities were used. The solid particles used were polypropylene cylindrical beads with an equivalent diameter of 4.221 mm (Table 4.1). The experiments were conducted in the vortical-spiral flow regime for $U_g = 2.0$ cm/s and in the dispersed flow regime for $U_g = 0.82$ cm/s. To compare with free particle movements, two tether lengths were used: $\sqrt{2} R_c$ (9.0 cm) and 3 R_c (19 cm). The tethered particle was injected in the same way as mentioned for polycarbonate bead. 40 sets of data, each consisted of 1000 frames with a frequency of 20 Hz, were collected for free particle tracking. For tethered particle tracking, 20 sets of data were collected for each tether length with the same frequency as that of free particle.

5.3.3.1 Flow Patterns

At $U_g = 2.0$ cm/s, the column operated in the vortical-spiral flow regime. Some particles were observed to reach the screen on the column top. In the main bed section, the particles and liquid moved downward in straight and/or spiral manner near the column

wall at one side. At the other side, solid particles and liquid moved up all the way to the free-board also in straight and/or spiral manner. It should be noted that for all experiments the column was checked and maintained in a vertical position. Morooka *et al.* (1982) also observed that the value of liquid velocity near the wall was not necessarily negative. However, this phenomenon was not found in the studies of Chen *et al.* (1994) and Larachi *et al.* (1996). Note that the solid particles they used were glass beads with a density of 2500 kg/m^3 . The reason for particles moving up at one side and down the other could be the effects of the distributor on hydrodynamics of the fluidized bed containing low-density particles (Asif *et al.*, 1991). At $U_g = 2.0 \text{ cm/s}$, few tiny bubbles existed in the region located near the column wall. It was characterized by the downward and upward movements of liquid and solid streams, and is referred to as liquid-solid emulsion region in this study.

Adjacent to liquid-solid emulsion region, spiral-downward and upward vortices which swung laterally back and forth to the wall were observed. These vortices were observed over the full height of the bed. They trapped and discharged particles and tiny gas bubbles. This region, characterized by the spiral-downward and upward vortices, was again referred to as vortical-spiral flow region observed by Chen *et al.* (1994) and Larachi *et al.* (1996).

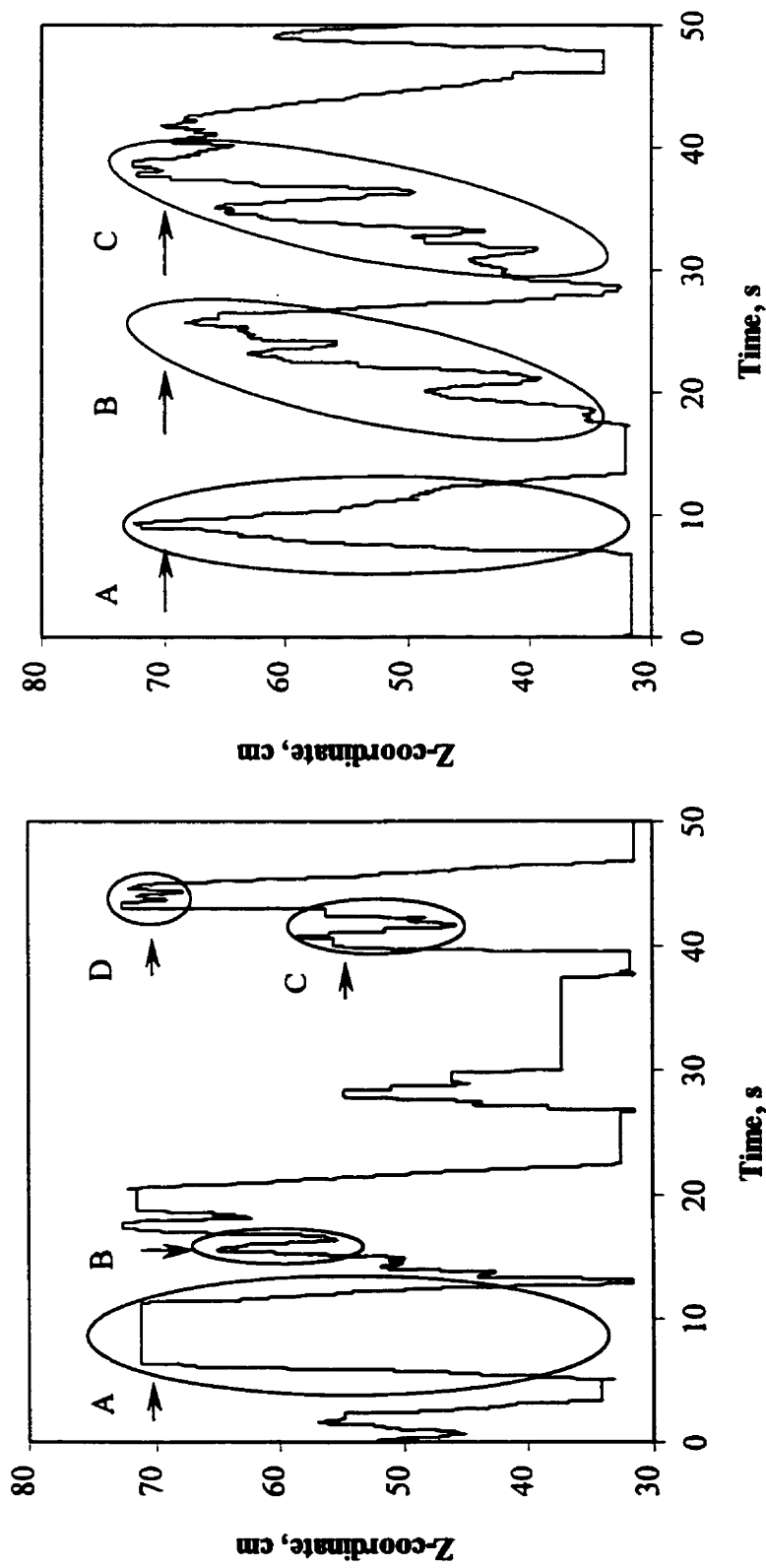
In the free-board section, clusters of bubbles were observed to move upward in a spiral manner with high velocity in the column center. At times, there was more than one spiral bubble stream existing simultaneously and the spiral direction changed dynamically. These spiral bubble streams swung laterally back and forth over almost the entire diameter. This region is referred to as the fast bubble flow region (Chen *et al.*, 1994; and Larachi *et al.*, 1996)

When the column operated in the vortical-spiral flow regime, it could be divided into three regions: the fast-bubble flow region in the column center, which was characterized

by the upward spiral bubble streams or bubbles; the vortical-spiral flow region, which was adjacent to the fast-bubble flow region and was characterized by the downward and upward vortices; and the liquid-solid emulsion region near the wall, which was characterized by the downward and upward movements of liquid and solid streams.

For $U_g = 0.82$ cm/s, the column operated in the dispersed flow region, and the bubble size was relatively uniform. Some bubbles did however grow to a large size (2-3 cm in diameter) and rose spirally in a narrow radial range of the column center and a few vortices were observed.

Figure 5.29 (a) and (b) show the typical movements of a free particle for $U_g = 2.0$ cm/s and $U_g = 0.82$ cm/s. Three types of movements are exhibited here: the wake movement in the fast bubble flow region (ascending path in area A), the compensatory descending movement (descending path in area A), and the random fluctuation movement (areas B, C and D). Moreover, the lower the gas velocity, the more frequent the random fluctuating movements. As we discussed previously, the random fluctuating movements were caused by the particle being shed from the bubble wake. With increasing gas velocity, the wake of large leading bubble become more stable because of the existence of the bubbles trailing behind which prevents the particles in the leading bubble wake from being shed. Note that the operating conditions here were $U_L / U_{Lmf} = 1.8$ with $U_g = 2.0$ cm/s and $U_g = 0.82$ cm/s, and the operating conditions for polycarbonate beads were $U_L / U_{Lmf} = 1.6$ with $U_g = 2.16$ cm/s. If we compared Figure 5.29 (a) to Figure 5.23 (a), we could see that the particle no longer went all the way up without being shed from a wake. The major differences here were particle size and shape (see Table 4.1). Larachi *et al.* (1995) also found that the smaller the particles were, the shorter time they resided in the wake. In order to find out whether size or shape is more critical to the stabilization of the wake



(a)

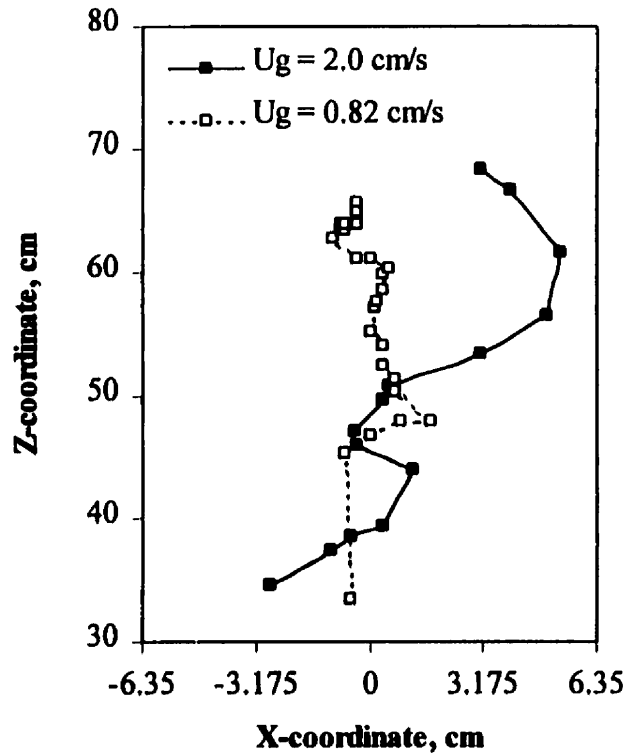
(b)

Figure 5.29 Typical movements of the free-particle
 (a) $U_g = 2.0 \text{ cm/s}$ (b) $U_g = 0.82 \text{ cm/s}$

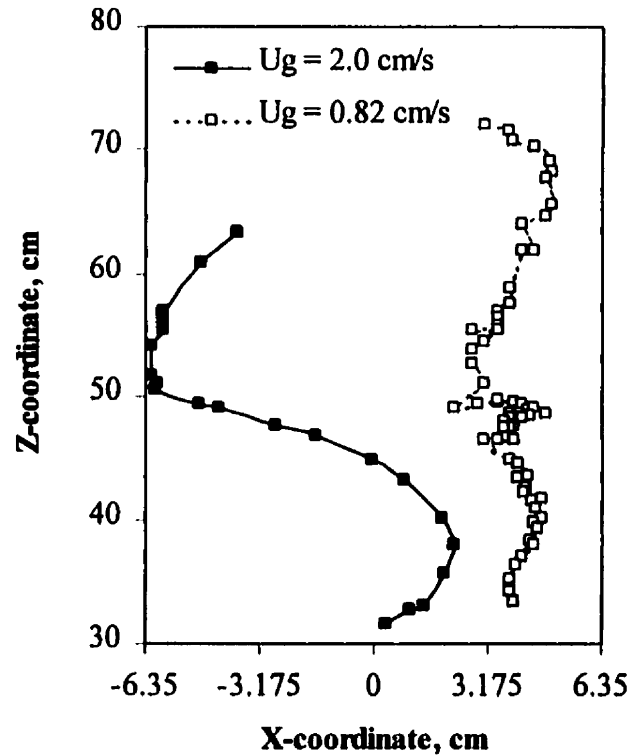
(the longer the residence time, the more stable the bubble wake), more research will be necessary.

The ascending and descending paths for $U_g = 2.0$ cm/s and 0.82 cm/s of area A of Figures 5.29 (a) and (b) are shown in Figures 5.30 (a) and (b). A relatively narrow zigzag ascending or descending trajectory in the axial direction was observed for $U_g = 0.82$ cm/s. Recall that for $U_g = 0.82$ cm/s, the column was operated in dispersed flow regime. In this regime, most bubbles are small and rise steadily in relatively rectilinear paths, while only some large bubbles rise spirally in the column center within a narrow range. Occasionally, when a large bubble passes by, it traps the particle in its wake and carries the particle up while it is ascending. However, the bubble wake in the dispersed flow regime is not very stable. As a large bubble accelerates and the wake grows in size by continuously accumulating material from outside the wake, the symmetry of its flow is perturbed and eventually some wake material is discharged, i.e. shed (Tsuchiya and Fan, 1988). The periodic nature of asymmetric wake shedding causes the zigzag motions of particles as shown in the ascending path of Figure 5.30 (a). Once a particle is shed from the wake, it may start to descend near the wall until it is trapped in the wake of another upcoming bubble and starts a new ascending path (areas B and C in Figure 5.29). By contrast, the trajectories of particles in the vortical-spiral flow regime ($U_g = 2.0$ cm/s) exhibit a wide spiral pattern: the ascending and descending paths covers almost the whole diameter (Figure 5.30). From a chemical reactor point of view, this type of movement is desired simply because it increases radial mixing.

The ascending and descending velocities for $U_g = 2.0$ cm/s were 30 and 23 cm/s respectively (Figure G.2). While for $U_g = 0.82$ cm/s, they were 17 and 7.7 cm/s. Again, the ascending velocities were found to be higher than descending velocities. Furthermore, the ascending and descending velocities for $U_g = 2.0$ cm/s were higher than those of $U_g = 0.82$ cm/s.



(a)



(b)

Figure 5.30 Particle ascending and descending paths from area A of Figure 5.29
(a) Ascending (b) Descending

5.3.3.2 Free Versus Tethered Particle Movements

Figure 5.31 shows the comparison of typical movements of free, 9 cm and 19cm tethered particles. They all exhibit random fluctuation movements in their paths, especially near the upper boundaries for 9 and 19 cm tethering. The shorter the tether, the more frequent the random fluctuating movements. Note that the particle did not exit the camera window for 19 cm tethering.

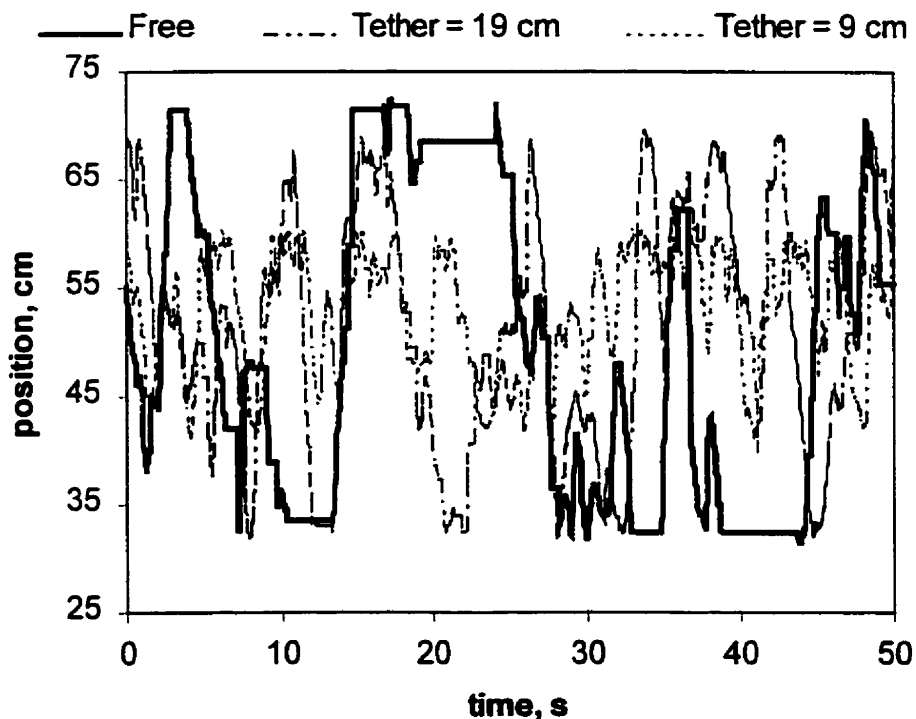


Figure 5.31 Comparison of typical movements of free and tethered particles
(PP, $U_L = 2.20$ cm/s, $U_g = 2.0$ cm/s)

Figures 5.32 (a) and (b) show particle occurrence frequency in the column for $U_g = 2.0$ cm/s (see also Appendix E, Figures E.4, E.5 and E.6). The position frequency distributions for free particle are quite even in both x- and z-directions. A similar

phenomenon of particle occurrence is observed for the tethered particles: it gradually increases along z-direction until reaches its upper boundary (59 cm for 9 cm tethering, and 68 cm for 19 cm tethering), where the occurrence has a sudden peak. Moreover, the shorter the tethering, the larger the peak. Compared to the occurrence of polycarbonate particle (Figure 5.27 (a)), a relatively high occurrence at the lower boundary no longer exists. This was because no wrapping of the tether on the injection tube occurred. In x-direction, the position frequency distributions for free particle and 19 cm tethering are similar. Again, with increasing tethered length, the particle position distribution along x- and z-directions is improved. The similar trends are also observed for $U_g = 0.82$ cm/s as shown in Figure 5.33 (a) and (b) (see also Appendix E, Figures E.7, E.8 and E.9).

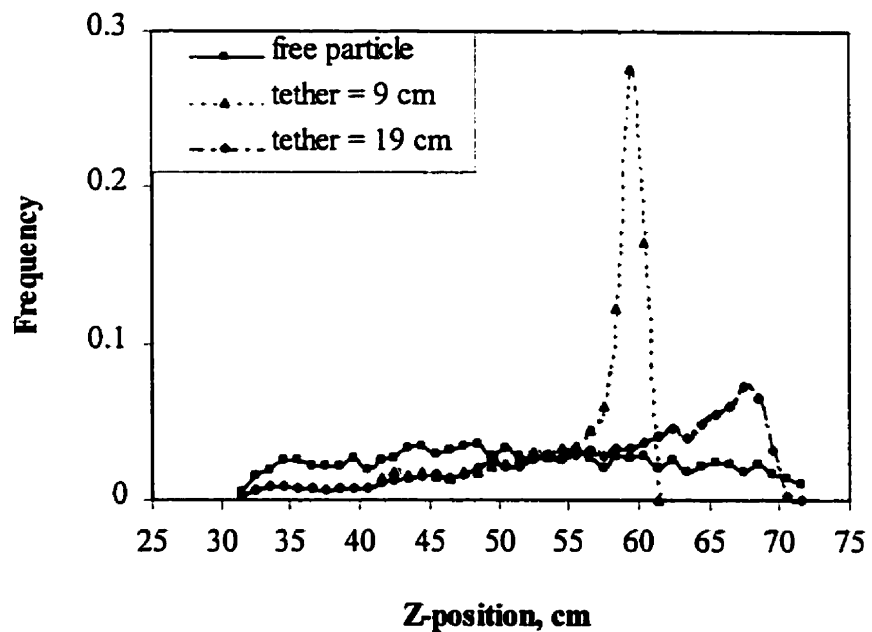


Figure 5.32 (a) Particle Z-position distribution ($U_g = 2.0$ cm/s)

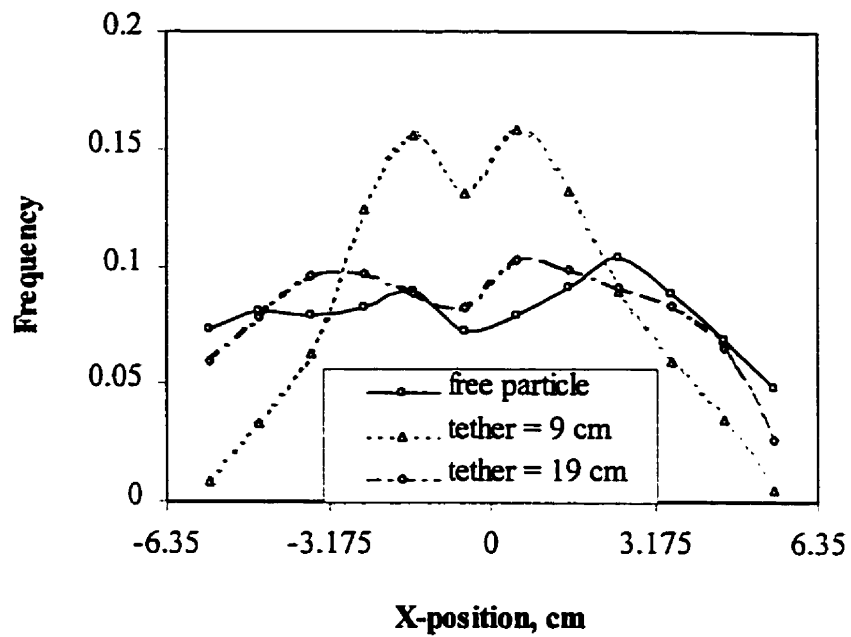


Figure 5.32 (b) Particle X-position distribution ($U_g = 2.0$ cm/s)

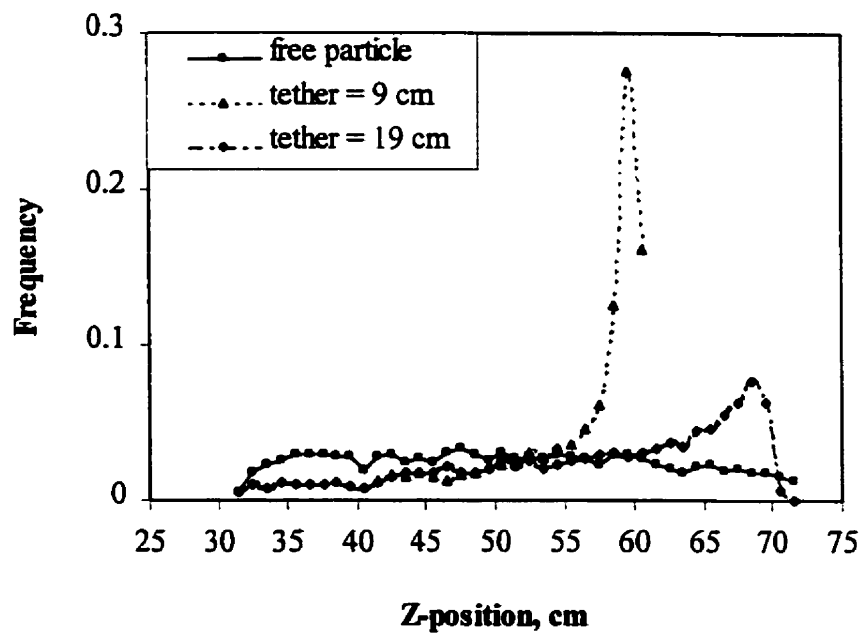


Figure 5.33 (a) Particle Z-position distribution ($U_g = 0.82$ cm/s)

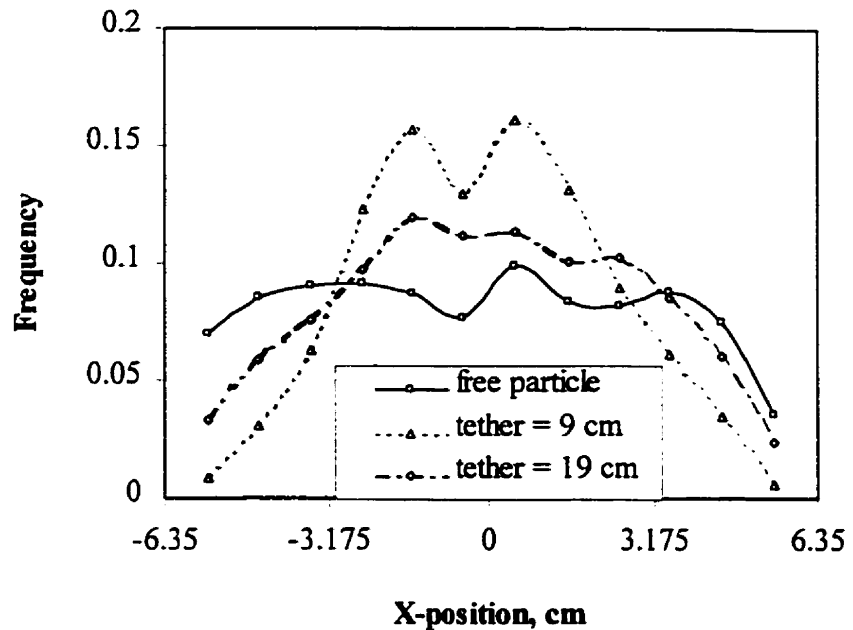


Figure 5.33 (b) Particle X-position distribution ($U_g = 0.82$ cm/s)

The velocity distributions of polypropylene particles are similar to those of polycarbonate particles (Figure 5.34). A goodness of fit analysis was also conducted to compare the velocity distributions of tethered particles to that of the free particle (Table 5.5). The goodness of fit analysis shows that at the higher gas velocity in the vortical-spiral flow regime, z-velocity of 9 cm tethering deviates significantly from that of free particle; while z-velocity of 19 cm tethering and x-velocities for both gas velocities have similar distributions to those of the free particle.

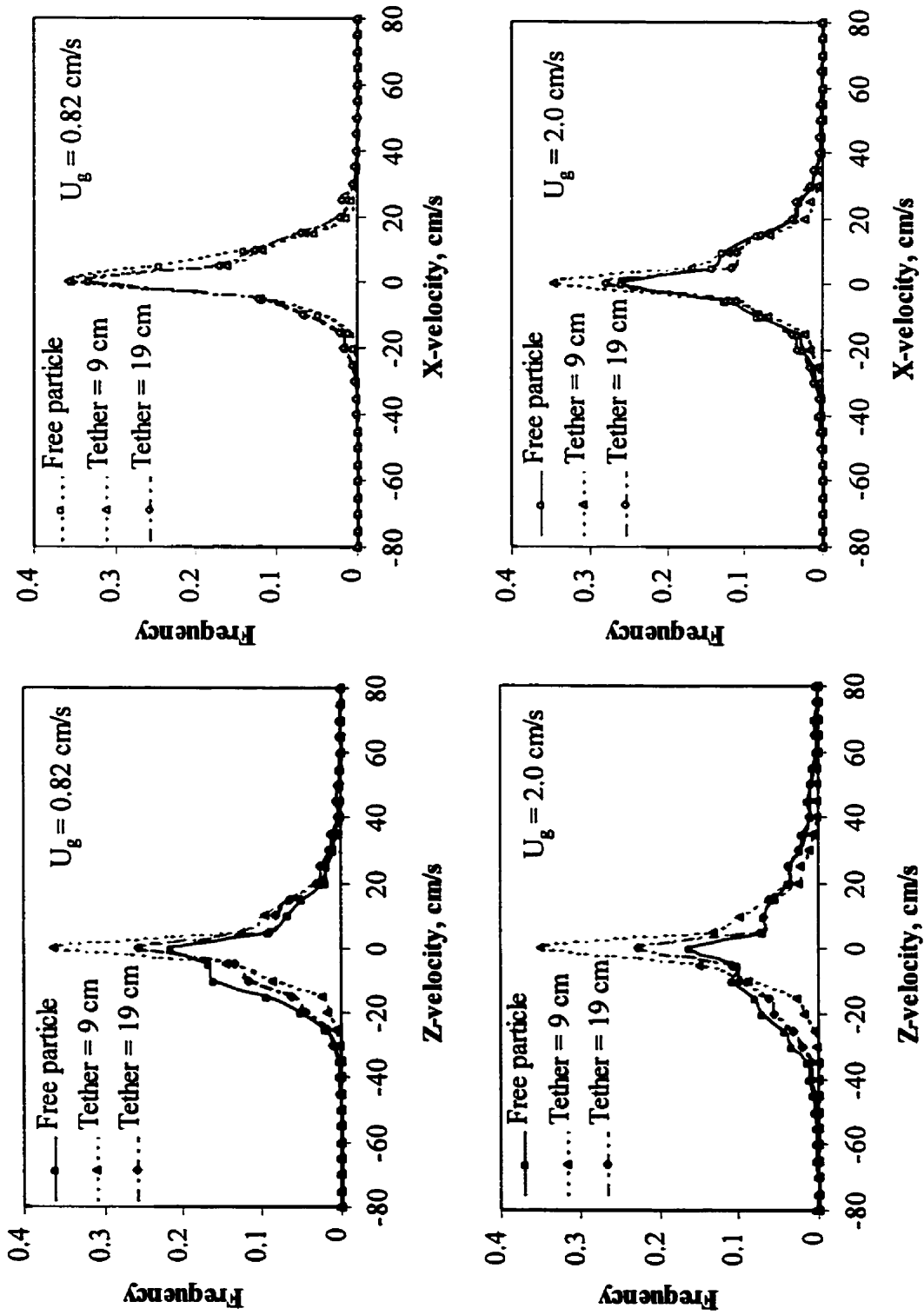


Figure 5.34 X- and Z-velocity distributions (PP, $U_L = 0.82$ cm/s)

**Table 5.5 Goodness of fit for tethered to free velocity frequency distributions
(PP, $U_L = 2.20$ cm/s)**

Tether length (cm)	U_g (cm/s)	Velocity	Critical region ($\chi^2_{0.05, m-2}$)	Goodness of fit (χ^2)	Result
9 ($\sqrt{2} R_c$)	0.82	z-velocity	41.337	25.820	Accept
		x-velocity	32.671	23.937	Accept
	2.0	z-velocity	43.773	55.848	Reject
		x-velocity	42.557	7.218	Accept
19 (3 R_c)	0.82	z-velocity	41.337	8.329	Accept
		x-velocity	32.671	20.895	Accept
	2.0	z-velocity	43.773	5.118	Accept
		x-velocity	42.557	3.971	Accept

In summary, when the column operates in the dispersed flow regime, particle tethering shows no effect at $\sqrt{2} R_c$ nor $3 R_c$ on particle velocity distributions (Table 5.5). When the column operates in the vortical-spiral flow regime, z-velocity distributions of 9 cm ($\sqrt{2} R_c$) tether show a significant deviation to that of free particle (Tables 5.4 and Table 5.5). If the tether length is increased to 19 cm (3R), tethering effect is sufficiently reduced.

For the vortical-spiral flow regime, the three regions observed in the column, namely the fast-bubble flow region in the center, the gas-liquid-solid emulsion region near the wall and the vortical-spiral flow region in between, have strong effects on solid-liquid mass transfer. If a particle is in the fast-bubble flow region or vortical-spiral flow region, it will encounter the increased turbulence generated by the fast rising bubble wakes or the vortices. Due to the restriction of the tether, tethered particle has a higher occurrence near column center ($x = 0$) than free particle (Figures 5.27 (b) and 5.32 (b)). Therefore,

a higher mass transfer coefficient is expected because of the high turbulence. Moreover, a tethered particle has a lower ascending velocity in the fast-bubble flow region than free particle (Figure G.1), which means it has a higher slip velocity between solid particle and liquid phase to reduce the mass transfer boundary layer thus results in a higher mass transfer coefficient. This gives direct experimental evidence of Arters and Fan's (1990) results: mass transfer coefficient was higher in the column center than near the wall and particle tethering of any type affected mass transfer coefficient. If the tether is long enough, $\geq 3 R_c$, however, the effect on the mass transfer coefficient should not be too significant, as shown by the goodness of fit analysis for the velocity distributions.

CHAPTER 6

Conclusions and Recommendations

6.1 Conclusions

For 6.35 mm polycarbonate spheres, three flow regions existed in the vortical-spiral flow regime: the descending flow region, the vortical-spiral flow region, and the fast bubble flow region. For small and light particles such as polypropylene cylinders (equivalent diameter 4.211 mm), the same three flow regions were observed. However, ascending flow near the wall at one side of the column and descending flow near the wall at the other side of the column can exist simultaneously. The position of these ascending and descending flow regions changes dynamically. With increasing gas velocity, the size of fast-bubble flow region in the column center became larger for both the polycarbonate spheres and polypropylene cylinders.

With the conditions under study, the solid-liquid mass transfer was found to be independent of liquid velocity but to increase with increasing gas velocity for 30.48 cm column and for main-bed region of 12.7 cm column. The mass transfer coefficient (k_s) decreased with increasing gas superficial velocity in the distributor region of 12.7 cm column due to gas bypassing. The mass transfer coefficient was found to increase with column diameter. The scale up factor of $k_s \propto D_c^{0.31}$ was found to be a good approximation for a three-phase fluidized bed containing low density particles. Note that the mass transfer coefficients in this study were measured with a tether length of $\sqrt{2} R_c$.

RPT results suggested that particle tethering had little effect on x-velocities. In the z-direction, tethered particles exhibited slower movements and this was especially apparent with shorter tether lengths. A goodness of fit analysis of tethered versus free x and z-velocity distributions suggests that a tether length 3 times the column radius ($3 R_c$) was sufficient to reduce the effects of tethering.

6.2 Recommendations

The current RPT experiments were conducted in a two-dimensional manner. In order to verify the flow structure for light particles as a function of radial position, three-dimensional RPT experiments are necessary. Since the performance of a three-phase fluidized bed reactor is strongly affected by the particle residence time in the bubble wake, different shapes and sizes of particles should also be used to examine wake stabilization.

In order to test whether the tethered particle x- and z-velocities can be considered a sample population of the free particle x- and z-velocities, a goodness of fit analysis was done using instantaneous velocities from RPT data. Average particle ascending and descending velocities determined by using the best linear fits of z-position versus time curves (Figures G.1 and G.2) examined only one path from one run. In order to test whether the average tethered particle ascending and descending velocities can be considered a sample population of the average free particle ascending and descending velocities, a similar goodness of fit analysis should be done for average ascending and descending velocities from the entire data set.

Since the solid-liquid mass transfer coefficient increases with column diameter, more experiments with different column diameters are necessary to determine the scale-up coefficient of solid-liquid mass transfer. Moreover, conducting mass transfer experiments with a longer tether length ($3R_c$ and longer) is highly recommended.

One problem encountered in this study was that it was very hard to accurately predict the bed height as well as the holdups due to the nature of light particles. Conducting more experiments to establish an empirical correlation to accurately predict holdups for light particles would be valuable.

References

- Alvarez-Cuenca, M., Nerenberg, M.A., and Asfour, A.-F.A., 1984, Mass transfer effects near the distributor of three-phase fluidized beds. *Ind. Engng. Chem. Fundam.* **23**, 381-386.
- Arters, D. C. and Fan, L.-S., 1986, Solid-liquid mass transfer in a gas-liquid-solid fluidized bed. *Chem. Engng. Sci.* **41**, 107-115.
- Arters, D. C. and Fan, L.-S., 1990, Experimental methods and correlation of solid-liquid mass transfer in fluidized beds. *Chem. Engng. Sci.* **45**, 965-975.
- Arters, D. C., 1989, Solid-liquid mass transfer in multiphase fluidized beds. Ph.D. Thesis, The Ohio State University, Columbus, OH.
- Asfour, A.-F.A. and Nhaesi, A.H., 1990, An improved model for mass transfer in three-phase fluidized beds. *Chem. Engng. Sci.* **45**, 2895-2900.
- Asif, M., Kalogerakis, N. and Behie, L.A., 1991, Distributor effects in liquid fluidized beds of low-density particles. *AIChE J.* **37**, 1825-1832.
- Asif, M., Kalogerakis, N. and Behie, L.A., 1992, Hydrodynamics of liquid fluidized beds including the distributor region. *Chem. Engng. Sci.* **47**, 4155-4166.
- Baker, C.G.J., Kin, S.D. and Bergounou, M A., 1977, Wake characteristics of three-phase fluidized beds. *Powder Technology* **18**, 201-207.
- Ballesteros, R. L., Riba, J. P., and Couderc, J. P., 1982, Dissolution of non spherical particles in solid-liquid fluidization. *Chem. Engng. Sci.* **37**, 1639-1644.

Bhatia, V. K., and Epstein, N., 1974, Three phase fluidization: a generalized wake model, in *Fluidization and Its Applications* (edited by Angelino, H., Couderc, J.P., Gibert, H. and Laguerie, C.), 380-392, Cepadues-Editions, Toulouse.

Cassanello, M., Larachi, F., Guy, C. and Chaouki, J., 1996, Solids mixing in gas-liquid-solid fluidized beds: experiments and modeling. *Chem. Engng. Sci.* **51**, 2011-2020.

Castellana, F.S., Spencer, J.L. and Cartolano, A., 1980, Application of the gamma camera to studies of flow and mixing in reactor vessels. *Ind. Engng. Chem. Fundam.* **19**, 222-225.

Catros, A., Bernard, J.D., Briens, C.L. and Bergougnou, M.A, 1985, Gas hold-up above the bed surface and grid gas jet hydrodynamics for three-phase fluidized beds. *Can. J. Chem. Engng.* **63**, 754-759.

Chen, R. C., and Fan, L.-S., 1992, Particle image velocimetry for characterizing the flow structure in three-dimensional gas-liquid-solid fluidized beds. *Chem. Engng. Sci.* **47**, 3615-3622.

Chen, R. C., Reese, J. and Fan, L.-S., 1994, Flow structure in a three-dimensional bubble column and three-phase fluidized bed. *AIChE J.* **40**, 1093-1104.

Darton, R.C. and Harrison, D., 1975, Gas and liquid hold-up in three-phase fluidization, *Chem. Engng. Sci.* **30**, 581-586.

Dhanuka, V.R. and Stepanek, J.B., 1978, Gas and liquid hold-up and pressure drop measurements in a three-phase fluidized bed, in *Fluidization* (edited by Davidson, J.F. and Keairns, D.L.), 179-183, Cambridge University Press, Cambridge.

Dutta, N. N. and Pangarkar, V. G., 1993, Solid-liquid mass transfer in three-phase fluidized beds: some scale-up effects. *Chem. Engng. Commun.* **119**, 55-70.

Efremov, G. I. and Vakhrushev, I. A., 1970, A study of the hydrodynamics of three-phase fluidized beds. *Int. Engng. Eng.* **10**, 37-41.

El-Temtamy, S.A. and Epstein, N, 1978, Bubble wake solids content in three-phase fluidized beds. *Int. J. Multiphase Flow* **4**, 19-31.

El-Temtamy, S.A. and Epstein, N, 1980, Simultaneous solids entrainment and de-entrainment above a three-phase fluidized bed, in *Fluidization* (edited By Grace, J.R. and Matsen, J.M.), 519-528, Plenum Press, New York.

Epstein, N., 1981, Three-phase fluidization: some knowledge gaps. *Can. J. Chem. Engng.* **59**, 649-656.

Fan, L.-S, Satija, S. and Wisecarver, K., 1986, Pressure fluctuation measurements and flow regime transitions in gas-liquid-solid fluidized beds. *AIChE J.* **32**, 338-340.

Fan, L.-S., 1989, *Gas-Liquid-Solid Fluidization Engineering*. Butterworth Publishers, Boston, MA.

Freund, J.E. and Walpole, R.E., 1980, *Mathematical Statistics* (3rd Ed.). 413-415, Prentice-Hall Inc., Englewood Cliffs, New Jersey.

Fukuma, M., Sato, M., Muroyama, K. and Yasunishi, A., 1988, Particle-to-liquid mass transfer in gas-liquid-solid fluidization. *J. Chem. Engng. Japan* **21**, 231-237.

Gervais, A., Briens, C.L., Andre, J.C. and Wild, G., 1995, A modified axial dispersion model applied to three-phase fluidized bed reactors with a transition zone. *Trans. Inst. Chem. Engng. Part A*, **73**, 745-749.

Gogoi, N.C. and Dutta, N.N., 1996, Empirical approach to solid-liquid mass transfer in a three-phase sparged reactor. *Fuel Processing Technology* **48**, 145-157.

Hassanien, S., Delmas, H., and Riba, J.L., 1984, Transport des matiere liquid particles en fluidisation a trois phases. *Entropie* **119**, 17-26.

Jadhav, S. V. and Pangarkar, V. G., 1991, Particle-liquid mass transfer in three-phase sparged reactors: scale-up effects. *Chem. Engng. Sci.* **46**, 919-927.

Jakher, R. K., 1998, Hydrodynamics and mass transfer in different zones in a three-phase fluidized bed. M. Sc. Thesis, The University of Calgary, Calgary, AB.

Kantzas, A., Hamilton, K., Zarabi, T., Bhargava, A., Wright, I., Brook, G. and Chen, J.W., 1999, Application of gamma camera imaging and SPECT systems in chemical processes. 1st World Congress on Industrial Process Tomography, Buxton, Greater Manchester, April 14-17.

Kato, Y., Morooka, S., Koyama, M., Kago, T. and Yang, S., 1985, Longitudinal dispersion coefficient of liquid in three-phase fluidized bed for gas-liquid-solid systems. *J. Chem. Engng. Japan* **18**, 313.

Kiared, K., Larachi, F., Guy, C. and Chaouki, J., 1997, Trajectory length and residence-time distributions of the solids in three-phase fluidized beds. *Chem. Engng. Sci.* **52**, 3931-3939.

- Kikuchi, K., Takahashi, H., and Sugawara, T., 1995, Liquid-solid mass transfer in a slurry bubble column and a gas-liquid-solid three-phase fluidized bed. *Can. J. Chem. Engng.* **73**, 313-321.
- Kim, C. H., Delmas, H., and Riba, J. P., 1991, Liquid-solid mass-transfer and axial dispersion in three-phase fluidization. *Int. Chem. Engng.* **31**, 303-314.
- Kim, S. D., Kim, H. S. and Han, J. H., 1992, Axial dispersion characteristics in three-phase fluidized beds. *Chem. Engng. Sci.* **47**, 3419-3426.
- Kim, S.D. and Kim, C.H., 1983, Axial dispersion characteristics of three-phase fluidized beds. *J. Chem. Engng. Japan* **16**, 172-178.
- Kitano, K. and Fan, L.-S., 1988, Near-wake structure of a single gas bubble in a two-dimensional liquid-solid fluidized bed: solids holdup. *Chem. Engng. Sci.* **43**, 1355-1361.
- Larachi, F., Cassanello, M., Chaouki, J. and Guy, C., 1996, Flow structure of the solids in a 3-D gas-liquid-solid fluidized bed. *AIChE J.* **42**, 2439-2452.
- Larachi, F., Cassanello, M., Marie, M., Chaouki, J. and Guy, C., 1995, Solid circulation patterns in three-phase fluidized beds containing binary mixtures of particles as inferred from RPT. *Chem. Engng. Res. Des.* **73**, 263-267.
- Lin, J. S., Chen, M. M. and Chao, B. T., 1985, A novel radioactive particle tracking facility for measurement of solids motion in gas fluidized beds. *AIChE J.* **31**, 465-473.
- Morooka, S., Uchida, K. and Kato, Y., 1982, Recirculating turbulent flow of liquid in gas-liquid-solid fluidized bed. *J. Chem. Engng. Japan* **15**, 29-34.

Muroyama, K. and Fan, L.-S., 1985, Fundamentals of gas-liquid-solid fluidization. *AIChE J.* **31**, 1-34.

Nikov, I. and Delmas, H., 1987, Solid-liquid mass transfer in three-phase fixed and fluidized beds. *Chem. Engng. Sci.* **42**, 1089-1093.

Nishikawa, M., Inui, K., Yonezawa, Y. and Nagata, S., 1976, Mass transfer from solid particles in a spouted vessel. *Int. Chem. Engng.* **16**, 714-719.

Ostergaard, K., 1965, On bed porosity in gas-liquid fluidization. *Chem. Engng. Sci.* **20**, 165-167.

Page, R.E. and Harrison, D., 1974, Particle entrainment from a three-phase fluidized bed, in *Fluidization and Its Applications* (edited by Angelino, H., Couderc, J.P., Gibert, H. and Laguerie, C.), 393-406, Cepadues-Editions, Toulouse.

Pearson, E.S. and Hartley, H.O., 1966, *Biometrika Tables for Statisticians* (3rd Ed.). Volume I, 137, The University Press, Cambridge.

Prakash, A., Briens, C. L. and Bergougnou, M. A., 1987, Mass transfer between solid particles and liquid in a three-phase fluidized bed. *Can. J. Chem. Engng.* **65**, 228-236.

Rigby, G. R., and Capes, C. E., 1970, Bed expansion and bubble wakes in three-phase fluidization. *Can. J. Chem. Engng.* **48**, 343-348.

Song, J.S., Hyndman, C.L., Jakher, R.K., Hamilton, K. and Kantzas, A., 1999, Fundamentals of hydrodynamics and mass transfer in a three-phase fluidized bed system. *Chem. Engng. Sci.* **54**, 4967-4973.

Steele, L.R., M.Sc. Thesis, The Ohio State University, Columbus, Ohio (1958).

Tzeng, J. -W., Chen, R. C. and Fan, L.-S., 1993, Visualization of flow characteristics in a 2-D bubble column and three-phase fluidized bed. *AIChE J.* **39**, 733-744.

Weast, R.C. and Astle, M.J. (eds.), 1982, *Handbook of Chemistry and Physics*. CRC press, Cleveland, Ohio.

Werther, J., 1992, Scale-up modeling for fluidized bed reactors. *Chem. Engng. Sci.* **47**, 2457-2462.

Zarabi, T. 1998, Analysis of X-ray/gamma-ray tomographic imaging data to describe hydrodynamic properties of gas-polyethylene fluidized beds. M.Sc. thesis, The University of Calgary, Calgary, AB.

Zhang, J.-P., Grace, J.R., Epstein N. and Lin, K.S., 1997, Flow regime identification in gas-liquid flow and three-phase fluidized beds. *Chem. Engng. Sci.* **52**, 3979-3992.

Zheng, C., Yao, B.P. and Feng, Y.D., 1988, Flow regime identification and gas hold-up of three-phase fluidized system. *Chem. Engng. Sci.* **43**, 2195-2200.

Appendix A Rotameter Calibration

In the present study, the calibration equation obtained using the magnetic flowmeter was used to determine the liquid velocity for 12.7 cm ID column.

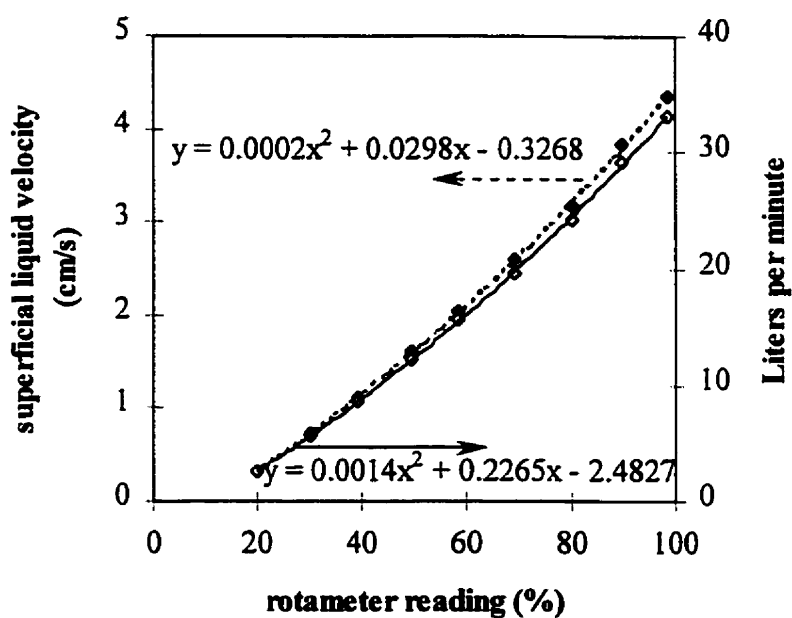


Figure A.1 Rotameter calibration curve

Appendix B Gas-Liquid Distributor

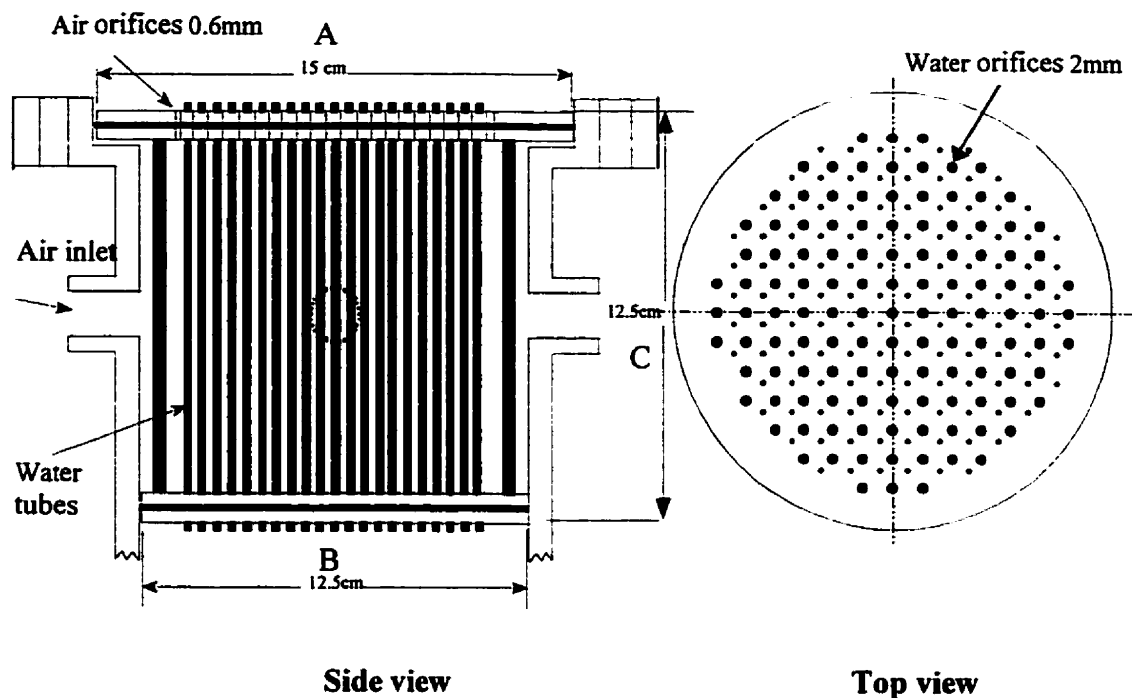


Figure B.1 Gas-liquid distributor for 12.7 cm ID column

For the 30.48 cm diameter column, the gas-liquid distributor is essentially a scaled version of the one shown above. It also has 109 water tubes (6.35 cm ID) and 121 air orifices (0.6 mm ID). The dimensions denoted as A, B and C above are 32, 30.48 and 21 cm respectively.

Appendix C Minimum L-S Fluidized Velocity

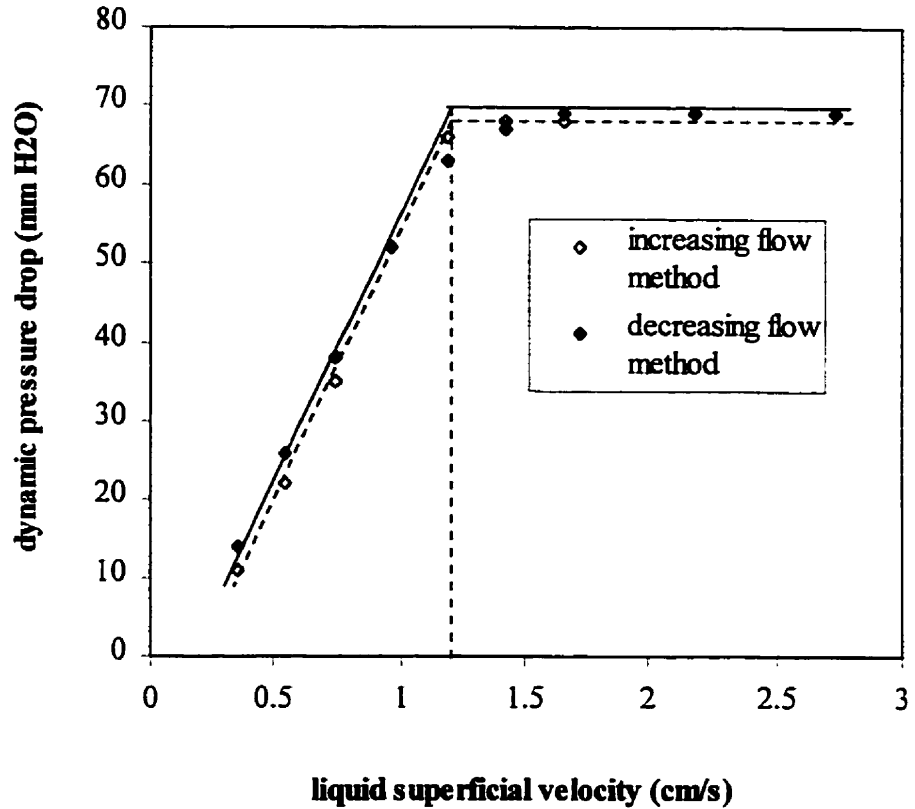


Figure C.1 Dynamic pressure drop for determining the minimum fluidization velocity in a L-S fluidized bed ($D_c = 12.7$ cm)

Dynamic pressure drop can be used to determine the minimum fluidization velocity in a fluidized bed. For liquid-polypropylene beads system, the pressure drop increases sharply with increasing liquid velocity in the fixed-bed state. Whereas in the fluidized bed state, the pressure drop almost remains constant. The change of the slope indicates where the incipient fluidization occurs. Both increasing and decreasing liquid flow rate methods show a minimum fluidization velocity of 1.2 cm/s.

Appendix D Mass Transfer Coefficient Experimental Data

The mass transfer coefficient was calculated using Equation 3.1 with $C_b = 0$. To calculate Sherwood number, the viscosities and densities of water and air were assumed constant and were obtained from the CRC Handbook of Chemistry and Physics at 20 °C (Weast and Astle, 1982).

Benzoic acid saturation concentration was calculated from the correlation proposed by Steele (1958):

$$C_{sat} (g/L) = 1.6976 + 0.021758T + 0.001853686T^2 \quad (D.1)$$

Benzoic acid particles for mass transfer measurements were cylindrical in shape. In the following table, D1 and D2 are the diameters of the active benzoic acid particle in perpendicular direction. H1 and H2 are the heights of the active benzoic acid particle measured on two opposite edges. Particle equivalent diameter D_p was calculated by:

$$D_p = (3(D1 + D2)^2(H1 + H2)/16)^{1/3} \quad (D.2)$$

For example, the first particle in Table D.1 has the following dimensions: D1 = 3.722 mm, D2 = 3.703 mm, H1 = 4.691 mm, H2 = 4.607 mm, and its equivalent diameter is $D_p = 4.58$ mm. Particle surface area $A_p = \pi(D1+D2)(H1+H2)/4 + 2\pi(D1+D2)^2/16$. Weight before and weight after refer to the particle weight before and after the experiment. The change of benzoic acid particle size was negligible during the experiments, so A_p was treated as a constant (equal to initial surface area). Position 1 refers to the first injection port in the 12.7 cm ID column, which is 7.62 cm above the distributor plate. Position 3 refers to the third injection port in the 12.7 cm ID column, which is 50.8 cm above the distributor plate. Position 2 refers to the second injection port in the 30.48 cm ID column, which is 25 cm above the distributor plate. Position 6 refers to the sixth injection port in the 30.48 cm ID column, which is 130 cm above the distributor plate. Temperature was monitored at the outlet of the column using a thermocouple. Time was measured using a stop watch.

Table D.1 Mass transfer data from the 12.7 cm ID column

particle number	D1 (mm)	D2 (mm)	H1 (mm)	H2 (mm)	weight before (g)	weight after (g)	position	U _L (cm/s)	U _g (cm/s)	T (°C)	C _{sat} (g/L)	time (s)	k (m/s)
1	3.722	3.703	4.691	4.607	0.1254	0.1172	1	2	1	16.82	2.5880	650	6.42E-05
2	3.722	3.644	4.699	4.644	0.125	0.1179	3	2	1	16.97	2.6007	610	5.94E-05
3	3.629	3.678	4.889	4.874	0.1258	0.1176	1	2	1	18.5	2.7345	615	6.33E-05
4	3.654	3.607	4.655	4.677	0.1194	0.1127	3	2	1	18.73	2.7554	605	5.44E-05
5	3.689	3.658	4.608	4.725	0.1239	0.1159	1	2	1	19.02	2.7820	610	6.28E-05
6	3.674	3.678	4.667	4.746	0.1261	0.1189	3	2	1	19.19	2.7978	603	5.65E-05
7	3.694	3.727	4.735	4.814	0.1275	0.1206	1	3	1	15.87	2.5098	612	5.81E-05
8	3.711	3.641	5.025	5.123	0.1289	cracked		3	1				
9	3.712	3.763	4.675	4.56	0.127	0.1191	3	3	1	16.38	2.5513	605	6.72E-05
10	3.724	3.734	4.862	4.675	0.1296	0.1227	1	3	1	16.65	2.5738	602	5.73E-05
11	3.701	3.675	5.031	4.947	0.1276	0.1192	3	3	1	16.89	2.5939	600	6.82E-05
12	3.672	3.683	4.671	4.806	0.1263	0.1193	1	3	1	17.32	2.6305	603	5.81E-05
13	3.723	3.678	5.145	5.187	0.1276	0.1198	3	3	1	17.65	2.6591	600	5.99E-05
14	3.632	3.605	4.772	4.462	0.1252	0.1177	1	4	1	15.32	2.4660	600	6.94E-05
15	3.680	3.733	4.99	5.086	0.1325	0.1263	3	4	1	15.53	2.4826	600	5.19E-05
16	3.766	3.723	4.867	4.851	0.1294	0.1228	1	4	1	15.81	2.5049	600	5.55E-05
17	3.654	3.699	4.681	4.726	0.1248	0.1186	3	4	1	15.93	2.5146	600	5.44E-05
18	3.721	3.696	4.78	4.832	0.1283	0.121	1	4	1	16.65	2.5738	600	6.09E-05
19	3.681	3.681	4.879	4.861	0.1272	0.1195	3	4	1	16.91	2.5956	600	6.37E-05
20	3.630	3.707	4.59	4.624	0.1239	0.117	1	2	2	17.57	2.6521	605	5.79E-05

Table D.1 continued

particle number	D1 (mm)	D2 (mm)	H1 (mm)	H2 (mm)	weight before (g)	weight after (g)	position	U _L (cm/s)	U _g (cm/s)	T (°C)	Csat (g/L)	time (s)	k (m/s)
21	3.717	3.67	4.274	4.302	0.1193	0.1112	3	2	2	17.62	2.6565	602	7.12E-05
22	3.661	3.71	4.465	4.584	0.1249	0.1173	1	2	2	18.05	2.6943	600	6.38E-05
23	3.711	3.664	4.854	4.858	0.1298	0.1204	3	2	2	18.21	2.7085	600	7.45E-05
24	3.674	3.656	4.81	4.803	0.1277	0.1198	1	2	2	18.41	2.7264	600	6.32E-05
25	3.753	3.692	4.467	4.504	0.1235	0.1148	3	2	2	18.54	2.7382	600	7.13E-05
26	3.688	3.687	4.823	4.832	0.1298	0.123	1	2	3	15.88	2.5106	600	5.84E-05
27	3.594	3.645	4.998	4.987	0.1259	0.1165	3	2	3	15.97	2.5178	600	8.04E-05
28	3.690	3.713	4.73	4.752	0.1292	0.1222	1	2	3	16.36	2.5497	600	5.97E-05
29	3.654	3.681	4.651	4.635	0.1233	0.1143	3	2	3	16.48	2.5596	600	7.85E-05
30	3.747	3.75	4.278	4.352	0.1232	0.1164	1	2	3	16.79	2.5855	603	5.98E-05
31	3.662	3.709	4.369	4.417	0.1232	0.1142	3	2	3	16.97	2.6007	600	7.99E-05

Table D.2 Mass transfer data from the 30.48 cm ID column

particle number	D1 (mm)	D2 (mm)	H1 (mm)	H2 (mm)	weight before (g)	weight after (g)	position	U _L (cm/s)	U _g (cm/s)	T (°C)	C _{sat} (g/L)	time (s)	k (m/s)
13	3.597	3.604	5.395	5.181	0.1433	0.1337	2	2	2	21.4	3.0121	605	6.57E-05
14	3.598	3.628	5.105	5.106	0.1437	0.1288	6	2	2	21.67	3.0396	610	0.000102
15	3.584	3.577	4.783	4.782	0.1408	0.1317	2	2	2	21.9	3.0631	606	6.63E-05
16	3.65	3.682	4.993	4.929	0.1457	0.132	6	2	2	22.11	3.0848	603	9.41E-05
17	3.649	3.626	4.533	4.534	0.1376	0.1286	2	2	2	22.22	3.0963	604	6.63E-05
18	3.617	3.612	4.602	4.499	0.1354	0.1215	6	2	2	22.36	3.1109	601	0.000103
19	3.587	3.613	5.395	5.282	0.1463	0.1367	6	4	1	17.24	2.6237	600	7.55E-05
20	3.619	3.603	5.11	5.152	0.1453	0.1382	2	4	1	17.51	2.6469	603	5.65E-05
21	3.613	3.616	4.689	4.659	0.1391	0.1308	6	4	1	17.63	2.6574	602	7.05E-05
22	3.685	3.686	4.745	4.725	0.1422	0.1345	2	4	1	17.82	2.6740	600	6.3E-05
23	3.632	3.683	4.907	4.749	0.1434	0.1347	6	4	1	18.19	2.7067	604	6.96E-05
24	3.689	3.72	5.03	5.071	0.1464	0.1387	2	4	1	18.38	2.7237	606	5.81E-05
25	3.653	3.647	5.037	4.898	0.1442	0.1351	6	3	1	19.04	2.7839	604	6.95E-05
26	3.68	3.645	4.856	4.827	0.1428	0.136	2	3	1	18.94	2.7747	603	5.29E-05
27	3.627	3.642	5.579	5.356	0.1477	0.1382	6	3	1	18.58	2.7418	600	6.94E-05
28	3.67	3.644	4.411	4.4	0.1379	0.1304	2	3	1	18.95	2.7756	605	6.24E-05
29	3.657	3.592	4.855	4.858	0.1402	0.1311	6	3	1	19.27	2.8052	600	7.12E-05
30	3.616	3.638	5.059	5.042	0.1426	0.1348	2	3	1	19.43	2.8202	603	5.86E-05
31	3.621	3.622	5.431	5.311	0.1461	0.1359	6	2	1	19.14	2.7931	600	7.45E-05
32	3.653	3.644	4.954	4.941	0.1436	0.1366	2	2	1	19.37	2.8145	604	5.31E-05

Table D.2 continued

particle number	D1 (mm)	D2 (mm)	H1 (mm)	H2 (mm)	weight before (g)	weight after (g)	position	U_L (cm/s)	U_g (cm/s)	T (°C)	Csat (g/L)	time (s)	k (m/s)
33	3.637	3.625	5.134	5.091	0.1457	0.136	6	2	1	19.61	2.8371	600	7.21E-05
34	3.62	3.636	5.422	5.276	0.1479	0.1404	2	2	1	19.66	2.8418	602	5.37E-05
35	3.678	3.661	4.6	4.59	0.1405	0.1307	6	2	1	19.92	2.8666	601	7.67E-05
36	3.669	3.672	4.3	4.312	0.1371	0.1301	2	2	1	20.06	2.8800	606	5.66E-05
37	3.628	3.649	4.798	4.646	0.1393	0.1241	6	2	3	20.4	2.9129	601	0.000116
38	3.655	3.629	4.639	4.566	0.1387	0.1282	2	2	3	20.52	2.9246	603	8.1E-05
39	3.738	3.673	4.158	4.36	0.1363	0.1221	6	2	3	20.72	2.9442	607	0.000112
40	3.648	3.614	4.533	4.524	0.1403	0.1255	6	2	3	21.04	2.9760	608	0.000113
41	3.682	3.668	5.025	5.144	0.1443	0.1324	2	2	3	20.93	2.9650	605	8.3E-05
42	3.628	3.65	5.055	5.031	0.1445	0.1328	2	2	3	21.15	2.9870	609	8.2E-05

Appendix E RPT Image Data

128 x 128 array was used in this study with a pixel size of 0.343 cm x 0.343 cm. Each frame consisted of cluster of pixels which had a variety of counts and the rest were empty pixels. The FORTRAN program written by Amit Bhargava and Jinwen Chen was used to read the counts as well as their pixel index. Center of mass was then used to determine the particle position in the camera window. In the following table, column x-position and z-position were thus obtained. The reference point was located at 50.8 cm above the distributor plate, and this was the 55th pixel from the top. Thus the z-adjusted column was equal to $(z\text{-position} + 50.8 - (128 - 55) * 0.343)$ cm. x-velocity and z-velocity were calculated using $(x_n - x_{n-1}) / (t_n - t_{n-1})$ and $(z_n - z_{n-1}) / (t_n - t_{n-1})$ respectively.

Particle occurrence in the column for set 2 and set 3 RPT experiments are also shown in Figures E.1 to E.9.

Table E.1 Sample of RPT image data after treating

(PP, tethered = 9 cm, run 11)

time (s)	x-position (cm)	z-position (cm)	z-adjusted (cm)	x-velocity (cm/s)	z-velocity (cm/s)
0	4.336	18.3314	44.0924	-7.868	-2.644
0.05	3.9426	18.1992	43.9602	3.19	-1.34
0.1	4.1021	18.1322	43.8932	0.72	7.532
0.15	4.1381	18.5088	44.2698	-2.216	-12.77
0.2	4.0273	17.8703	43.6313	-4.116	7.46
0.25	3.8215	18.2433	44.0043	1.248	-10.952
0.3	3.8839	17.6957	43.4567	-6.736	-3.368
0.35	3.5471	17.5273	43.2883	5.832	3.088
0.4	3.8387	17.6817	43.4427	1.852	3.224
0.45	3.9313	17.8429	43.6039	2.026	-0.93
0.5	4.0326	17.7964	43.5574	4.354	2.936
0.55	4.2503	17.9432	43.7042	-7.204	-6.604
0.6	3.8901	17.613	43.374	-2.636	5.904

Table E.1 continued

time (s)	x-position (cm)	z-position (cm)	z-adjusted (cm)	x-velocity (cm/s)	z-velocity (cm/s)
0.65	3.7583	17.9082	43.6692	-2.656	4.926
0.7	3.6255	18.1545	43.9155	3.296	-4.188
0.75	3.7903	17.9451	43.7061	1.248	-3.742
			.		
			.		
			.		
49	1.7635	18.1981	43.9591	1.016	1.778
49.05	1.8143	18.287	44.048	-4.914	12.34
49.1	1.5686	18.904	44.665	-1.506	8.262
49.15	1.4933	19.3171	45.0781	-11.452	16.732
49.2	0.9207	20.1537	45.9147	-4.076	11.604
49.25	0.7169	20.7339	46.4949	-8.032	10.108
49.3	0.3153	21.2393	47.0003	0.186	12.162
49.35	0.3246	21.8474	47.6084	-1.432	15.68
49.4	0.253	22.6314	48.3924	2.106	13.298
49.45	0.3583	23.2963	49.0573	7.858	15.194
49.5	0.7512	24.056	49.817	4.048	8.036
49.55	0.9536	24.4578	50.2188	7.28	13.682
49.6	1.3176	25.1419	50.9029	6.322	11.754
49.65	1.6337	25.7296	51.4906	11.386	10.198
49.7	2.203	26.2395	52.0005	15.348	17.278
49.75	2.9704	27.1034	52.8644	10.62	6.046
49.8	3.5014	27.4057	53.1667	14.472	22.678
49.85	4.225	28.5396	54.3006	7.668	24.212
49.9	4.6084	29.7502	55.5112	3.196	15.948
49.95	4.7682	30.5476	56.3086	-95.364	-1126.172

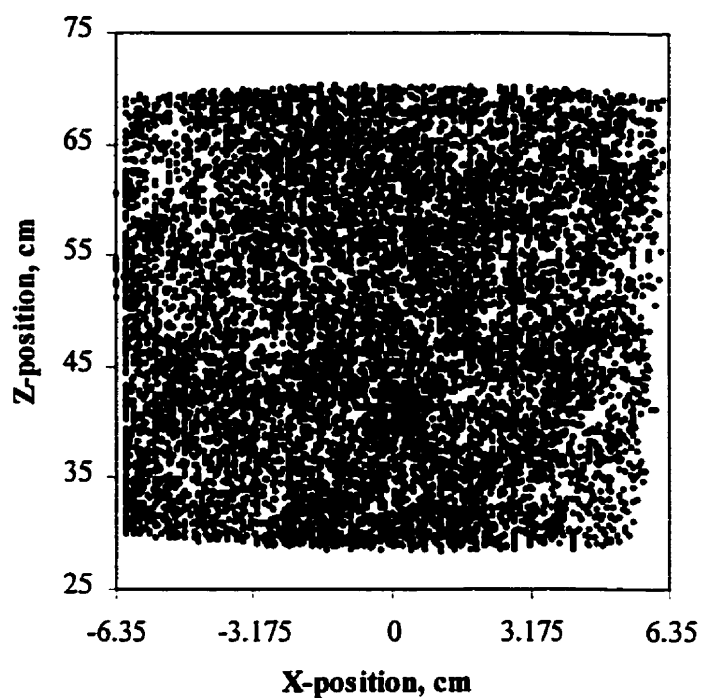


Figure E.1 Particle occurrence in the column (PC, free particle, $U_g = 2.16$ cm/s)

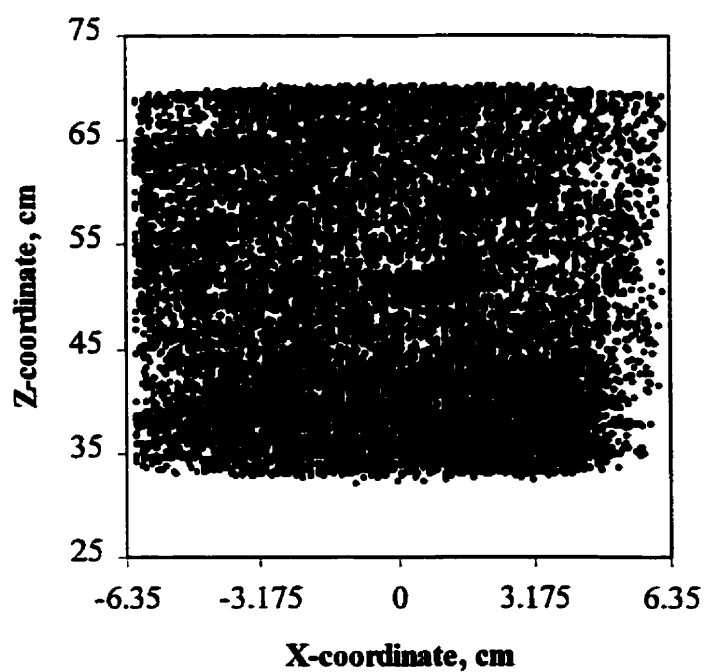


Figure E.2 Particle occurrence in the column (PC, tether = 19 cm, $U_g = 2.16$ cm/s)

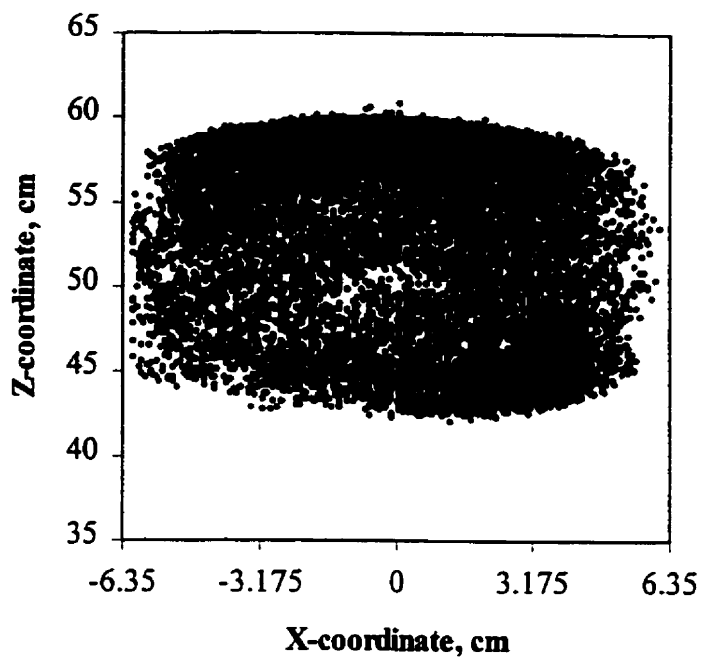


Figure E.3 Particle occurrence in the column (PC, tether = 9 cm, $U_g = 2.16$ cm/s)

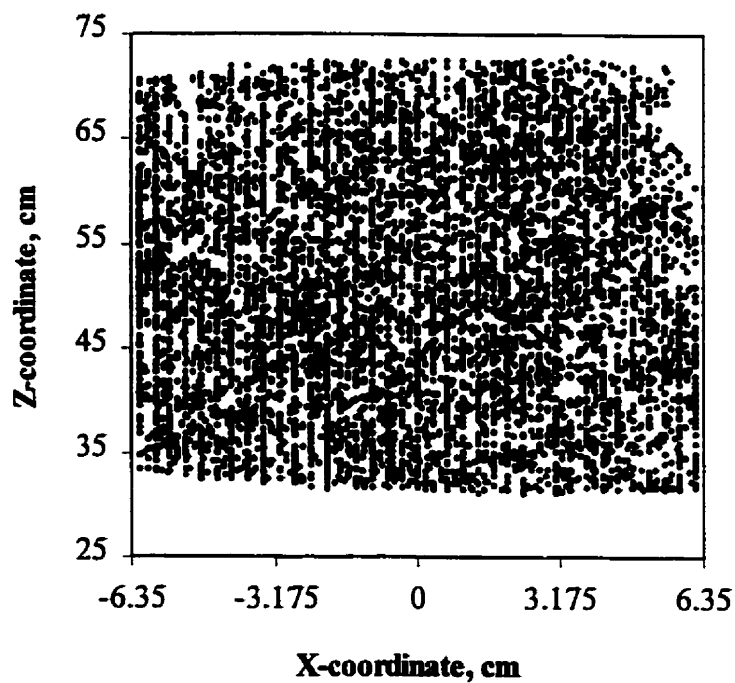


Figure E.4 Particle occurrence in the column (PP, free particle, $U_g = 2.0$ cm/s)

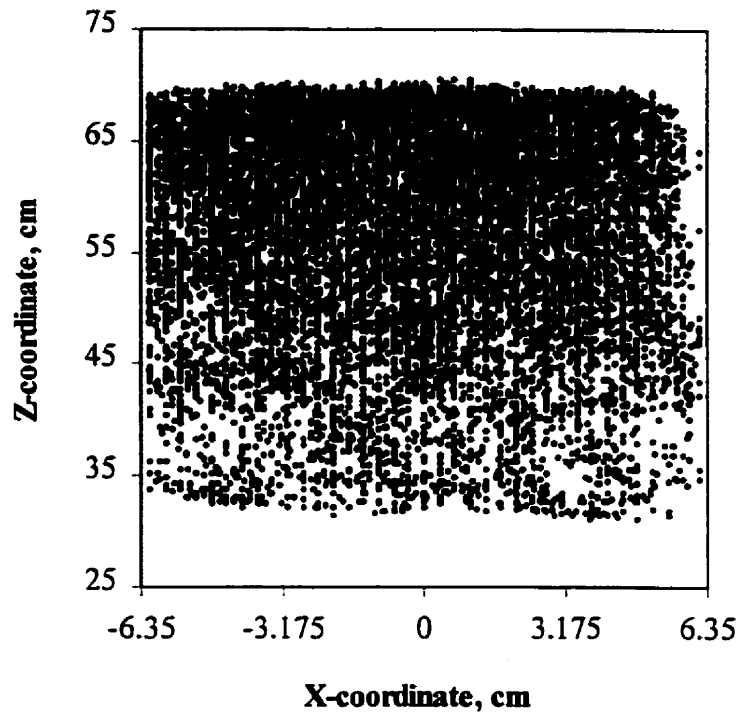


Figure E.5 Particle occurrence in the column (PP, tether = 19 cm, $U_g = 2.0$ cm/s)

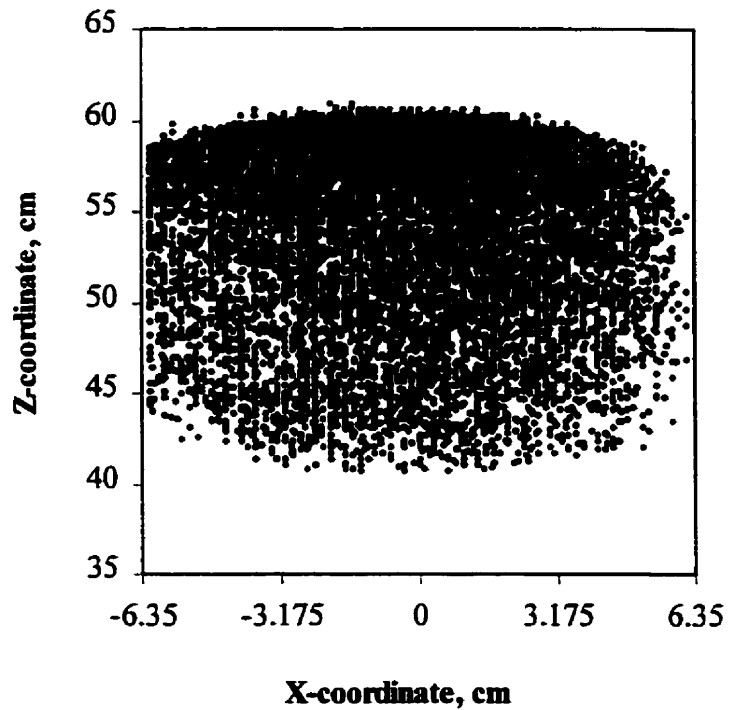


Figure E.6 Particle occurrence in the column (PP, tether = 9 cm, $U_g = 2.0$ cm/s)

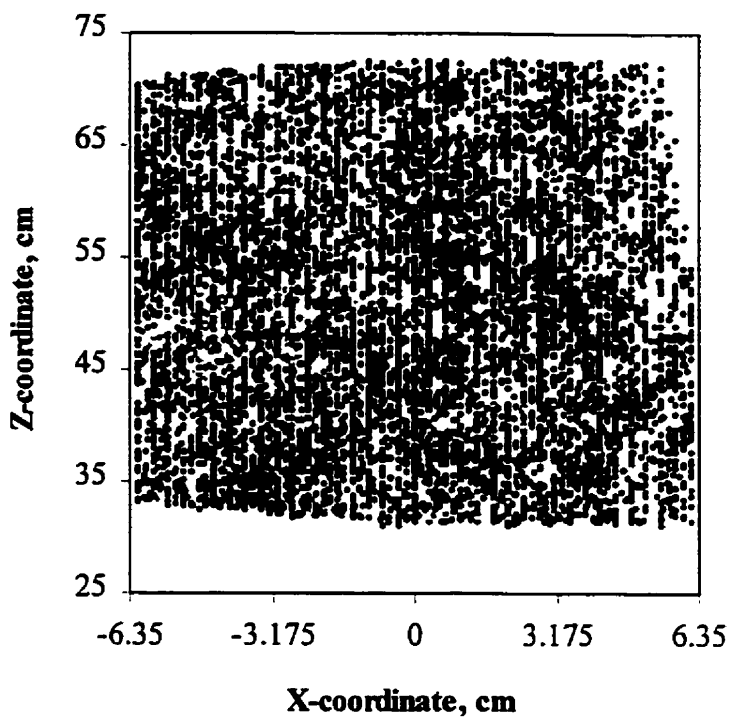


Figure E.7 Particle occurrence in the column (PP, free particle, $U_g = 0.82$ cm/s)

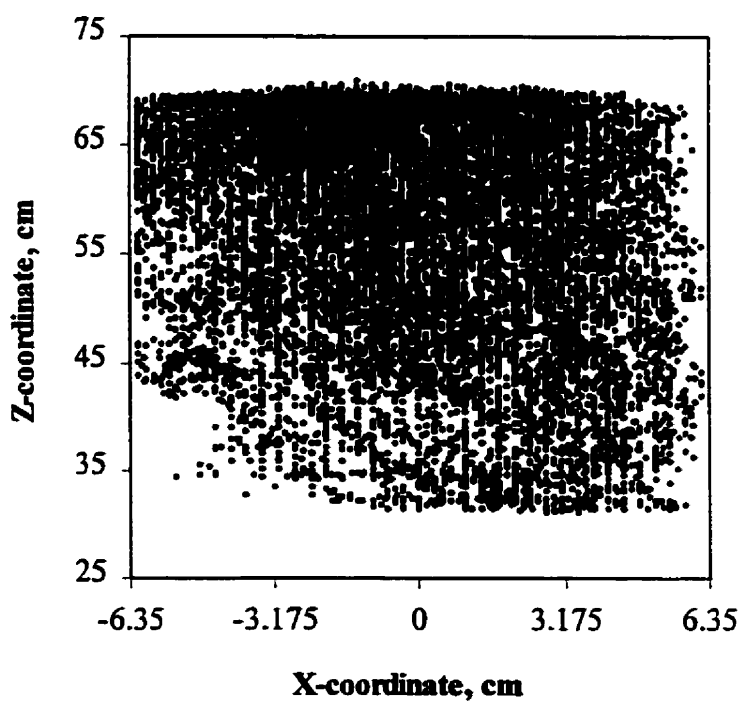


Figure E.8 Particle occurrence in the column (PP, tether = 19 cm, $U_g = 0.82$ cm/s)

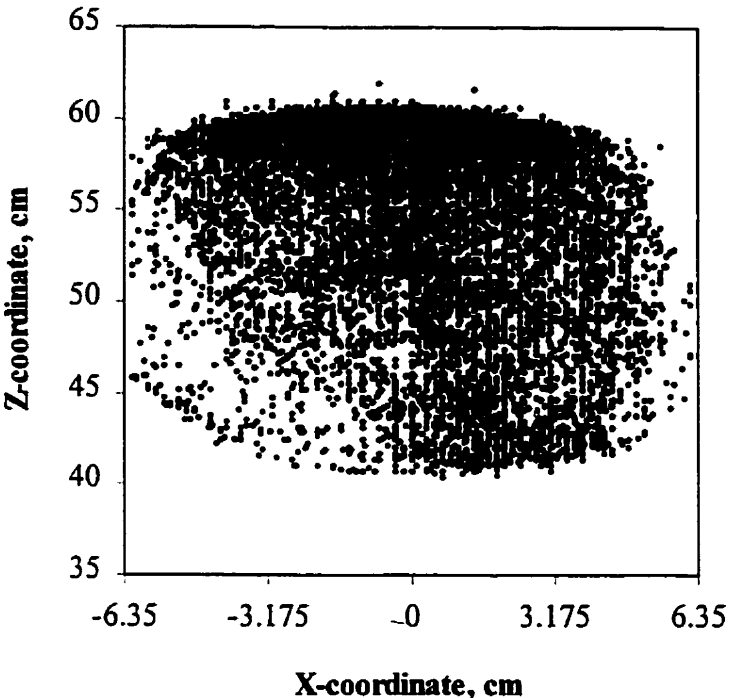


Figure E.9 Particle occurrence in the column (PP, tether = 9 cm, $U_g = 0.82$ cm/s)

Appendix F Goodness of Fit Analysis

For all the goodness of fit analysis in this study, the level of significance α was 0.05. Critical region $\chi^2_{\alpha, m-2}$ was obtained from Biometrika Tables for Statisticians (1966). The value of goodness of fit χ^2 was calculated from the following equation:

$$\chi^2 = \sum_{i=1}^m \frac{(f_i - e_i)^2}{e_i}$$

A sample calculation of χ^2 is illustrated in Table F.1. In this example, the number of terms in column "Free particle x-velocity frequency in main bed (e_i)" is 29, thus $m = 29$. From the Biometrika Tables for Statisticians, the critical region $\chi^2_{0.05, 27} = 40.113$. The summation term in the last column is 5.66. Since $\chi^2 < \chi^2_{0.05, 27}$, the hypothesis that the tethered particle velocity distribution could be sample from the free particle velocity distribution is accepted.

Table F.1 Sample calculation of the goodness of fit analysis (PC, $U_g = 1.46$ cm/s, $U_L = 2.08$ cm/s)

Bin	Free particle x-velocity frequency in main bed (e_i)	Tethered particle x-velocity frequency in main bed (f_i)	$(f_i - e_i)^2 / e_i$
-100	0	0	0
-95	0	0	0
-90	0	0	0
-85	0	0	0
-80	0	0	0
-75	0	0	0
-70	0.000146908	0	0.01469076
-65	0.000146908	0	0.01469076
-60	0.000440723	0	0.044072279
-55	0.00058763	0	0.058763038
-50	0.000293815	0	0.029381519
-45	0.001322168	0	0.132216836
-40	0.001762891	0.000625626	0.073366575

Table F.1 continued

Bin	Free particle x-velocity frequency in main bed (e_i)	Tethered particle x-velocity frequency in main bed (f_i)	$(f_i - e_i)^2 / e_i$
-35	0.000881446	0.001126126	0.00679209
-30	0.003819597	0.003128128	0.012517807
-25	0.003966505	0.00513013	0.034136431
-20	0.010577347	0.019394394	0.734970012
-15	0.024386661	0.039414414	0.926052898
-10	0.065226972	0.07982983	0.326925262
-5	0.147789041	0.146771772	0.000700212
0	0.254590862	0.217217217	0.548640803
5	0.231085647	0.189439439	0.750547096
10	0.134567357	0.145895896	0.095369184
15	0.061260467	0.082207207	0.716230121
20	0.028646981	0.043918919	0.814159391
25	0.01469076	0.016016016	0.011955167
30	0.005435581	0.006256256	0.012390724
35	0.003819597	0.001501502	0.140684168
40	0.001909799	0.001251251	0.022708403
45	0.000881446	0.000375375	0.029055344
50	0.000734538	0.000500501	0.00745687
55	0.000146908	0	0.01469076
60	0.000293815	0	0.029381519
65	0.000146908	0	0.01469076
70	0	0	0
75	0.000293815	0	0.029381519
80	0	0	0
85	0	0	0
90	0	0	0
95	0	0	0
100	0	0	0
Σ	-	-	$\chi^2 = 5.66$

Please note that Table 2 in Song *et al.* (1999) has an error and the corrected version is Table 5.3 in this thesis.

Appendix G Calculation of Average Particle Ascending and Descending Velocities

The average particle ascending and descending velocities can be determined by using the best linear fits of z-position versus time curves. The points in Figure G.1 were taken from the particle trajectory in area B of Figure 5.25. The points in Figure G.2 were taken from the particle trajectory in area A of Figure 5.30. The slopes represent the particle velocities.

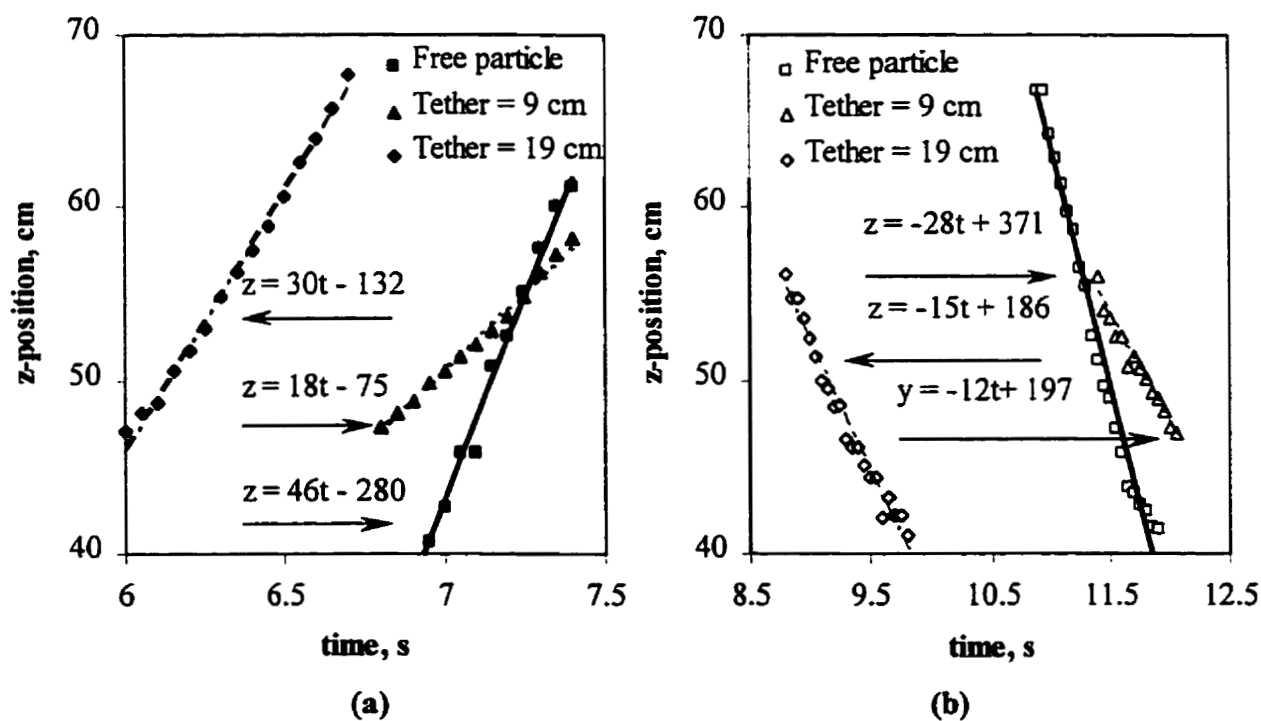
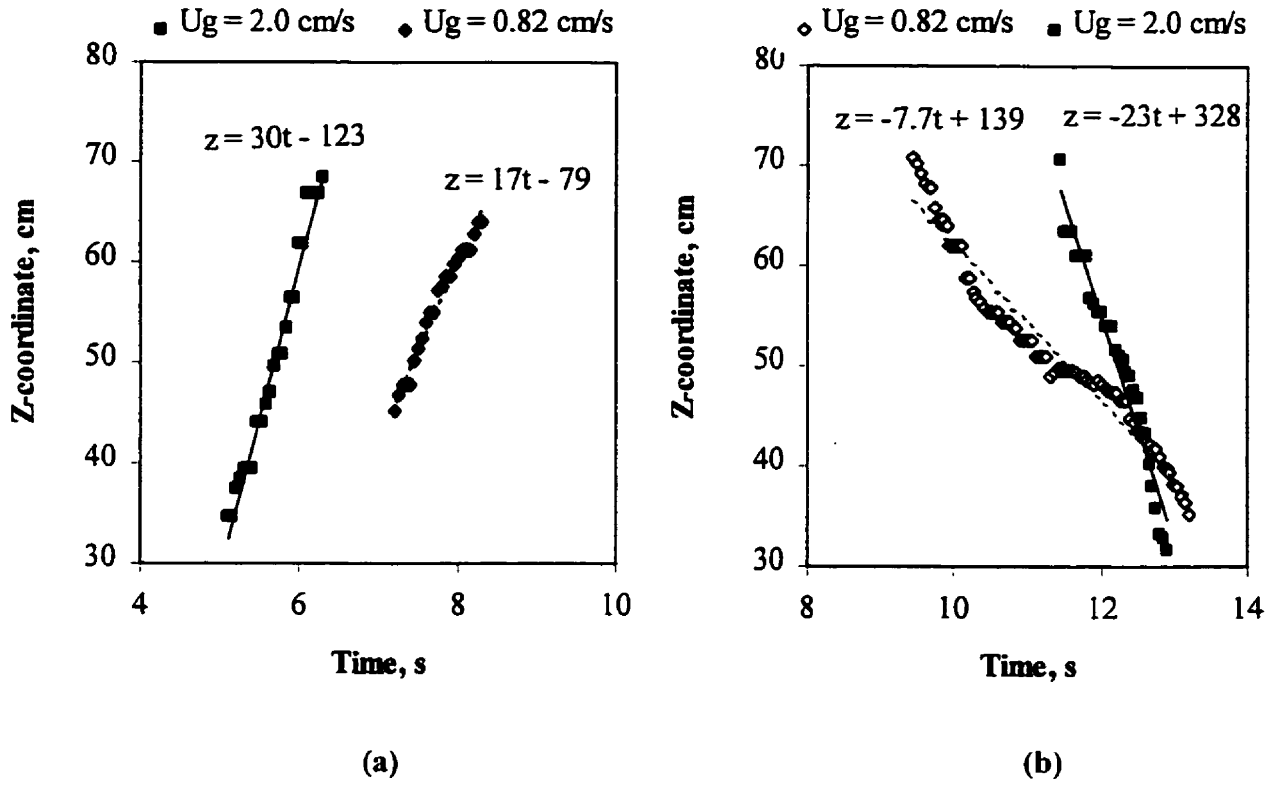


Figure G.1 Particle velocities in area B of Figure 5.25: (a) Ascending (b) Descending (PC, $U_L = 2.69$ cm/s)



**Figure G.2 Particle velocities in area A of Figure 5.30: (a) Ascending
(b) Descending (PP, $U_L = 2.20 \text{ cm/s}$)**